UNIVERSITY OF LIVERPOOL

Study on the Mechanisms and Prediction Methods of Arcing Contact Erosion of High-voltage SF_6 Circuit Breaker

Thesis submitted in accordance with the requirements of
the University of Liverpool for the degree of Doctor in Philosophy

By

Zhixiang Wang

September 2018

Acknowledgements

To begin with, I would like to acknowledge and extend my heartfelt gratitude to my supervisors — Professor J. W. Spencer, Professor M. Z. Rong and Prof. J. D. Yan for their support and continuous encouragement throughout my study, for their vital encouragement and patient guidance, generous assistance and invaluable advice, all of which have been of inestimable worth to the completion of my thesis. Specially, I am grateful to Professor G. R. Jones for his guidance of the experimental work and suggestions during the writing of this thesis. All these scholars with stringent realistic attitude in their scholarly work, great generousness and kindness to people, a high degree of professionalism, dedication and assiduous work style and bold innovation and entrepreneurial spirit to me has an important impact and will encourage me to continue the journey of research and service to others.

I also wish to thank other members of the Arc Research Group in Xi'an Jiaotong University and the University of Liverpool, especially Mr. J. E. Humphries, Mr. G. Blacoe and Ms. J. Anson, for their valuable discussions and tremendous assistance on the design and construction of the experimental platform. Additionally, I would like to take this opportunity to express my gratitude to the Dual Collaborative PhD Degree Program between Xi'an Jiaotong University and the University of Liverpool and the Chinese Government Scholarship Program for Postgraduates. This thesis would not have been possible without their financial support. Thanks also go to all my colleagues and friends for making my time at the University of Liverpool and Xi'an Jiaotong University a great experience.

The last but not least, to my family, I wish to express my greatest thanks for their love, endless support and encouragement which give me confidence, wisdom, strength, and endurance to pursue my dreams throughout all my study.

Abstract

High-voltage SF_6 circuit breaker (SF_6 HVCB) is a key equipment in the power transmission system for breaking the fault current and protecting the safe and stable operation of the power grid. In the process of current breaking, the arcing contacts will be eroded subjecting to the heat of the arc, which will seriously affect the capability of breaking current and the electrical lifetime of the HVCB, and further endanger the safe and stable operation of the power grid. The investigation of the erosion mechanisms and prediction methods of arcing contacts erosion of HVCB can advance the theory of contacts erosion, improve the accuracy of massloss prediction of the arcing contacts to provide reference for the condition maintenance of the equipment. This thesis takes the SF_6 HVCB as the research object and strives to lay a theoretical foundation for the development of monitoring system of arcing contacts erosion.

Based on a 245kV/40kA live tank SF_6 HVCB, an arcing contact erosion experimental platform is built using a noval fiber-optic sensor system. The use of optical approaches effectively avoids electromagnetic interference in a practical scenario. Using the combination of high-speed camera and multiple reflective mirrors, the macroscopic behavior of the arc is observed, which provides important reference for the install location of sensors. By using a noval fiber-optic sensor system, combined with photodiode and high-speed spectrometer, the trajectory and time-varying spectra of the arc roots on the arc contact surface are monitored synchronously, offering abundant experimental data for further investigation of massloss prediction algorithm of arcing contacts erosion. Using the spatial domain chromatic method to predict the massloss of arcing contacts, the prediction accuracy is improved by 31.0% compared to the existing widely used arc energy accumulation method.

The macroscopic behavior of the arc in the SF_6 HVCB and its effects on arcing contact erosion are studied. Using high-speed photography technology, the shape of the

arc column, the spatial distribution of metal vapor of the arc column, and the mobility of the arc root on the contact surface are observed. The effects of the shape of the arc column and the mobility of the arc root on the erosion process are interpreted. Using the spatial domain chromatic method, the trajectory of the arc root on the contact surface is measured. The mobility of the arc root at different current levels is studied and a method for the massloss prediction of the arcing contacts at relative low currents is proposed.

A prediction method of massloss of arcing contacts based on chromatic analysis of arc spectra is proposed. Through the analysis of chromatic spectral data both in the wavelength domain and time domain, a series of chromatic parameters representing the erosion characteristics of the arcing contacts are obtained, and the contacts erosion modes at various current amplitudes are identified. Furthermore, the chromatic parameters which are closely related to the arc contact ablation are selected. In combination with the linear regression algorithm, the prediction method for massloss of the arcing contacts at relative high currents is explored, the accuracy of massloss prediction has been improved by 39.1% comparing with using the square of current.

A 3D thermal model of arcing contact erosion considering the movement of the arc root and the structure of the copper-tungsten material is proposed. The temperature, mass loss rate, and change of contact surface geometry are simulated and compared with the experimental data and the simulation results of a fixed arc root model. The influence of the root movement on the erosion process is further verified and explained. The simulated results of massloss of arcing contacts are obtained.

Table of contents

List of figures

List of tables

Chapter 1

Introduction

1.1 Background

With the development of social and economic construction, the requirements for safe and stable operation of power systems and reliable supply of power are increasing. By the end of 2015, the national installed capacity of full-scale power generation of China was 1525.27 million kW, an increase of 10.62% over the previous year, and the growth rate was 1.67% higher than the previous year[1]. In 2016, the total electricity consumption of the whole society was 599.8 billion kWh, an increase of 5.0%[2]. With the increase in demand for electricity, the safe and stable operation of the power system and the reliable supply of electricity have increasingly affected the development of the national economy and the social stability.

According to the International Electrotechnical Commission (IEC) standard, circuit breaker is a mechanical device that capable of making, carrying and breaking currents under normal circuit conditions, and has the ability to make, carry for a certain period of time and break fault current[3]. As a protection device for the power system, the reliable operation of the high-voltage SF_6 circuit breaker is related to the safety and stability of the entire power grid. In the case of normal operation of the power system, HVCBs are in close state carrying the normal working current; in the event of a power system failure or other circumstances need to cut off the current, HVCBs will be automatically or manually switched to the open circuit state isolating the fault lines to protect the entire power grid from breakdown. If the HVCB cannot cut off the

fault current quickly, the power system will face serious operational failure and huge personal and property lossed may be caused.

Among all the fault types with which a HVCB confronted, a large number of those were directly related to arcing contacts. According to the final results of the CIGRE (International Council on Large Electric Systems) second international enquiry on the reliability of HVCBs in service[4, 5], it has been found that for the HVCBs of 63kV and above, the failure rate of the arc extinguishing unit (mainly consists of arcing contacts and nozzle[6]) was the highest among all major failures, accounting for 14.0%. Among the minor failures, the failure rate of the arc extinguishing unit also accounts for 9.4% of the total number. As the components directly exposed to arcs in HVCBs, the working conditions and electrical lifetime of arcing contacts determine the reliability and service lifetime of the equipment.

The degradation of arcing contacts in HVCBs is mainly caused by arc erosion[7, 8]. Subject to the heating of the arc, the material of the contact surface will be vaporized violently. Droplet splashing and solid material cracking may also occur under certain conditions. Figure 1.1 shows the surface morphology of the copper and copper-tungsten contacts after being eroded by the arc. The metal material leaving the contact surface during the erosion process will eventually adhere to the inner wall of the nozzle and the components connected to the contact, which may result in a reduction in the insulation level of the device. Arcing erosion can also lead to the deformation of the contact surface, the shortening of the contact length and the change of the contact surface structure, which will seriously affect the short-circuit current breaking capacity and the overall electrical life of the HVCB.

(a) Cu Contact (b) CuW Contact

Fig. 1.1 Surface morphology of arcing contacts after current breaking in a HVCB

Research on the mechanisms and prediction methods of the arcing contact erosion of HVCBs can deepen the understanding of the physical process of current breaking, and provide theoretical and experimental basis for the condition monitoring and life time prediction of the HVCB. Through experimental investigation, the deterioration trend of the HVCB can be monitored, the potential faults can be discovered in advance, and the operating cost of the power system can be finally reduced. Thus, monitoring the arcing contacts erosion is of great significance to improve the safety and reliability of power systems.

1.2 State-of-the-art and Existing Problems of Arcing Contacts Erosion of SF_6 HVCB

The erosion of arcing contacts is an inevitable phenomenon during the current breaking process in HVCB which is the result of the interaction between the arc and the arcing contacts. During the development of HVCB, various of arc extinguishing mechanisms have been designed. In general, the arc has always been through the phases of burning, developing and extinguishing. In the research area of arcing contacts erosion, a lot of theoretical and experimental research work have been carried out by researchers from worldwide. However, due to the diversity of research background, in most cases, the problem of arcing contact erosion is simplified to varying degrees. Therefore, further investigation is necessary to gain deeper understanding of the process of arcing contact erosion which can be utilized for condition monitoring.

1.2.1 Theoritical Calculation and Modeling of Arc Plasma

Characteristics of arc plasma is an important aspect that affects arcing contacts erosion. The arc is a collection of microscopic charged particles whose macroscopic properties are closely related to the internal microscopic processes and are the external manifestations of the collective behavior of the microscopic particles that constitute the arc. At high temperature, the physical properties of arc plasma are difficult to be measured experimentally. Theoretical estimation is a common research method. From the microscopic point of view, the research mainly involves the calculation of physical

parameters of arc plasma; from the macroscopic point of view, the research focuses on the establishment and simulation of the magnetohydrodynamic model of the arc.

The calculation of physical parameters and magnetohydrodynamics simulation of the arc can provide necessary theoretical support for the study of contacts erosion. Gleizes[9] and Murphy[10] have carried out thorough reviews of the calculation and simulation theory of arc plasma, including the plasma equilibrium composition[11], thermodynamic parameters[12], particle transport coefficients[13] and the radiation transport coefficients[14], and the establishment of the magnetohydrodynamics model (including the mass conservation equation, the momentum conservation equation, the energy conservation equation and the Maxwell equations)[15]. Through the simulation, the temperature, pressure, velocity, electric field and magnetic field distribution of the arc can be obtained. The simulation results can help to understand the arcing process quantitatively under different conditions and offer technical support of the optimal design of the circuit breakers.

In the earlier papers, the researchers only considered the characteristics of the gaseous particle of the arc, ignoring the possible effects of metal vapour on the arc[16, 17]. With the continuous advancement of theory study, the researchers realized that the metal vapour produced from the contacts erosion had a significant effect on the characteristics of the arc. The properties of arc considering the effects of metal vapour were calculated[18–21].

As shown in Figure 1.2, the relative change of the thermaodynamic properties (density, specific enthalpy, specific entropy and isothermal thermal capacity) of SF_6-Cu mixture with various Cu ratio have been demonstrated. When the ratio of copper vapour is 50% and the temperature is 1500K, the relative change of density is over 50%, and the relative change of specific enthalpy is more than 15%. The relative changes of specific entropy and isothermal heat capacity both reach 20%. Zhang[21], Liau[22] and Lee[20] built up two-dimensional axisymmetric models of arc and contact, and the arc plasma properties were studied considering the existence of metal vapour. It is shown that the presence of metal vapour reduces the arc temperature and improves the net radiation coefficient and conductivity of the arc.

At present, most computational studies related to high temperature plasma are based on the assumption of local thermodynamic equilibrium (LTE) and axisymmetry[20–22].

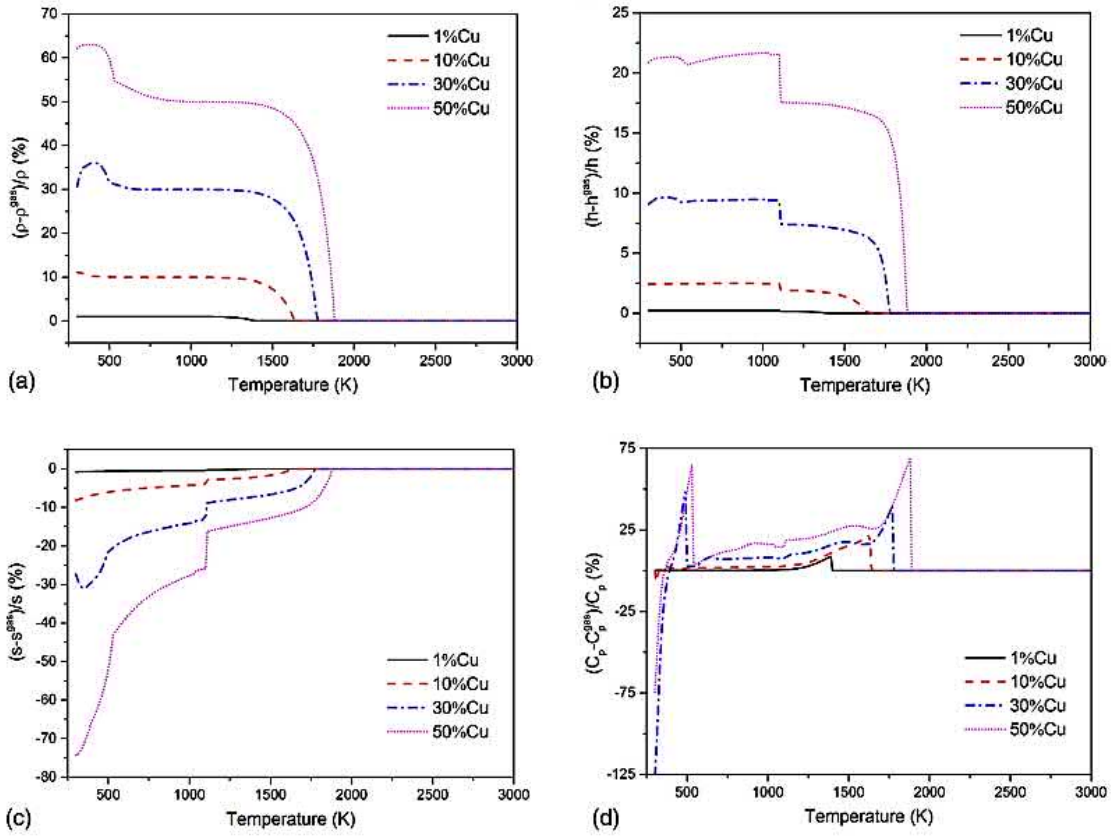

Fig. 1.2 Relative difference between calculated values of thermodynamic properties with and without consideration of the condensed phases in different SF_6–Cu mixtures at temperatures of 300–3000 K and a pressure of 0.1 MPa. (a) Mass density, (b) specific enthalpy, (c) specific entropy and (d) specific heat at constant pressure.[19]

When LTE is assumed, the temperature of electrons and heavy particles are the same, atomic ionization obeys the Saha thermal ionization equation, the atom/ion excitation obeys the Boltzmann equation and radiation obeys the Planck radiation law, and calculations can be easily carried out. However, the state of actual plasma (such as switching arc, welding arc, heating arc, etc.) is deviated from the LTE assumption. Especially, for the erosion region near the arcing contact surface, the temperature gradient is very large, the concentration of positive ions is difference from negative ions, the deviation from LTE is even larger. Meanwhile, subject to the computing speed of computers, researchers often use axisymmetric model to reduce the computing time. For the breaking arc in HVCB, since the duration of the arc is only a few tens of milliseconds and the arc is completely enclosed in the arcing chamber, it is difficult to observe the arc behaviour directly. For the actual arc breaking process, it may

be affected by a number of random factors. By observing the ablation marks on the contact surface of HVCB, it can be inferred that the contact erosion process was not axisymmetry[23].

In conclusion, the simulation model is often unable to give a convincing prediction of the arc erosion process in practical devices. In order to improve the existing theoretical models and provide an accurate description of the arc erosion process, it is helpful to further study the behaviour and evolution of the arc in HVCB during current breaking process and explore the new factors effecting the arc characteristics.

1.2.2 Mechanisms of Arcing Contacts Erosion

From the perspective of arcing contacts, lots of theoretical and experimental work have been done by researchers from worldwide.

Establishing the energy balance equation at the contact surface is the basic starting point for exploring the erosion of arcing contacts. Scholars have established many simulation models based on the energy balance of the contact surface, which can be used to calculate the parameters such as the contact surface temperature, the material transfer rate and the mass loss under various conditions. Holm had stated in his paper[24] which published in 1949 that during the process of current breaking, the energy generated by the arc can not be completely consumed through the heat transfer inside the arcing contact while part of the energy of the arc was carried away in the form of material evaporation. The energy balance equation of the contact surface was established, and the mass loss rates of the contact under different currents and materials were estimated. Wilson[25] studied the contacts erosion of high current and found that the erosion mechanisms of low current is not applicable at high currents. The erosion characteristics of different materials under high current were also compared. It was concluded that the contact material evaporation is the main form of mass loss, and the droplets ejection driven by the evaporation is secondary. Ecker[26] analysed the problems such as the continuity of the current on the contact, the voltage drop of the contacts, the energy balance of the contact surface and the plasma jet on the contact surface during the arc which laid the foundation for the follow-up theoretical research. Zhou[27–29] formulated a theoretical model of the arc cathode attachment region. From the theoretical calculation, it was found that the loss of the contact

material was mainly caused by the bombardment of the positive ion in the case of small current. In the case of high current, the thermal electron emission plays an important role in the energy balance of the contact surface. Tepper[30] studied the properties of CuW contacts in HVCB experimentally and established a zero-dimensional model based on the energy balance which can be used for mass loss prediction of HVCB. Nakagawa established a one-dimensional model in the literature[31], simulated the erosion characteristics of copper-tungsten materials at different mixing ratios, and found that the latent heat of vaporization of metallic copper has a great influence on erosion. Zhou established another relatively complex one-dimensional model in the literature[28], and discussed the temperature distribution of the contact surface, the plasma temperature and the current density as a function of current under steady-state DC conditions.

The factors affecting the mass loss of the arcing contacts are manifold. Donaldson[32–34] discussed in detail the factors that affecting contact erosion, analysed the mass loss mechanisms of different types of material and proposed that when the charge transfer is less than 25C, the mass loss of the contact is proportional to $Q_e I_p (t_p)^{1/2}$, where Q_e is the effective charge transferred, I_p is the peak current and t_p is the current pulse width. Walczuk[35] further summarizes the factors that affecting the contact erosion which can be divided into physical parameters, switching conditions, construction of contacts and quenching systems. Specifically, he studied the relationship between contact mass loss and the testing numbers, the product integral of arc current and time, and arc energy qualitatively and quantitatively. Teste[36] studied the influence of eletrode gap on cathode erosion experimentally. When the electrode gap was large, the mobility of the arc was high and heating from the anode plasma jet on cathode surface was low reducing the mass loss of cathode. Borkowski studied the influence of contact size[37] and electrode material[38] on erosion by using ANASYS simulation software. It was found that when the current was small and the contact size was large, the diameter of the contact had little effect on erosioin. However, when the arc diameter and the diameter of the contact were equivalent, the size of the contact was closely related to the degree of erosion. Shea[39] compared the erosion characteristic of AgW contact of different proportions. It was found that the closer the theoretical calculation and the actual material density, the lower the mass loss. It was also pointed out that the

current density and the size of the contact both have an important effect on erosion. Shea[7] summarized the contact erosion theories in the range of 3kA to 22kA, and the factors that affecting contacts erosion (Table 1.1).

Table 1.1 Factors affecting contacts erosion[7]

Categories	**Factors**
Electrical parameters	Arc energy, Current, Phase angle at part, Arcing time, Charge etc.
Contact parameters	Material properties (melting temperature, boiling temperature, density, electrical conductivity, thermal conductivity), Processing methods, Contact shape, Contact dimensions, Number of Phases etc.
Device parameters	Opening speed, Arc stability, Arcing gap distance, Quenching mechanisms, Heat sinking, Gas flow, Arc shape etc.

The mass loss of the arcing contacts of the HVCB is not a linear function of the arc current. Turner[40–42] had found that for the same contact material, the mass loss is not a continuous function of the arc current and there is a critical current. In the vicinity of the critical current, the mass loss increases sharply which coincides with the current value that causes the bulky melting of contact material. Wilson discovered through experiments that the magnitude of the current has an important influence on the change of the erosion mechanisms of the arcing contacts, and compares the erosion characteristics of different materials at high current. It is pointed out in the conclusion that the evaporation of the contact material is the main form of mass loss, and the droplet ejection driven by gas evaporation is a secondary form[25].

In the past investigations, the influence of the change of the surface morphology of the arcing contacts on the erosion process was mostly neglected. In practice, copper-tungsten (CuW) is commonly used as arcing contacts material in HVCB. Copper is used for providing better electrical conductivity and thermal conductivity, and tungsten has a high melting point forming the skeleton of the contact reducing the mass loss. These two materials are generally mixed with each other using a sintered technique and their microscopic physical properties remain independent. This property results in the material with low melting temperature being vaporized during the arc and the

other material remaining on the surface of the contact. After several times of current breaking process, the contact surface will form a unique layered structure[30, 43]. The material of copper and tungsten adjacent to the surface of the contact is no longer uniformly distributed, as shown in Figure 1.3. The top of the surface is re-solidified tungsten which is attached to a tungsten skeleton layer. During the subsequent arcing process, it is difficult for copper inside the contact to escape from the contact surface before tungsten on the surface layer is melted.

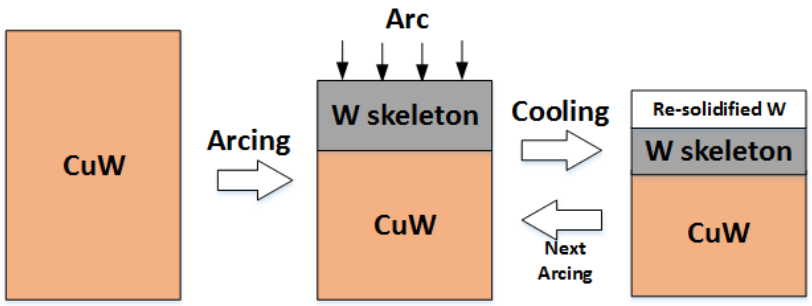

Fig. 1.3 Variation of surface microstructure for CuW contact during arcing[43]

So far, the influence of changes of the contact surface on the erosion process has not been systematically explored. In the published theoretical models of arcing contacts erosion, the contact surface is always assumed to be unchangeable during the arc, and the influence of the 'history of erosion' of the arcing contacts on the subsequent tests is neglected. This type of treatment is acceptable at low current within a certain number of tests, because the shape of the contact surface has not changed significantly. However, for arcing contacts erosion at high current, the calculated contact mass loss result is inaccurate if the surface morphology change is neglected. In this thesis, based on the study of arc and arcing contacts interaction, a noval 3D thermal conduction model is proposed.

1.2.3 Prediction Methods of Arcing Contacts Erosion

In the field of engineering applications, research on the prediction method of arc contact ablation of HVCBs has been a very active topic. According to the working status of the HVCB, the prediction methods are mainly divided into two catagories, i.e. offline monitoring and online monitoring.

In terms of the offline monitoring of arcing contacts erosion, Li[44] from Xi'an Jiaotong University proposed a method which is using travel of contacts, the length difference between arcing contacts and main contacts and the maximum length reduction of arcing contaccts to indicate the operating condition of the HVCB. Wang[45] built up a simple fault prediction system for circuit breakers according to the static loop resistance, arcing contacts dynamic resistance, arcing contacts effective contact time and other circuit parameters. Recently, ABB has introduced an offline overhauling method based on X-ray technology to HVCBs without disassembly[46] which has greatly reduced the power outage time of maintenance.

For on-line monitoring of arcing contacts erosion, parameters recorded in real-time such as the breaking current, arcing time, etc., are used for calculating the remaining electrical lifetime of HVCB. So far, the most commonly used numerical methods for electrical lifetime prediction include charge accumulation method[47], weighted breaking current accumulation method [48], and weighted breaking current accumulation method considering arcing time[49].

Stoving et al.[47] calculated the electrical lifetime of the HVCB using the charge accumulation method according to the following equation

$$Q = \sum_{n} (\int_{0}^{t_n} i_n dt) \tag{1.1}$$

where:

Q — accumulated charge;

n — operation numbers;

t_n — the arcing time of the nth operation;

i_n — the current of nth operation;

t — time.

The core idea of the charge accumulation method is to use the accumulated arc energy to measure the electrical lifetime. Since the arc voltage is essentially constant regardless the current level, the accumulated charge can be used to evaluate the arc energy. However, according to the experimental results from past works, the accuracy of using accumulated arc energy to measure the electrical lifetime was low.

The French power company (Electricite De France, EDF) and Italy's national power company (Ente Nazionale per l'Energia eLettrica, ENEL)[50, 51] found a law of contact

mass loss which is suitable for engineering applications from the study of SF_6 HVCB electrical lifetime.

$$N_{\mathrm{s}} = f(I_{\mathrm{sn}}/I_{\mathrm{b}}) \tag{1.2}$$

where:

N_{s} — equivalent operation numbers;

I_{sn} — rated short-circuit breaking current;

I_{b} — breaking current.

It is illustrated that if the breaking current $\mathrm{I_b} < 0.35\mathrm{I_{sn}}$, the mass loss is much less than those of breaking current $\mathrm{I_b} \geq 0.35\mathrm{I_{sn}}$. However, the effect of arcing time is not considered in this method.

Guan[49] from Tsinghua University proposed a method take the arcing time into consideration which is evolved from the breaking current accumulation method[52]. The electrical lifetime of the circuit breaker is characterized by the amount of contact mass loss, and the influence of the arcing time on the mass loss is taken into account, but the measurement of the arcing time is complicated since the start of the arc can not be located from the curve of current. In addition, the relationship between breaking current and contact mass loss is not simply exponential. When the breaking current is less than the threshold, the weight of current (i.e. a constant represent the effect of current amplitude on contact erosion) will change which is ignored by the weighted breaking current accumulation method considering arcing time. ABB has calculated the residual electrical lifetime using product integral of the breaking current and arcing time ($\mathrm{I_2t}$) in its HVCB on-line monitoring device (Circuit Breaker Sentinel $^{\mathrm{TM}}$, CBS).

In summary, the research on the prediction method of arcing contacts erosion has not yet reached a unified theory. As most of the existing prediction methods neglect the affecting factors such as the movement of the arc root and the structural changes of the contact surface, it is difficult to obtain accurate prediction results. Therefore, new theories and methods need to be proposed to monitor the erosion process of the arcing contacts in real time, thereby improving the prediction accuracy.

1.2.4 Spectroscopic Diagnostics of Arcing Contacts Erosion

The arc radiation spectrum during the current breaking process contains a wealth of information that can be used to monitor the erosion process of the arcing contacts.

Using spectral diagnosis methods, the data of the particle composition of the arc plasma (especially the metal vapor concentration) and the temperature distribution can be measured[53–57]. In the work related to contacts erosion, Okuda[55] has stuided the arc of copper-tungsten contacts in SF_6 spectrally and measured the arc temperature and pressure. The arc voltage calculated from the obtained temperature and pressure profiles agreed well with electrical measurements. In the paper, it was also found that the spectrum of SF_6 gas dominates in an electric arc below 10kA, and the metal vapour dominates in an electric arc over 10kA. Tanaka[53, 58] used a flat type arcing chamber to measure the metal vapour concentration in SF_6. Using the same set of test equipment, it had also found that the continuous spectra dominates the background spectra over the temperature of 4500K and S_2 spectra dominates below the temperature of 4500K. Moriyama[59] calculated the temperature of the copper contact surface by using the Boltzmann method. It was found that the temperature of the cathode surface was lower than that of the anode, and the temperature fluctuation of the cathode surface was small. Rouffet[60] obtained the arc plasma temperature by comparing the measured spectral intensity and the calculated net radiation coefficient at different temperatures of argon in various spectral bands. This method is free from the constraints of precise spectal line intensity measurement and a CCD camera can be used to detect the spatical temperature distribution of the arc plasma. Recently, Franke[61] established a strongly simplified arc radiation model. The spectral line profiles under different temperatures and pressures were obtained through simulation, and the arc temperature was derived through the comparison of measured and simulated spectral line profiles. The dependence on the optically thin condition is no longer required when calculating the temperature of arc plasma.

Griem[62] and Cooper[63] have offered a detailed review of the traditional arc plasma spectroscopy methods. Most of these methods depend on stringent experimental conditions (optically thin, axisymmetric, etc.) and complex mathematical calculations. Due to the lack of necessary data, the accuracy of some of the calculations is low.

The selection and installation of sensors are the guarantee of reliable extraction of signals containing equipment status and the following data analysis. The working environment of HVCB is very harsh and the sensors need to withstand the mechanical vibration, strong electromagnetic field, high temperature and chemical corrosion for a long period of time. The sensors installed inside the arcing chamber need not only to be stable and reliable, but also to be unharmful to the main body of HVCB. Therefore, the optical fibre sensors have become the best choice. Optical fibre based sensors have many advantages such as high sensitivity, immunity to electromagnetic interference, long lifetime and economical, and they have been studied widely in the field of power equipment on-line monitoring, such as temperature sensor[64], barometric pressure sensor[65, 66], vibration signal sensor[67, 68], displacement sensor and ion concentration sensor[66, 69] and so on. Humphries[70] and Tori[71] had proposed two different spectral analysing methods to detect the arcing contacts erosion phenomena and found that the relative spectral line intensities varies when the erosion degree of the arcing contacts are different. The feasibility of using the arc spectra analysis to predict the erosion of the contact is preliminarily verified.

How to use the simple sensor and efficient data processing method to extract the information related to contacts erosion from the spectrum of the arc has become a key point in contacts erosion monitoring. In recent years, a new data processing method being called chromatic method has been increasingly applied to various off-line and on-line monitoring cases[72–76]. In this thesis, the chromatic method is used to process the optical signal of the arc. The reasons causing the changes of erosion will be further analysed in the process of obtaining the quantitative relationship between the spectra and the arcing contact mass loss.

1.3 Structure of the Thesis

In this thesis, the arcing contact erosion phenomenon of HVCB had been studied using the combination of experimental tests and simulations. The law of arc root movement on the contact surface had been discussed. The spectral emission of the arc had been processed and analysed, and the correlation between the chromatic parameters and the contact erosion was discussed quantitatively. The feasibility of arcing contacts on-line

monitoring using chromatic methods was also discussed. Finally, a 3D thermal model of arcing contact erosion was built and compared with experimental data.

This thesis is organized as follows:

In Chapter 1, the research background and significance of arcing contact erosion mechanisms and prediction method of HVCB are introduced. The state-of-the-art and existing problems of arcing contacts erosion are also presented.

In Chapter 2, the construction of the experimental system and the experimental methods are described in detail. First, a HVCB arcing contacts erosion testing system is introduced in detail, including a 245kV/40kA SF_6 live tank HVCB, the gas handling equipment, the main circuit and a synchronising pulse trigger circuit. Second, the optical measuring system is illustrated which is composed of a high speed photography system, a high speed spectrometer unit and a photo-diode amplifying unit. Third, the timing of the experiments and the method of measuring contact mass loss are introduced.

In Chapter 3, the experiments undertaken in this study are tabulated and the experimental data are presented including the mass loss of arcing contact, photographs of arcing contact surface, high-speed photographs of arc column/root, outputs of photo-diode detector units and the time-resolved arc spectra.

In Chapter 4, the macroscopic arc behaviour in HVCB and its effect on arcing contact erosion are reported. First, the macroscopic arc behaviour are studied based on the captured high-speed photographs of the arc including the symmetry of the arc column, the mobility of the arc root and the droplet ejection phenomenon. Second, the quantitative relationship between the mass loss of arcing contact and the effective moving distance of the arc root at low currents is studied for CuW contact using spatial domain chromatic methods.

In Chapter 5, the quantitative relationships between the mass loss of Cu/CuW arcing contact and the arc spectra are studied based on wavelength and time domain chromatic analysis. First, the chromatic analysis techniques are introduced. Then the results of chromatic data analysis are presented and interpreted. Finally, combined with the linear regression method, the quantitative relationship between the chromatic parameters and the contact mass loss is calculated, and the accuracy of the chromatic method and the arc energy method in the prediction of contact mass loss is compared.

In Chapter 6, a 3D thermal model of contact erosion was established considering the movement of the arc root on the contact surface. The temperature distribution, the mass loss and the contact surface deformation of Cu and CuW contacts subjecting to a half-cycle AC current are simulated, and compared with experimental data.

In Chapter 7, the contents of the thesis and the main conclusions are summarized, and the future work is prospected.

Chapter 2

Experimental System and Methods

Arcing contacts erosion in HVCBs is closely related to the arc phenomenon. Observation and measurement of the characteristics of the arc through experimental methods can help to understand the interaction between the arc and arcing contacts and the energy exchange process. So far, many researchers and research institutions have undertaken experiments related to contacts erosion which is aiming for exploring the impact of material properties, equipment parameters and electrical parameters on contacts erosion and, therefore, providing references to the material selection and design of arcing contacts. However, the study of the interactions between the arc and arcing contacts in HVCBs through experiments is rarely reported. Especially, the lack of experimental data obtained directly from industrial HVCBs restricts the development of on-line monitoring systems of arcing contacts erosion.

In this chapter, the construction of the experimental system used for arcing contacts erosion is introduced, including the structure of the testing HVCB, the components of the main circuit, the gas handling equipment, the construction of the high-speed photography platform and the high-speed spectrograph system. Meanwhile, the experimental methods are described in detail, including the timing of the experiments, synchronisation of triggering signals, measurement of voltage and current, measurement of the movable contact displacement curve, capturing of the high-speed photographs of the arc, capturing of the arc spectra, and measurement of the contact mass loss.

2.1 Arc Discharge System

2.1.1 Arcing Contacts

The arcing contacts in a HVCB are generally of two geometries (Figure 2.1) - one is a tulip contact and the other a plug contact which when closed fits into the tulip contact. In this thesis, unless otherwise stated, the diameters of the tulip and the plug contacts are 47mm and 18mm respectively. The tip of the plug contact is cylindrical having a flat surface with 2mm round chamfer and redesigned to be replaceable so that its mass loss can be measured conveniently by weighing before and after each test. Two different types of material were used as the arcing contacts, i.e. Cu and CuW (28wt% copper and 72wt% tungsten). The plug contact was used as the cathode and the tulip contact as the anode at all time. Only the erosion of the plug contact was investigated in this study.

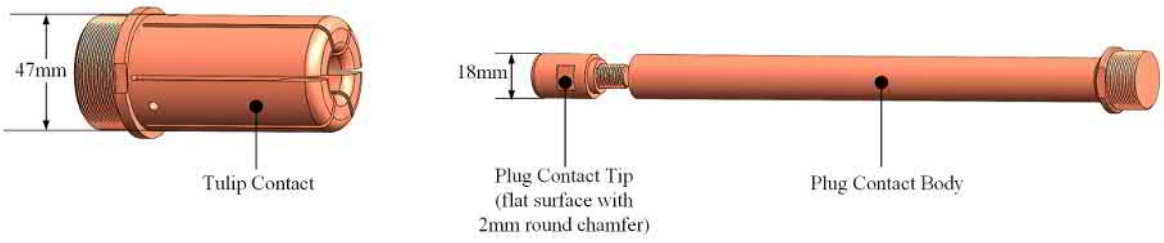

Fig. 2.1 Geometries of arcing contacts.

The material of CuW is a mixture of copper and tungsten. It is widely used as arcing contacts material in power switching devices. As copper and tungsten are not mutually soluble, the material is composed of distinct particles of one metal dispersed in a matrix of the other one. The micro structure is therefore rather a metal matrix composite instead of a true alloy. The material combines the properties of both metals, resulting in a material that is heat-resistant, ablation-resistant, highly thermally and electrically conductive, and easy to machine. The physical properties of metal copper and tungsten are listed in Table 2.1. In addition, the grain size of sintered copper tungsten in this study is 8μm.

Table 2.1 Properties of copper and tungsten.

Parameters	Copper	Tungsten	Unit
Melting Point	1358	3680	K
Boiling Point	2840	6201	K
Latent Heat of Melting	207	192	kJ/kg
Latent Heat of Vaporization	4730	4210	kJ/kg
Density	8.96	19.32	g/cm^3
Heat Conductivity	403	174	$W/(m \cdot K)$
Heat Capacity	385	136	$J/(kg \cdot K)$

2.1.2 Experimental HVCB Unit

The schematic diagram of the structure of the testing HVCB unit is shown in Figure 2.2. This unit represents a modified commercial 245kV/40kA SF_6 live tank self-blast HVCB. It is mainly composed of an breaking unit (upper section) and a support insulator (lower section). The hydraulic driving mechanism, which is connected to the moving rod at the bottom section, is omitted in the figure. The hydraulic mechanism provides the power for driving the moving contact. The opening velocity can be up to approximately 5m/s.

The arcing contacts (Figure 2.1) are mounted within the circuit breaker housing (Figure 2.2), one being fixed and the other attached to a moving hydraulic mechanism. In this study, tests have been made first with the plug contact attached to the hydraulic mechanism (reversed-structure of a HVCB, Figure 2.2(a)), and secondly with the tulip contact attached to the hydraulic mechanism (forward-structure of a HVCB, Figure 2.2(b)). This enabled the stationary contact in each case to be monitored more conveniently. The reversed-structure is generally used when the gas flow is excluded in the tests. For laboratory research, this type of structure is simple and easy to maintain. The plug contact can be dismounted for weighting without the disassembly of the entire arcing chamber. Moreover, the requirement of the output power of the hydraulic operation mechanism is lower than using the forward-structure to reach the same opening velocity. The forward-structure is exactly the same as a commercial HVCB where a expansion volume and a compression volume are included to generate the gas flow cooling the arc. Since the plug contact remains fixed the contact surface can be conveniently observed throughout the contact separation process. Unlike using a

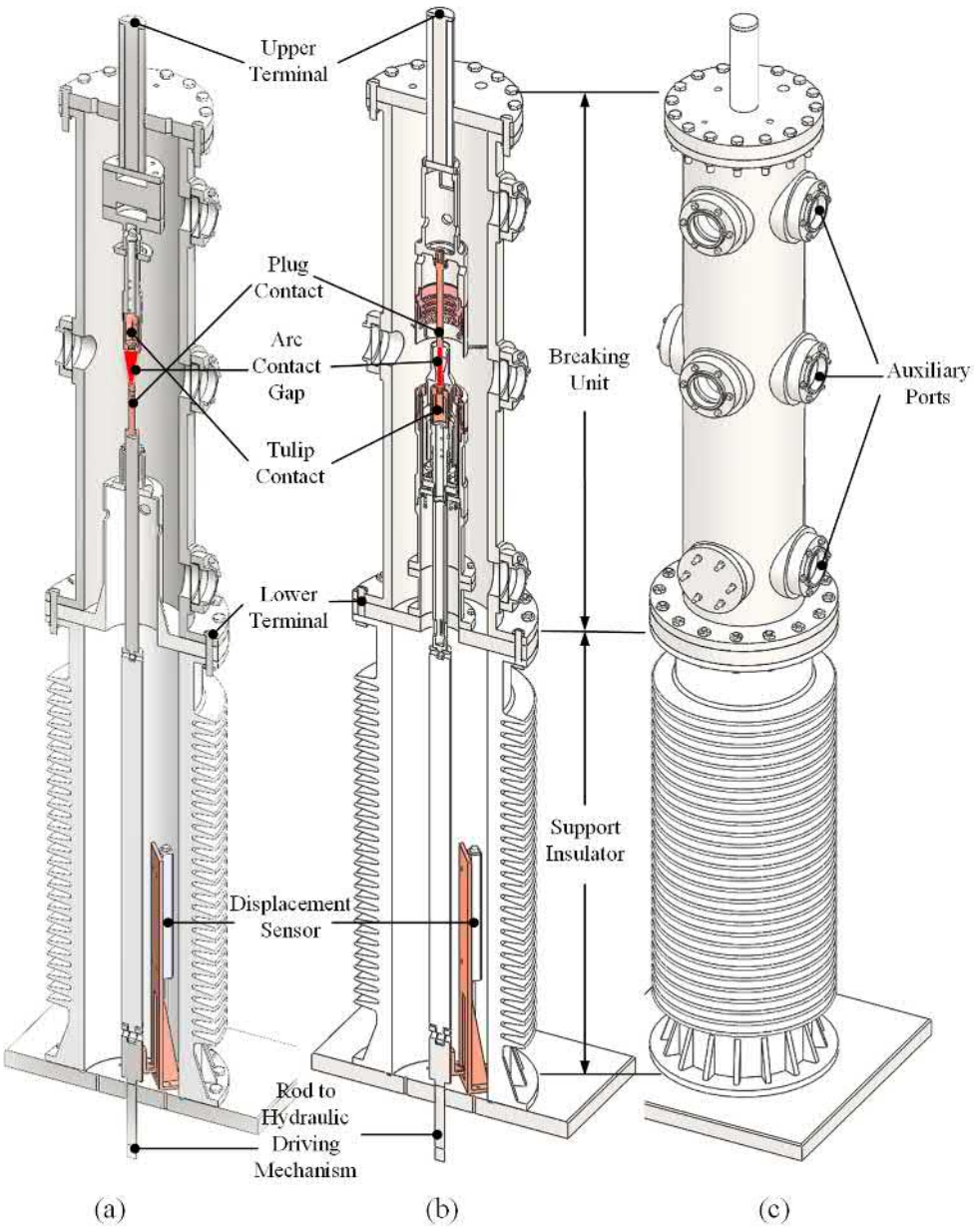

Fig. 2.2 Schematic diagram of the testing HVCB unit, a modified commercial 245kV/40kA SF_6 live tank self-blast HVCB. (a) Cross-section of reversed-structure, (b) cross-section of forward structure, and (c) circuit breaker housing.

ceramic bushing to separate the upper terminal and the lower terminal of an in-service circuit breaker, a steel cylinder with auxiliary ports was used as the arcing chamber of the testing HVCB (Figure 2.2(c)). Instead, a bushing is fixed at the centre of the top lid providing isolation between the upper and the lower terminals. With this change,

the sensor interface and the viewing windows can be easily set up on the metal housing. There are totally seven auxiliary ports located at upper, medium and lower sections of the housing respectively, as shown in Figure 2.2. According to the different purposes of the experiments, the auxiliary ports can be configured as observation windows or sensor ports flexibly. In this study, those three ports at medium level are used as observation windows and the rest as sensor ports. On observation windows, 20mm thick toughened glass are mounted which are able to withstand the heat and shock wave during current breaking. However, for tests using SF_6 as quenching gas, some of the byproducts (e.g. SF_4, SO_2F_2, SO_2, HF etc.) have corrosive characteristics, so that the window glass may be etched after a few tests. Therefore, they need to be replaced to guarantee the visibility when necessary.

The relative positions of arcing contacts in the arcing chamber with and with out a nozzle are shown in Figure 2.3. The moving contact can move vertically along the axis of the arcing chamber. At the open position (Figure 2.3(a), (b) and (c)), the clearance between the stationary and moving arcing contacts is approximately 100mm. During the breaking operation, the total displacement of the moving contact is approximately 200mm. For the structure shown in Figure 2.3(a) and (b) without a nozzle, there is no induced gas flow whereas Figure 2.3(c) and (d) have a gas flow produced by a piston attached to the hydraulic mechanism. Unless stated otherwise, the nozzle is removed to avoid the erosion process being affected by a possible interaction between the arc and the PTFE nozzle material.

2.1.3 Gas Handling Facilities and Methods

During the tests, the arcing chamber is filled with SF_6 (sometimes N_2) with a certain pressure. In the industry, there are strict regulations of the use of SF_6 gas and China is currently following the power industry standard DL/T662-1999 "Specification for SF_6 gas refilling and recovery device." In order to ensure the safety of personnel and avoid the destroying the environment, the SF_6 gas was handled using a professional service cart (model B052R01) produced by Dilo. It is mainly consists of vapour filters, particle filters, gas compressors and vacuum pump. The specific parameters are listed in Table 2.2.

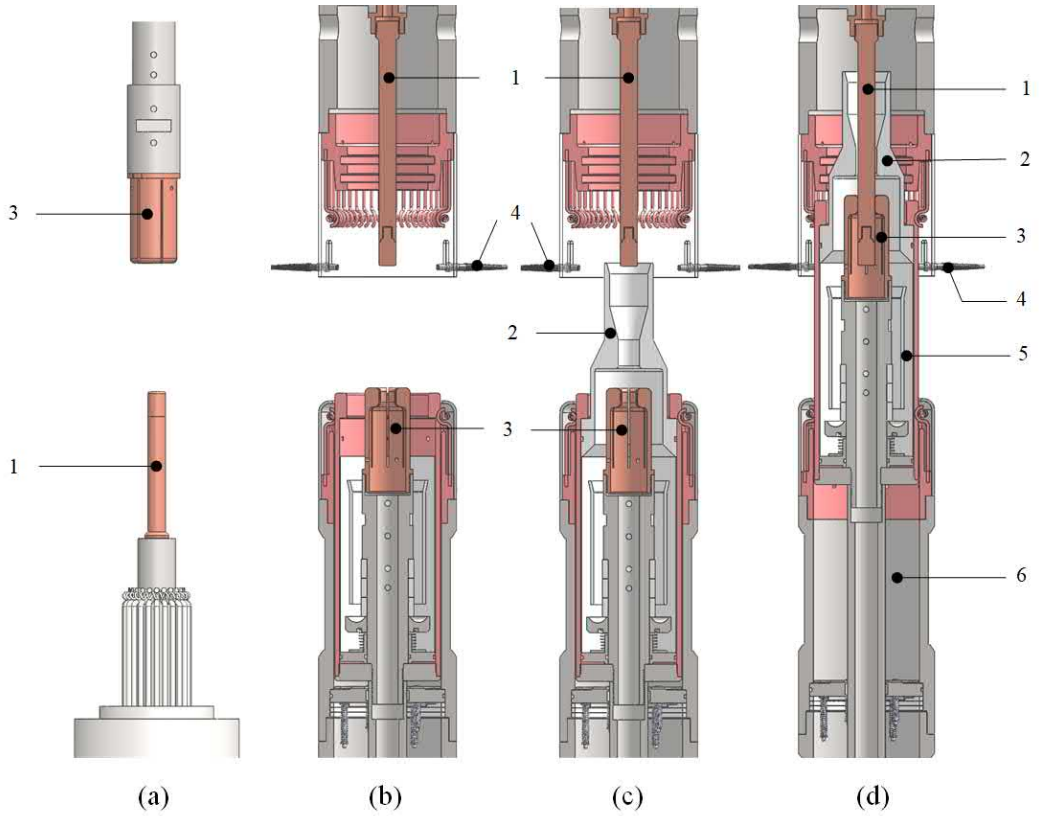

Fig. 2.3 Relative positions of arcing contacts (1. plug contact 2. nozzle 3. tulip contact 4. optical fibre sensor 5. expansion volume 6. compression volume). (a) Moving plug contact, no nozzle open position (b) moving tulip contact, no nozzle open position (c) moving tulip contact, with nozzle open position (d) moving tulip contact, with nozzle closed position.

Table 2.2 Main parameters of SF_6 gas service cart Dilo B052R01.

Items	Parameters
Compressor Displacement	11.4m^3/h
Compressor Working Pressure	23bar
Number of Particle Filter	2
Number of Vapour Filter	2
Pressure Gauge	0-25bar
Vacuum Pump Displacement	5.2m^3/h
Vacuum Pump Ultimate Pressure	50mbar

The schematic diagram of the piping of the gas handling system is shown in Figure 2.4. All the gases is filled and vented through the main valve of the testing HVCB. In branch 1, an oil/gas filter is connected in series to protect the vacuum pump

from contaminants. The sodium solution bucket is used to eliminate the possible acidic components in the exhaust gas. The particles/vapour filters in branch 2 are used to filter the suspended particulates and water vapour in the recycled SF_6. Branch 3 is used for inflation where different types of gas cylinders, such as SF_6, N_2 and CO_2 can be connected.

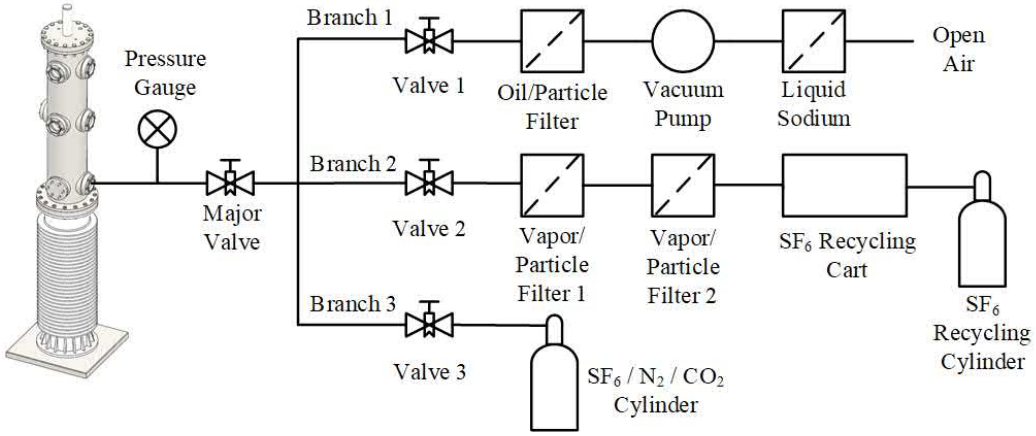

Fig. 2.4 Piping of the gas handling system.

Before each test, the following procedure is performed to handle the gas in the testing HVCB chamber:

(1) Check the airtightness of the HVCB chamber.

(2) Vacuumize the HVCB chamber down to the pressure of 50mbar through the vacuum pump in branch 1.

(3) Fill the chamber with dry N_2 to the pressure of 1bar and keep it still for a period of time letting the water vapour thoroughly mix with N_2.

(4) Repeat step (2) once.

(5) Fill the experimental gas accordingly to the predefined pressure through branch 3.

If SF_6 is used in the test, the following procedure need to be performed to recycle the discharged gas after each test. The purity of recovered SF_6 gas will be tested and can be reused for subsequent tests if meet the requirements.

(1) Recycle the SF_6 gas through branch 2 into the gas recycling cylinder.

(2) Fill the chamber with dry N_2 to the pressure of 1bar and keep it still for a period of time letting the residual gas thoroughly mix with N_2.

(3) Vacuumize the HVCB chamber down to the pressure of 50mbar through the vacuum pump in branch 1.

(4) Repeat steps (2) and (3) once.
(5) Fill the chamber with dry N_2 to the pressure of 1bar and then the chamber can be safely opened.

The recovered SF_6 is tested and, if it meets the purity requirements, it can be used again for subsequent experiments. If other gases (such as N_2 and CO_2) are used, the above step (1) can be simply replaced by the vacuumizing of the arcing chamber of HVCB using branch 1, and step (4) can be omitted.

2.1.4 Main Circuit and Control Unit

Figure 2.5 shows the main circuit of the experiments. It consists of a capacitor bank, a charging circuit and a discharging/testing circuit (including dump circuit, test current trigger circuit and testing circuit breaker).

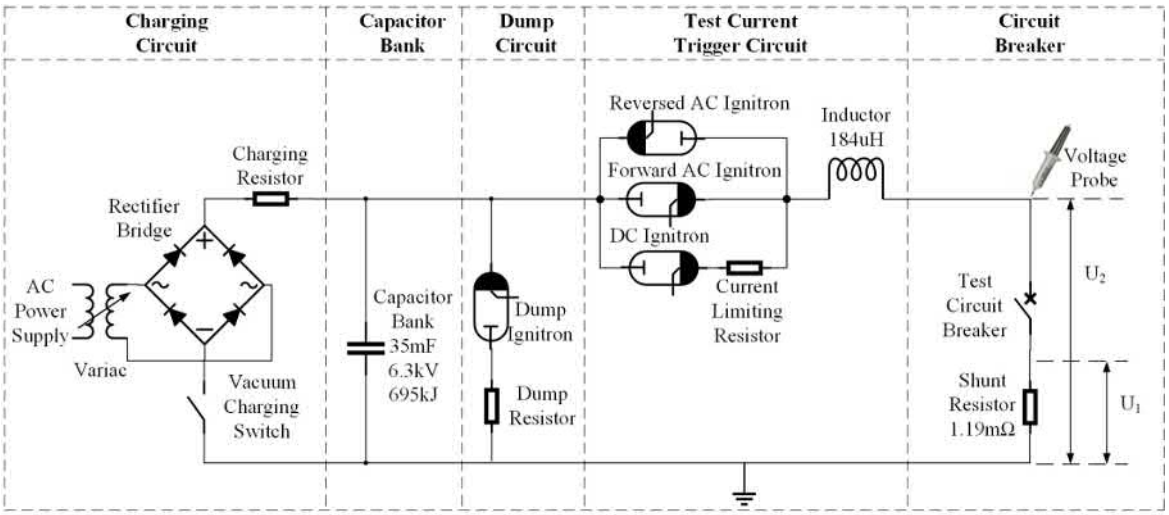

Fig. 2.5 Schematic diagram of the main circuit.

The capacitor bank is used as the power source of the arcing current. It has a capacitance of 35mF, a maximum charging voltage of 6.3kV and a maximum stored energy of 695kJ.

The charging circuit for the capacitor bank mainly includes a variac, a rectifier bridge, a vacuum switch and a current-limiting resistor. The charging voltage can be manually adjusted through the variac, so as to have a relatively constant charging current. Once the voltage of the capacitor bank reaches the preset value, the vacuum charging switch will be automatically cut off and the charging process is completed.

The discharge circuit is a RLC resonant circuit. Since the capacitance of the capacitor bank is 35mF and the inductance of the inductor is 184μH, the designed resonant frequency of the circuit is approximately 60Hz. However, due to the scattering of the parameters of analogue devices, the measured current half cycle time of the resonant circuit is approximately 9.5ms (53Hz) rather than 8.3ms (60Hz). The component used for controlling the current on and off is called ignitron, which is similar to a power thyristor. There are totally four ignitrons in the circuit which are a DC ignitron, a forward AC ignitron, a reverse AC ignitron and a dump ignitron. These ignitrons can be triggered by voltage pulses at selected time instances. The current branches of DC ignitron, forward AC ignitron and reverse AC ignitron can work separately according to the trigger sequences. For the consideration of safety, the residual charge on the capacitor bank will be released through the discharge resistor by controlling the dump ignitron when a test is finished.

The arc current and voltage were measured using a shunt resistor of $R_s = 1.19m\Omega$ and a high-voltage probe (Tektronix P6015A) respectively, and recorded using a digital oscilloscope (Tektronix DPO 2024). The high-voltage probe has a maximum input voltage of 20kV DC/40kV peak, a bandwidth of 75MHz and a attenuation ratio of 1000:1. The digital oscilloscope has four input channels, the bandwidth is 200MHz, sampling rate 1GS/s and maximum recording length 1M points. The arc current I_arc is equal to the measured voltage U_1 divided by the resistance R_s of the shunt resistor, and the arc voltage is the difference between the measured voltages U_2 and U_1.

The displacement of the moving contact of the HVCB is measured using Honeywell linear displacement transducer LF2S12N5KB6A which is installed at the bottom of the circuit breaker, connected to the moving rod of the hydraulic operating mechanism, as shown in Figure 2.2. The linear displacement transducer has a maximum mechanical travel of 12 inches, total resistance of 5kΩ, linearity of 0.1% and dielectric strength of 1000Vrms. The transducer is powered by an external 5V voltage source and the output is recorded by the digital oscilloscope DPO2024.

The control unit of the system is mainly composed of a linkage check module, a charging control module and a trigger control module. The linkage check module is mainly responsible for ensuring the doors leading to the testing site are closed, the ground terminal is disconnected and the water cooling switches for the ignitrons are

on. The charging control module is used to control the charging current and set the charging voltage. It will cut off the current automatically once the preset voltage of the capacitor bank is reached. The trigger control module is used to control the timing of the experiments to ensure that the ignitrons and measurement equipment are triggered precisely at the preset instants. The specific time settings are described in detail hereinafter.

2.2 Optical Measuring System

In this investigation, the optical measurement system mainly consists of a high-speed camera (HSC), a single-channel high-speed spectrometer (HSS) and a multi-channel photodiode detector unit (PDD).

2.2.1 High-speed Camera System

Depending on the different purposes of the experiments, the arc can be shot from different view angles. Two different configurations of the HSC systems are used as shown in Figure 2.6 and 2.7, respectively.

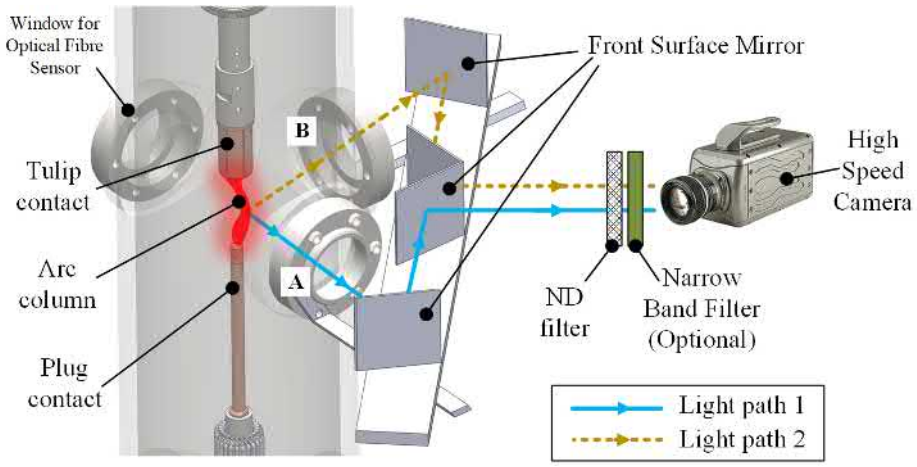

Fig. 2.6 High-speed camera arrangement for capturing light from the arc column along two perpendicular, radial directions.

The configuration shown in Figure 2.6 uses the reversed-structure of the HVCB (Figure 2.2(a)). Under this structure, the HSC and the observation windows are at the same height, and there is no extra mechanical parts blocking the arc light. The arcing

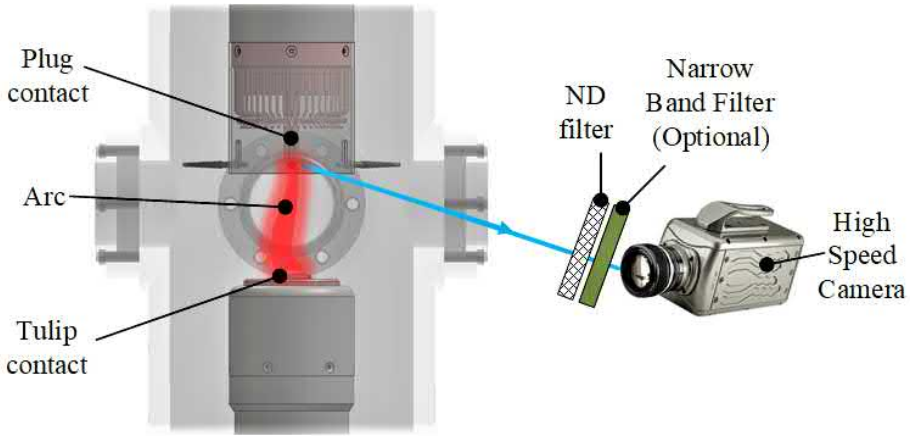

Fig. 2.7 High-speed camera arrangment for capturing of arc root movement.

process between the arcing contacts can be captured clearly. Since the brightness of the arc is extremely high, a neutral density (ND) filter is mounted in front of the camera lens to prevent the image sensor from being saturated. By installing a narrow band filter (522nm±2nm) in front of the camera lens, only the light emitted from copper atoms is allowed to be captured. Therefore, the relative distribution of copper vapour and its variation over time can be obtained. In addition, the use of four front coated mirrors enables the arc column to be observed in two perpendicular directions (Figure 2.6), so as to achieve the purpose of verifying the symmetry of arc columns.

The configuration shown in Figure 2.7 uses the forward-structure of the HVCB where the plug contact is fixed. The lens of the HSC is focused on the surface of the plug contact with a dip angle enables the details of the arc root movement on the contact surface to be captured.

The HSC used in the experiments is Phantom V7.1 and its main parameters are shown in Table 2.3.

2.2.2 Optical Fibre Measuring System

The schematic diagram of the optical fibre based measuring system is shown in Figure 2.8, which is mainly composed of three optical fibre sensors, a ND filter unit, a HSS, a PDD unit, a digital oscilloscope, a computer and the main control unit (MCU).

The system has two main functions: on the one hand, the use of the HSS can capture the visible spectra of the arc; on the other hand, the use of the PDD unit enables the

Table 2.3 Main parameters of the high-speed camera Phantom V7.1.

Items	Parameters
Maximum Resolution	800×600
Framerate per Second	4800(@max resolution), 150000(@min resolution)
Recording Time	1.2s(@max resolution)
Shutter Speed	Minimum 2μs
Triggering Mode	TTL
Image Sensor	SR-CMOS
Lens	Nikon 24-85mm F2.8 macro zoom lens

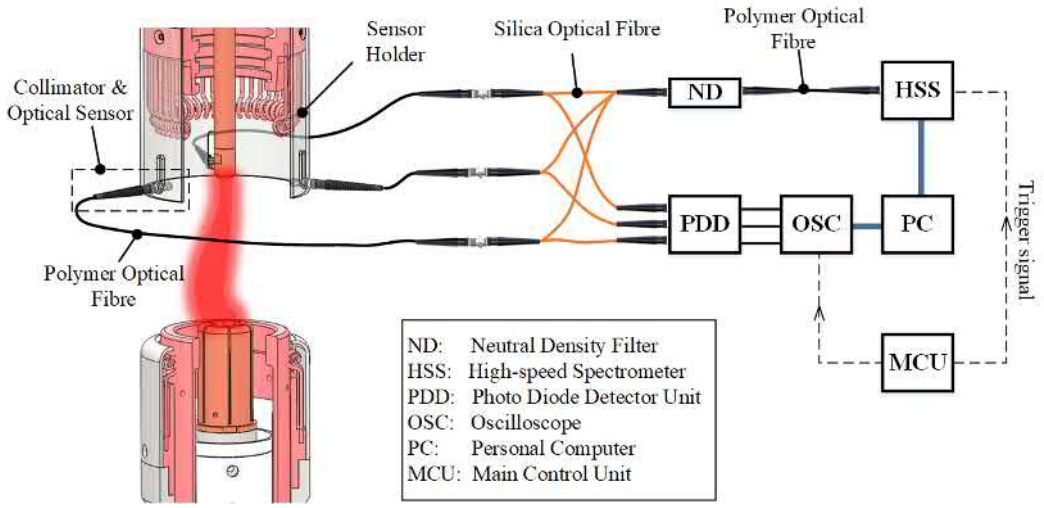

Fig. 2.8 Schematic diagram of the optical fibre measuring system.

trajectory of the arc root on the contact surface to be monitored quantitatively. The start of the data acquisition of the HSS and the oscilloscope is controlled through a pulse trigger signal from the the MCU.

The three optical fibre sensors are mounted on the sensor holder at the same height of the plug contact surface. The arc spectral signal is transmitted through the polymer optical fibre to the optical measuring devices (i.e. HSS and PDD unit) outside the HVCB housing. It is noteworthy that, due to the corrosive property of the decomposition byproducts of SF_6, only the polymer optical fibre, which is anti-chemical corrosion, can be used inside the HVCB.

Fibre Optic Sensors

Figure 2.9 illustrates the optical arrangement of the fibre optic sensors to which the photodiode detectors and high-speed spectrometer connected.

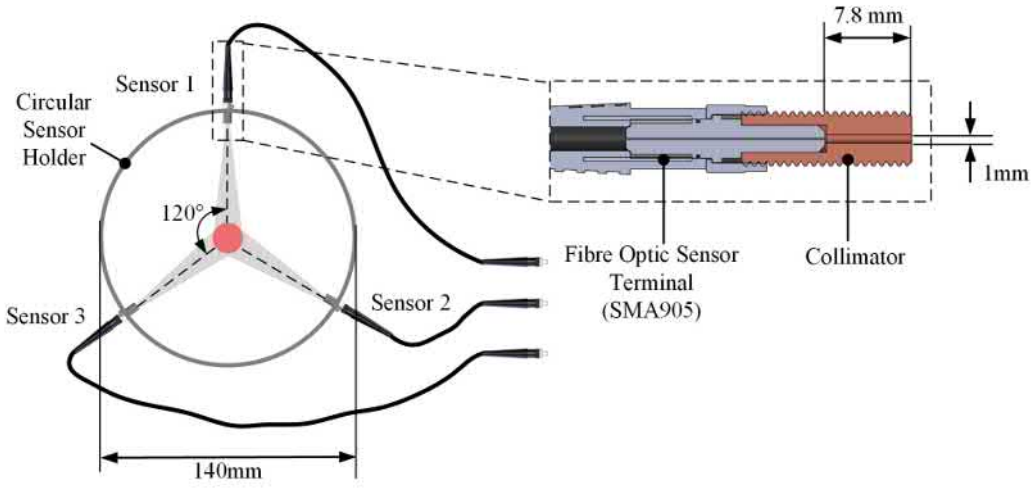

Fig. 2.9 Dimensions and arrangement of the fibre optic sensors.

The outer circle represents the holder of the sensors and the filled red circle indicates the surface of the plug arcing contact where the arc root moves on. In the horizontal plane align with the plug contact surface, there are three fibre optic sensors mounted on the circular sensor holder (diameter 140mm). The sensors are deployed in the plane of the plug contact tip with their axes (dash line) mutually inclined at 120° and the shadow area represents their response range. The fibre optic sensor mainly consists of a SMA905 connector and collimator. The length of the collimator is 7.8mm and the inner diameter is 1mm. The collimators are carefully calibrated to limit the scope of incident light to the area of the plug contact diameter and align with the axis of the contact.

High-speed Spectrometer

The HSS is Exemplar LS produced by BWTek^{TM} and its main parameters are listed in Table 2.4. It is a small CCD spectrometer optimized for low straylight by utilizing an unfolded Czerny-Turner spectrograph. It features on board data processing, USB 3.0 communication, and temperature compensation. Additionally, the Exemplar LS features a 2048 element detector and build-in 16-bit digitizer with greater than 2.0MHz

readout speed. In order to calibrate the output of the spectrometer, a Tungsten Halogen calibration lamp HL-2000-CAL produced by Ocean Optics was used.

Table 2.4 Main parameters of high-speed spectrometer Exemplar LS.

Items	Parameters
Detector Type	CCD
Spectral Range	200nm - 850nm
Detector Pixel Format	2048×1
Detector Pixel Size	14μm×200μm
Digitizer Resolution	16-bit, 65536:1
Data Transfer Speed	≥900 spectra per second in Burst Mode
Integration Time	Minimum 1ms, 1050μs in Burst Mode
Trigger	TTL
Slit Dimensions	25μm width, 1mm height
Spectral Resolution	∼0.6nm
Signal to Noise Ratio	∼295

Photo-diode Detector Unit

The PDD unit is a home-built equipment and the core components are the rapid response photodiode HAMAMATSU S5972 and the logarithmic amplifier AD8304 producted by Analog Devices. The response wavelength range of S5972 is 320nm-1000nm with an average sensitivity of approximately 0.5A/W which meets the requirements of the arc radiation detection. The dynamic range of AD8304 is up to 160dB which is optimized for fiber optic photodiode interfacing without using additional ND filters. The relationship between the output voltage of AD8304 V_{out} and the photodiode output current I_{pd} is shown as below[77]

$$V_{out} = 0.2V \times log_{10}(I_{pd}/100pA) \tag{2.1}$$

Since the output current of the photodiode is proportional to the intensity of the incident light, the incident light intensity can be derived from substituting the the output voltage of AD8304 into Equation (2.1).

Optical Fibres and Coupling

The optical fibres used in the system are 400μm multimode step-index glass optical fibre (AC01287-12) and 1000μm polymer optical fibre (GK-40) produced by Eska^{TM}. The characteristics of the optical fibres are listed in Table 2.5. The attenuation profiles of theses optical fibre are shown in Figure 2.10.

Table 2.5 Characteristics of optical fibres.

Parameters	AC01287-12	GK-40
Core Material	Silica	PMMA
Core Diameter	400 $\pm$ 8 μm	980 $\pm$ 60 μm
Cladding Material	Polyurethane	Fluorinated Polymer
Cladding Diameter	425 $\pm$ 10 μm	1000 $\pm$ 60 μm
Numerical Aperture	0.37	0.5
Refractive Index Profile	Step Index	Step Index

As can be seen from the graphs that the attenuations of the optical fibres are not constants against wavelength. The relative intensities of the spectra lines will be distorted and they should be compensated according to the attenuation curves.

In order to flexibly merge and split the outputs of the fibre optic sensors, three different types of fibre optic terminals are used as shown in Figure 2.11. Since the core diameter of the polymer optical fibre (GK-40) is 1000μm and the glass optical fibre (AC01287-12) is 400μm, one piece of polymer fibre or three pieces of glass fibre can be fitted into one metal substrate with inner diameter of 1100μm (Figure 2.11(a) and (c)). By coupling the single-core polymer fibre with the three-core glass fibre (they have the same light receiving areas), the spectral signal can be merged ("three-to-one") or split equally ("one-to-three") which enables the optical measuring system to be constructed conveniently.

Figure 2.12 shows the detailed connection of the fibre optical path, where the pattern connected to the dashed line represents the type of the fibre optic terminal (Figure 2.11). Single-core polymer terminals are used at the sensors positions. The outputs of each sensor are split equally into three identical routes: the first one is connected to the PDD unit directly; the second one is merged using the "three-to-one" coupling bundle and connected to the HSS; the third one is reserved in this study. At

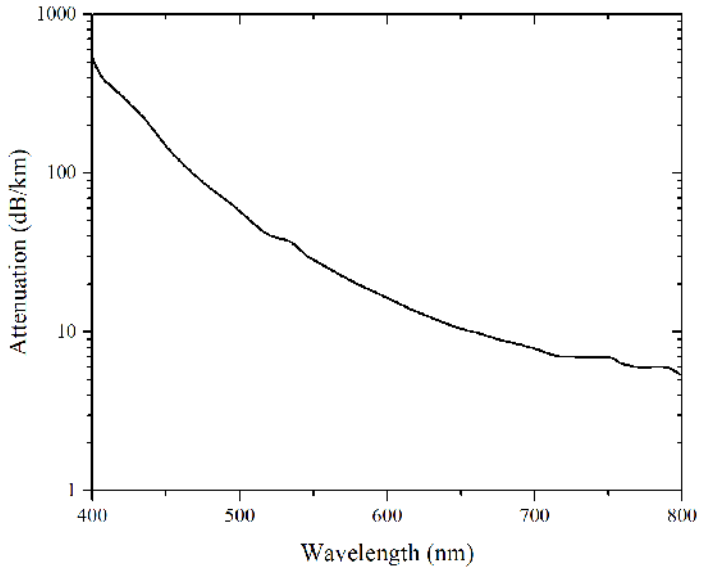

(a) glass optical fibre AC01287-12

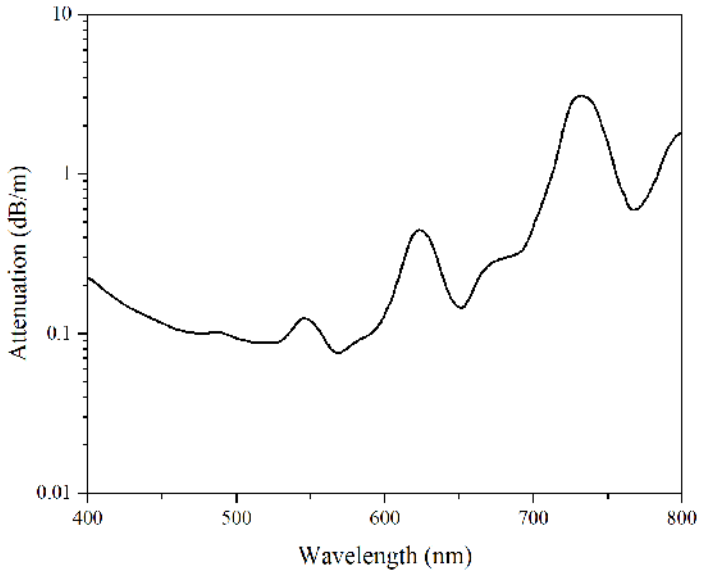

(b) polymer optical fibre GK-40

Fig. 2.10 Attenuation profiles of optical fibres

all coupling points, index matching gel was used to reduce the optical reflection and refraction.

It is worth noting that, in principle, each of the three sensors fixed on the circular holder can deliver spectral signal to the spectrometer, however, due to the movement of the arc root, the radiance of the arc in different radial directions varies which may increase the uncertainty of the spectral measurement. By using the superposition of

(a) single-core polymer fibre optic terminal

(b) single-core glass fibre optic terminal

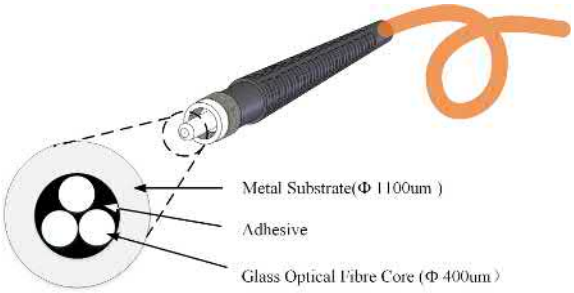

(c) three-core glass fibre optic terminal

Fig. 2.11 The design of optical fibre terminals

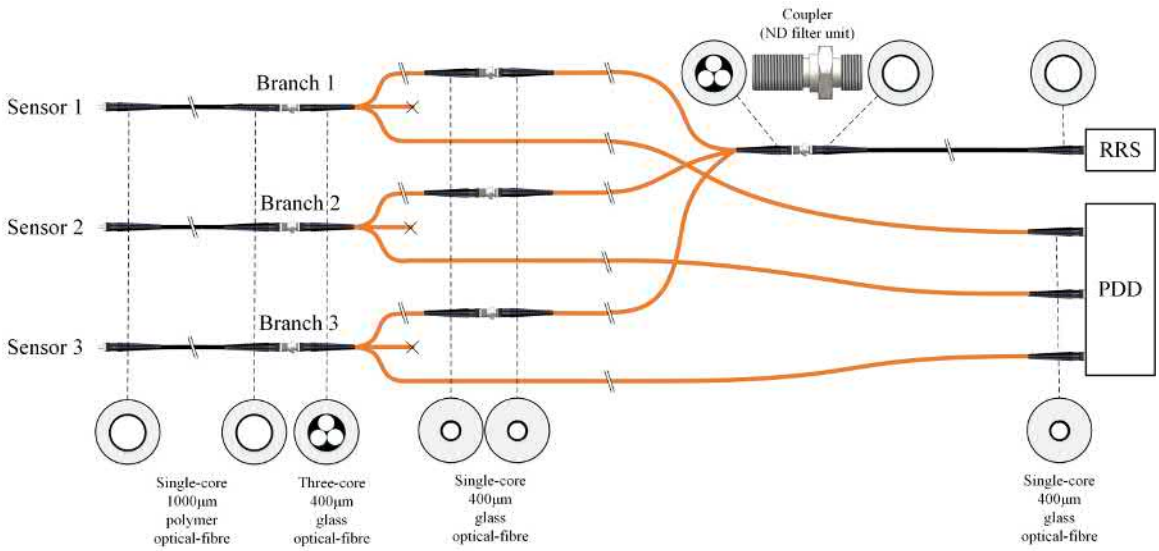

Fig. 2.12 Connection diagram of the optical fibre.

the spectral signals from three different radial directions, the influence of the arc root movement on the spectral signal measurement can be effectively reduced.

Neutral Density Filters

At different currents, the magnitude of optical emission from the arc varies largely and different numbers of ND filters are required to achieve the maximum resolution of the HSS without saturation. Figure 2.13 shows the transmittance curves of the ND filters. Though the transmittance of the ND filters in the wavelength range from 400nm to 700nm are relatively constant with small fluctuation, it will also introduce errors to the spectral data. Thus, before detailed analysis, the captured spectra should also be corrected. It is remarkable that at wavelengths greater than 675nm, the transmittance of the ND filters are very high which will result in inevitable saturation of arc light (the integration time of the HSS is 1050μs which can not be changed). Therefore, the spectral data greater than 675nm should be excluded during data processing.

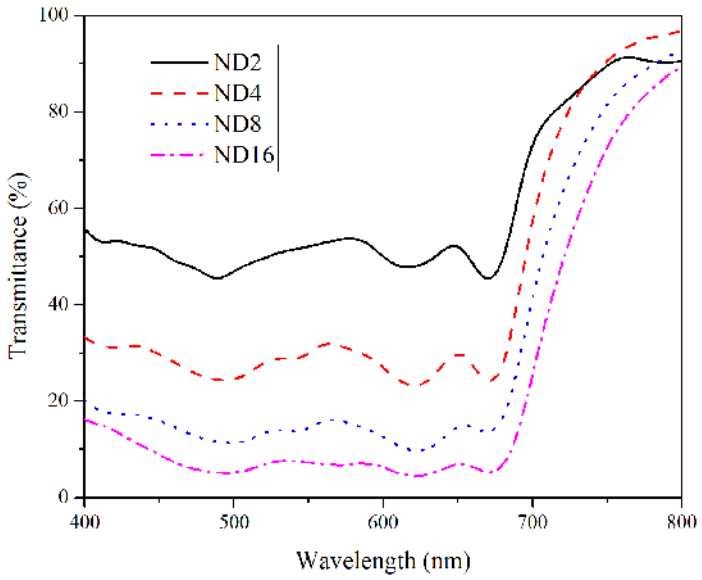

Fig. 2.13 Transmittance curves of ND filters.

2.3 Experimental Methods

2.3.1 Experimental Timing and Synchronization

Each arcing test has three stages, i.e. pre-test checking, capacitor bank charging, and arc discharging. Pre-test checking includes the air tightness of the arcing chamber, pressure of the arcing chamber, pressure of the hydraulic operating mechanism and the

close state of the system interlock switches. During the capacitor bank charging process, the charging current need to be manually controlled within a certain range using a variac. When the voltage of the capacitor bank reaches the preset value, the charging switch will automatically cut off the current. It takes approximately 10 minutes to charge the capacitor bank to 5kV. The timing of the tests and typical current, voltage, and contact displacement curves are shown in Figure 2.14.

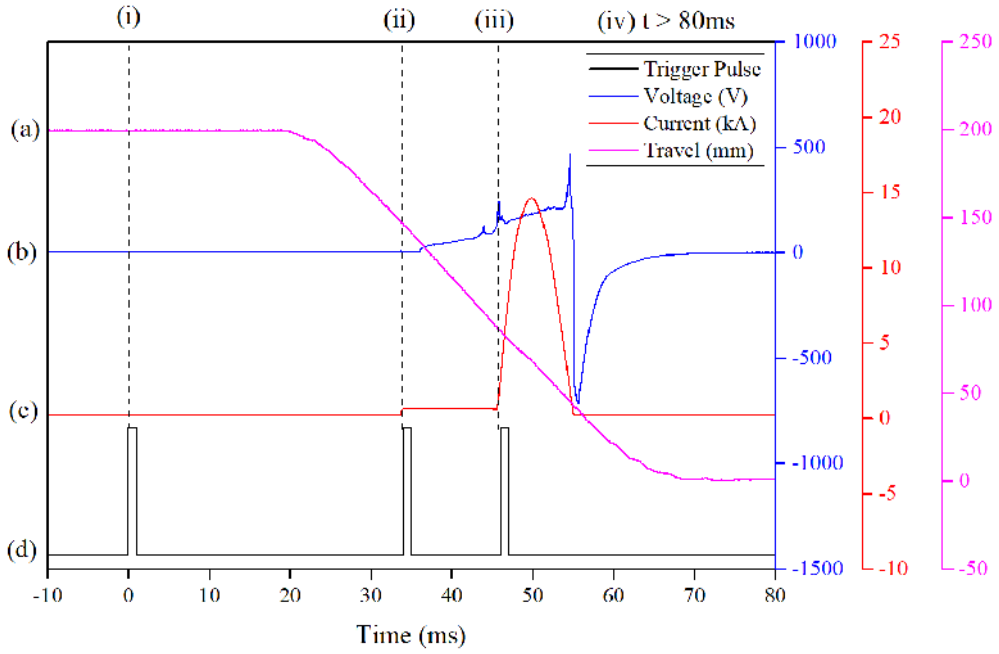

Fig. 2.14 Timing of trigger pulses and typical waveforms (a) moving contact displacement, (b) arc voltage, (c) arc current, and (d) trigger pulses - (i) trigger for hydraulic mechanism, (ii) trigger for DC current, (iii) trigger for half-cycle AC current, and (iv) trigger for dump ignitron.

The first trigger pulse is issued at the beginning of a test which triggers the hydraulic operating mechanism, the digital oscilloscope, the HSC and the HSS simultaneously. After approximately 20ms (reaction time of the operating mechanism), the hydraulic operating mechanism starts to drive the moving contact to move. Before the arcing contacts are separated, the second trigger pulse is issued and the DC ignition (Figure 2.5) is triggered, so that a DC current of several hundred amperes keeps the gap between arcing contacts conducting. After a certain period of time, the arc contact has been separated from a certain distance. The third trigger pulse is issued to trigger the forward AC ignitron (Figure 2.5). The current of the discharging circuit will quickly

transfer to the AC branch forming a positive half cycle AC current. At the first current zero crossing point, the arc will be automatically extinguished (the reverse AC ignitron is not triggered). During the arc, the capacitor bank is charged in the reverse direction, and approximately 40% of the energy is returned to the capacitor bank, so the reverse voltage overshoot can be observed at current zero point. Approximately 100ms after the arc is extinguished, the dump ignition will be triggered, the remaining charge in the capacitor bank will be discharged through the discharge resistor. At this point, a test cycle is completed.

2.3.2 Mass Loss Measurement

The mass of the plug contact tip is measured before and after each test (or several tests), and the mass loss can be calculated. The equipment for weighing the contact mass is the precision electronic scale LP1200S produced by Sartorius and its main parameters are listed in Table 2.6. After weighing, the image of the contact surface morphology was also captured for comparison.

Table 2.6 Main parameters of the precision electronic scales Sartorius Master^{pro} LP1200S.

Items	Parameters
Resolution	0.001g
Full Scale	1200g
Repeatability	$\leq \pm 0.001$g
Linearity	$\leq \pm 0.002$g
Temperature Drift	$\leq \pm 2 \times 10^{-6}$/K

2.4 Summary

This chapter describes the experimental system and methods of the arcing contacts erosion experiments of HVCB in detail, which mainly includes the following parts:

(1) This experimental arcing system was built based on a commercial 245kV/40kA SF_6 live tank self-blast HVCB. Two different kinds of structure were used in this study, i.e. the reversed-structure and the forward-structure. Cu and CuW arcing contacts were

used for different arcing tests, respectively. The experimental system is similar to the practical HVCV, and the experimental data has positive reference value for engineering applications.

(2) The optical measuring system, which is mainly composed of a HSC, a HSS and a PDD unit, was introduced. The HSC can be used for qualitative investigation of the arc behaviour and its interaction with arcing contacts. The HSS was used for capturing the spectral emission of the arc which can be analysed using chromatic methods. The PDD unit is used for capturing the relative emission intensities of the arc root for different radial directions perpendicular to the axis of the arcing contacts. Such data can be utilized in spatial domain chromatic analysis of arc root movement.

(3) The experimental methods were presented briefly. The timing of the experiments can be controlled precisely using synchronous trigger pulses. The mass losses of the arcing contact were measured using a precision electronic scale.

Chapter 3

Experimental Results

In this chapter, using the devices and methods described in Chapter 2, experiments were undertaken to investigate the behaviour of breaking arcs and the characteristics of arcing contacts erosion on different contact materials (i.e. Cu and CuW) in various quenching gases (i.e. N_2 and SF_6), with or without gas flow. Mass losses of arcing contacts under various experimental conditions are plotted against peak current. The photographs of arcing contact surface morphologies after arc erosion are shown afterwards. The high-speed photographs of the arc column and arc root are listed. The original outputs of PDD unit which is used for arc root movement detection are provided. The original time-resolved arc spectra are also plotted for various peak currents.

3.1 Experimental Contents

In total, there were four sets of tests undertaken aiming to investigate different aspects of arc/contact interaction (arcing contact erosion). The experimental conditions for all these tests are listed in Table 3.1 and unique test codes are designated to each set of tests, namely CuN2-S, CuWSF6-S, CuWSF6-D and CuWSF6-G.

To minimize confusion, throughout this thesis, each single test is designated by an unique test code as listed in Table 3.2. At each current level, tests were always undertaken successively starting from a brand new plug contact (i.e., the plug contact was always replaced before the first test).

As an example, the timing of trigger pulses and the typical waveforms (i.e. arc voltage, arc current and contact displacement) of test number c3 (Table 3.2) are shown

Table 3.1 Experimental conditions for all tests.

Parameters/Set Code	CuN2-S	CuWSF6-S	CuWSF6-D	CuWSF6-G
Plug Contact Material	Cu	CuW	CuW	CuW
Plug Contact Shape	Planar	Planar	Planar, Spherical, Trapezoid	Planar
Quenching Gas	N_2	SF_6	SF_6	SF_6
Polarity of Plug Contact	Cathode	Cathode	Cathode	Cathode
Peak Current Range	5-25kA	5-40kA	4.5-6.7kA	4.5-33.5kA
Number of Current Levels	5	8	2	3
Number of test at each current	5	5	10	5
HVCB Structure	Reversed	Forward	Forward	Forward
Nozzle Material	No Nozzle	No Nozzle	No Nozzle	PTFE
Open Speed	5m/s	5m/s	5m/s	5m/s
Trigger of DC	39ms	34ms	34ms	34ms
Trigger of AC	51ms	46ms	46ms	46ms
Duration of AC	9ms	9ms	9ms	9ms
Type of Mass Loss Value	Single	Single	Average	Average
Optical Sensor Focus	Arc Column	Arc Root	Arc Root	Arc Root
Number of Optical sensor-position	1	3	3	3
HSC Focus	Arc Column	Arc Root	Arc Root	Arc Root

in Figure 3.1. From this graph, it is shown that there is no overshoot voltage at current zero point which indicates that test c3 was an unsuccessful current breaking operation from the circuit breaker point of view.

3.2 Mass Loss of Arcing Contacts

3.2.1 Mass Loss of Cu Arcing Contacts

Figure 3.2 shows the measured mass loss of tests in set CuN2-S (Cu arcing contact in N_2 without external gas blast) subject to a half-cycle alternating current. At low currents,

Table 3.2 Designation of test codes.*

Set Code	Peak Current	1st test	2nd test	3rd test	4th test	5th test
CuN2-S	5kA	a1	a2	a3	a4	a5**
	10kA	b1	b2	b3	b4	b5**
	15kA	c1	c2	c3	c4	c5
	20kA	d1	d2	d3	d4	d5
	25kA	e1	e2	e3	e4	e5
CuWSF6-S	5kA	f1	f2	f3	f4	f5
	10kA	g1	g2	g3	g4	g5
	15kA	h1**	h2	h3	h4	h5**
	20kA	i1	i2	i3	i4	i5**
	25kA	j1	j2	j3	j4	j5
	30kA	k1	k2**	k3	k4	k5
	35kA	l1	l2	l3	l4**	l5
	40kA	m1	m2	m3	m4	m5
CuWSF6-G	4.5kA	n1	n2	n3	n4	n5
	19.0kA	o1	o2	o3	o4	o5
	33.5kA	p1	p2	p3	p4	p5

* Since the tests of set CuWSF6-D are aimed to investigate the comprehensive impact of plug contact shape on mass loss, the test number are not designated.
** Due to the reason of missing trigger, the spectra of these tests are not captured thus excluded from analysis.

less than 10kA, the mass loss of each test was only approximately 20mg. Above 15kA, the mass loss increased sharply and reached approximately 475mg at 25kA. It is clear that at each current amplitude, the mass loss values are scattered which is even more pronounced at high currents. There is no obvious correlation between the mass loss value and the sequence of the test.

3.2.2 Mass Loss of CuW Arcing Contacts

Without Gas Blast

Figure 3.3 shows the measured mass loss of tests in set CuWSF6-S (CuW arcing contact in gas SF_6 without external gas blast). The variation of the mass loss against peak current is nonlinear with an inflection point occurring between 10kA and 15kA. From 5kA to 10kA, the mass loss was only about several milligrams. Starting from 15kA (up

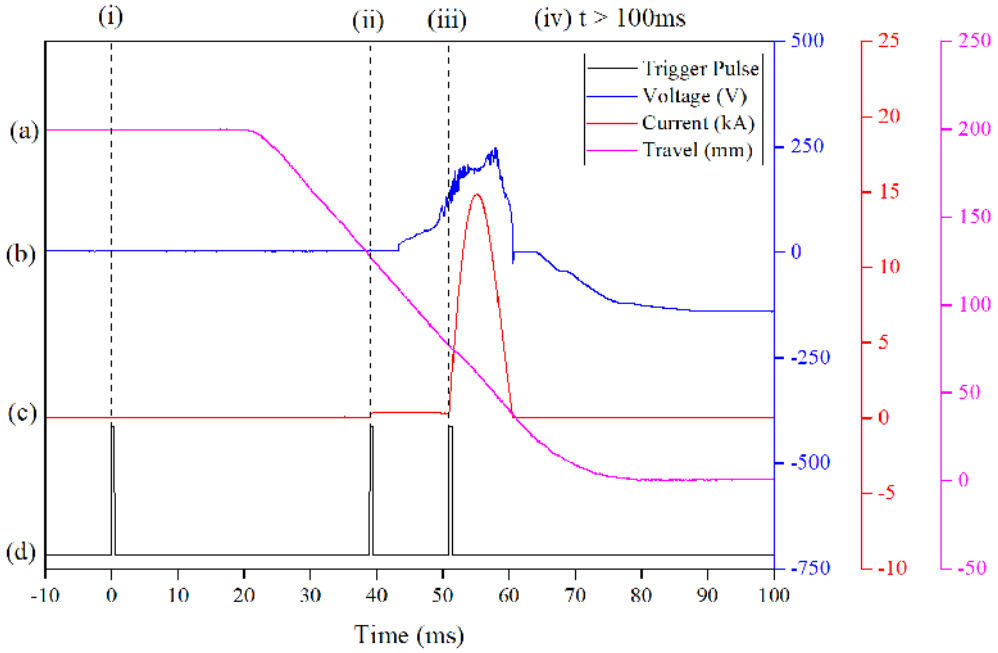

Fig. 3.1 Timing of trigger pulses and the waveforms of test number c3 (Cu contacts erosion in N_2), (a) moving contact displacement, (b) arc voltage, (c) arc current, and (d) trigger pulses - (i) trigger for hydraulic mechanism, (ii) trigger for DC current, (iii) trigger for half-cycle AC current, and (iv) trigger for dump ignitron.

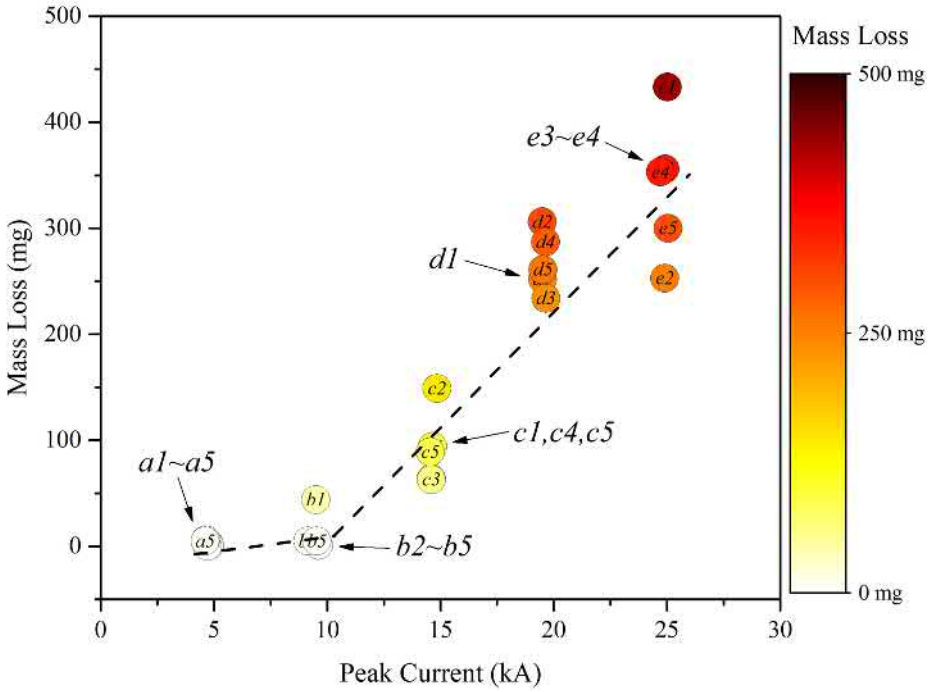

Fig. 3.2 Measured mass loss of Cu contacts erosion in N_2.

to 40kA), the mass loss increased sharply. It is also observed that, for the same current level, the mass loss generally increased with the test numbers. Especially, the mass loss of the first test on a new contact was remarkably lower than those of subsequent tests. This effect was more pronounced at high current levels (i.e., tests j1, k1, l1 and m1).

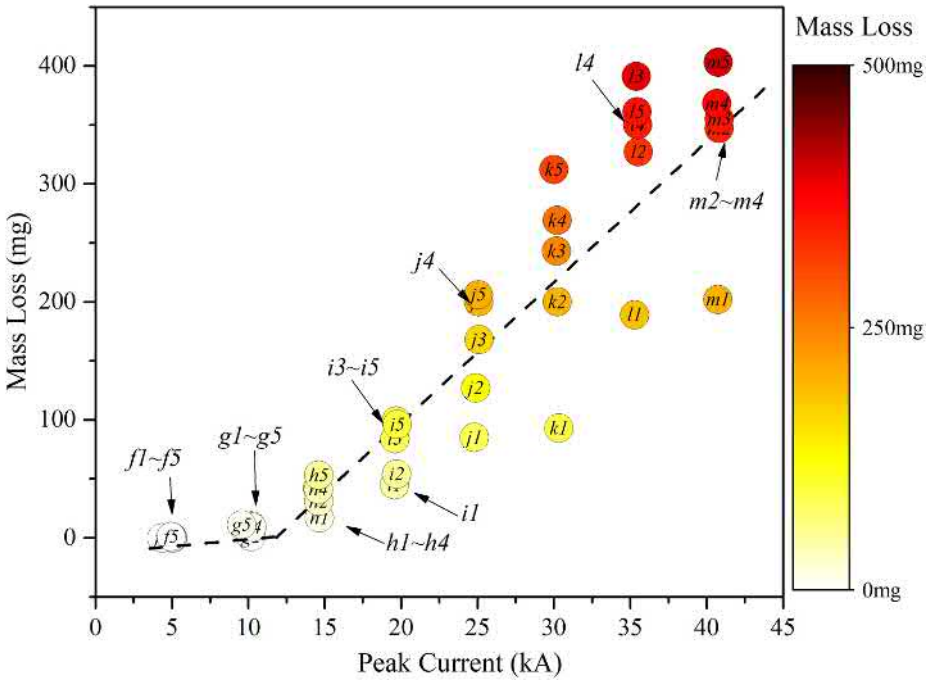

Fig. 3.3 Measured mass loss of CuW contacts erosion in SF_6.

Comparative experiments were undertaken using three different shapes of CuW arcing contacts as shown in Figure 3.4 (tests set CuWSF6-D). The diameter of the spherical and trapezoidal contacts was 18mm and 10mm, respectively.

Ten tests were performed on each type of contact with two peak currents, 4.5kA and 6.7kA. The measured average mass loss values are plotted in Figure 3.5.

The average mass loss of the trapezoidal contact was 8.0mg and 29.3mg per test at 4.5kA and 6.7kA respectively, which was the highest among all three types of contacts. The mass loss of the planar contact was 1.9mg (@4.5kA) and 5.4mg(@6.7kA) at the second place and the spherical contact was the lowest 1.1mg(@4.5kA) and 2.2mg(@6.7kA).

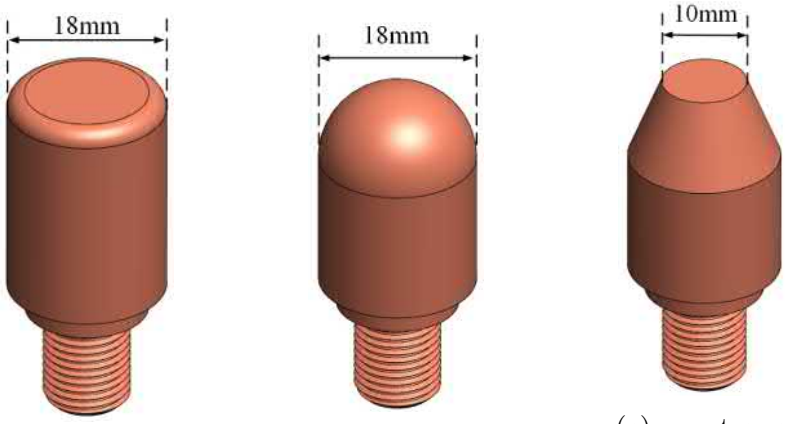

(a) Planar (b) spherical (c) trapezoidal

Fig. 3.4 Three different shapes of plug arcing contact.

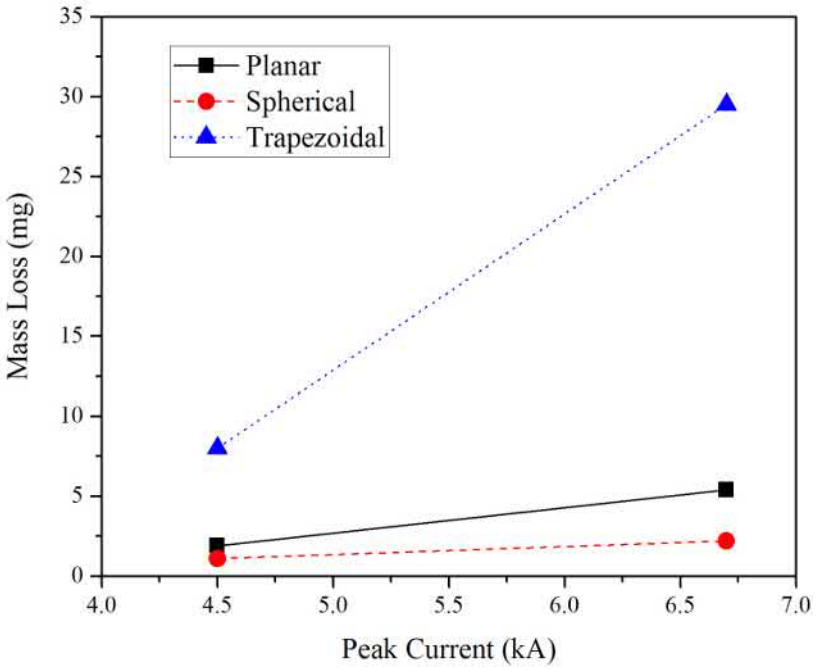

Fig. 3.5 Average mass loss of three different shapes of CuW arcing contact.

With Gas Blast

The self-generated gas flow which is used for cooling the arc plasma is critical to the process of arc extinguishing in a self-blast HVCB. With the PTFE nozzle installed (Figure 2.3(c)), an external force provided by the gas flow will be applied to the plug arcing contact surface which may cause an increase of the mass loss during

current breaking. Using the experimental configuration shown in Figure 2.3(c), the characteristics of CuW arcing contacts erosion subjected to gas blast in SF_6 (i.e., test set CuWSF6-G) were studied at three different current levels (i.e., 4.5kA, 19.0kA and 33.5kA). At each current level, five tests were undertaken successively starting from a brand new plug contact. The average mass loss values are plotted in Figure 3.6 as function of peak current. The average mass loss values are 9mg, 93mg and 640mg at 4.5kA, 19.0kA and 33.5kA, respectively.

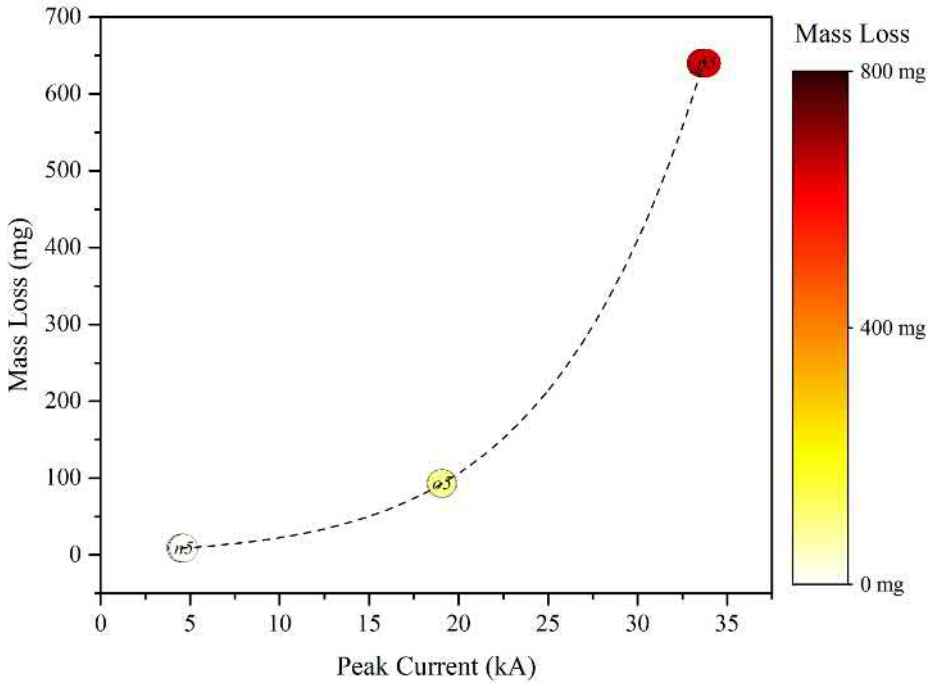

Fig. 3.6 Measured mass loss of CuW contacts erosion subject to gas blast in SF_6.

3.3 Photographs of Arcing Contacts

The surface morphologies of plug arcing contacts were affected by the arc erosion. By analysing the arcing contact surface morphologies, the arc-contact interaction and the material removal mechanisms can be preliminarily studied.

3.3.1 Photographs of Cu Arcing Contacts

Figure 3.7 shows the Cu arcing contact surface morphologies after five consecutive tests at 5kA. It was found that the edge area of the contact surface was eroded by the energy of arc roots (the red dash line area in Figure 3.7(a)) and the centre area of the arcing contact surface was survived from arc erosion in subsequent experiments (refer to the green dash line area in Figure 3.7(b) to (e)).

(a) a1 (b) a2 (c) a3 (d) a4 (e) a5

Fig. 3.7 Images of the Cu arcing contact surface after 5kA current breaking tests.

Figure 3.8 shows the images of Cu arcing contact surface at high currents. As the current increased, at 10kA (Figure 3.8(a)), the whole contact surface was eroded by the arc roots unevenly where the area in red dash line was eroded more severely than the area in green dash line. After one test at 15kA (Figure 3.8(b)), it was found that there was a copper filament on the edge of the contact surface (objects in red dash line). This can be regarded as strong evidence of liquid copper ejection during the arc. Re-solidified liquid copper was also found on the lateral surface of the contact after tests at 25kA (area in red dash line in Figure 3.8(c)).

(a) b1 (b) d1 (c) e3

Fig. 3.8 Images of the Cu contact contact surface after current breaking tests.

3.3.2 Photographs of CuW Arcing Contacts

Without Gas Blast

Figure 3.9 shows the images of CuW arcing contact surface after different numbers of tests at 40kA in SF_6. The material removal process of CuW contacts appeared to be different from that of pure copper. There were no protrusions observed on the contact surface. Since the melting and boiling temperature of copper and tungsten are different (see Table 2.1), these two types of material will not reach their boiling temperatures at the same time. The metal copper adjacent to the contact surface was vaporized first and the metal tungsten mostly remained on the contact surface (the plug contact surface showed the colour of tungsten after several tests). As shown in Figure 3.9(e), when the copper was removed, there was a crater formed at the centre of CuW contact where the melted tungsten re-solidified. Cracks were also observed on the contact surface and appeared to be more severe at specific locations (in the red dash line area) resulting in bulk removal of top layer materials.

(a) m1 (b) m2 (c) m3 (d) m4 (e) m5

Fig. 3.9 Images of the CuW arcing contact surface after 40kA current breaking tests.

With Gas Blast

Figure 3.10 shows the images of CuW arcing contact surface (and side views) after 5 arcing tests being subjected to gas blast at various currents in SF_6. At 4.5kA, the contact surface was only burned mildly by the arc root and the colour was turned into black (Figure 3.10(a)). At 19kA, the entire contact surface was formed by porous tungsten skeleton (Figure 3.10(b)) where a large crack was also observed on the edge of the contact surface (pointed out by a red arrow in Figure 3.10(d)). This offers strong evidence of the formation of layered structure of CuW contact which is subjected to arc heating. At 33.5kA, the tungsten layer no longer existed on the contact surface

(Figure 3.10(c)) and fragments of the surface layer was peeled off inside the area of red dash line. From the side view of the plug contact (Figure 3.10(e)), the patterns of stripes suggested that the melted material (including both tungsten and copper) was blown off by the generated gas flow and the streamline of the gas flow can be inferred from the pattern on the lateral surface of the contact as indicated by the greed dash arrows. It is shown that the mass loss of an arcing contact can be affected by the gas blast in a HVCB.

(a) n5 (b) o5 (c) p5 (d) o5 side view (e) p5 side view

Fig. 3.10 Images of the CuW arcing contact surface subjected to gas blast after current breaking test.

3.4 High-speed Photographs

3.4.1 Symmetry of the Arc Column

During the process of tests of set CuN2-S, using the high-speed camera configuration shown in Figure 2.6, the arc column can be observed from two perpendicular radial directions. Figure 3.11 and 3.12 show the high-speed photographs of the arc column in N_2 at 10kA and 25kA, respectively. In each figure, there are 9 photographs showing the shapes of the arc column at 1ms to 9ms after the ignition of the AC arc. In each photograph, the left half showed the arc column observed from window A (see Figure 2.6), and the right half was captured from window B (see Figure 2.6). The positions of the arcing contacts are marked in the photographs where the tulip (stationary) is at the top and plug (movable) at the bottom.

Figure 3.11 shows the high-speed photographs of an arc column at 10kA. It can be seen that during the first two milliseconds, the diameter of the arc column was small. Starting from 3ms, a strong plasma jet was formed and emanated from the plug contact surface. Figure 3.11(c) shows that the spraying direction of the plasma

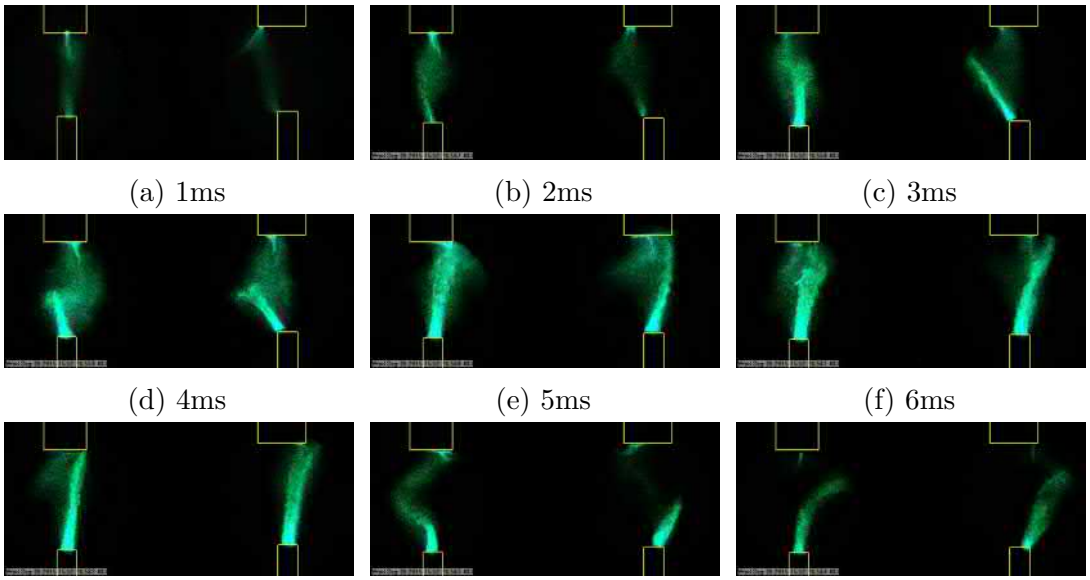

(a) 1ms (b) 2ms (c) 3ms

(d) 4ms (e) 5ms (f) 6ms

(g) 7ms (h) 8ms (i) 9ms

Fig. 3.11 High-speed photographs of arc column of test b3 (Cu contact in N_2 at 10kA, framerate 5000fps, F22 aperture, 2μs exposure time, ND64 filter and no narrow band filter).

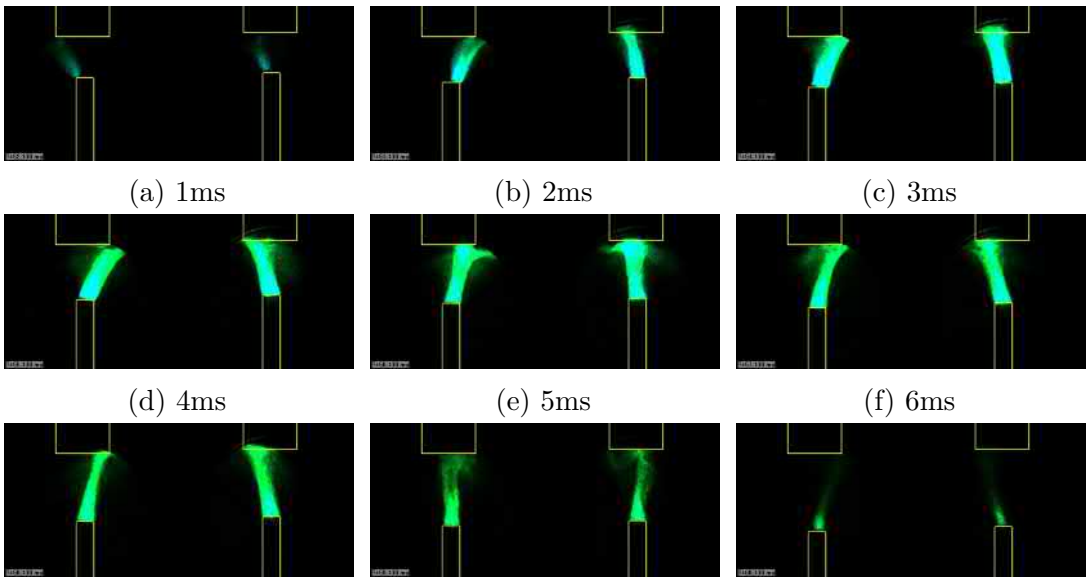

(a) 1ms (b) 2ms (c) 3ms

(d) 4ms (e) 5ms (f) 6ms

(g) 7ms (h) 8ms (i) 9ms

Fig. 3.12 High-speed photographs of arc column of test d3 (Cu contact in N_2 at 25kA, framerate 5000fps, F22 aperture, 2μs exposure time, ND64 filter and no narrow band filter).

jet deviated from the axis (the right half of the photograph). As the current was increased, the plasma jet was gradually strengthened, but its direction was unstable and always deviated from the axis. In Figure 3.11(d), plasma jets were observed from both arcing contacts which were met in the middle of the arcing channel. From 5ms to 7ms (Figure 3.11(e) to (g)), the plasma jet from the plug contact appeared to be predominating and the arc column stayed relatively close to the axis. Once the current reduced, the plasma jets began to swing in the arc channel (Figure 3.11(f)) until it was completely extinguished.

Figure 3.12 shows the high-speed photographs of arc column of another test at 25kA. It shows that the brightness of the arc column was significantly increased compared to that at 10kA. Although the arc column was at an off-axis position, the spatial position of the arc was comparatively stable and showed no significant movement during the half current cycle.

3.4.2 Distribution of the Metallic Vapour

By deploying a narrow band filter (522nm±2nm) in front of the high-speed camera lens (Figure 2.6), the spatial distribution of the copper vapour in the arcing channel can be captured.

The spatial distribution of copper vapour in the arcing channel of test set CuN2-S (Cu plug contact in N_2) at 10kA is shown in Figure 3.13. It shows that, during the first 4ms of the alternating current, there was no evidence of copper vapour in the arcing channel. At 5ms, a very thin copper vapour core appeared between the arcing contacts indicating the onset of massive vaporization of contact material. The copper vapour jet emanating from the plug contact was enlarged in the next two milliseconds and eliminated at 8ms. The optical intensity was relatively higher at the vicinity of plug contact surface than that in the middle of the arcing channel implying a relatively higher copper concentration near the plug contact.

Figure 3.14 shows the copper vapour distribution at 15kA. In general, the spread of copper vapour was enhanced from two aspects. On one hand, the onset of the intense radiation from copper vapour was advanced to 4ms which indicated that the input energy density at the plug contact surface was higher than that at 10kA. On the other hand, as the current increased, the diameter of the copper vapour core was

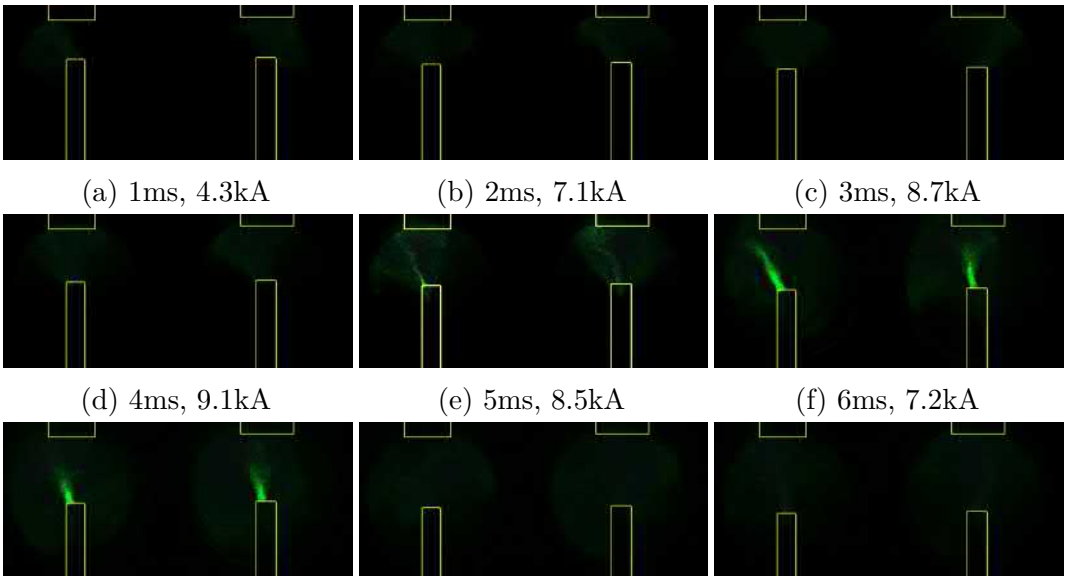

(a) 1ms, 4.3kA (b) 2ms, 7.1kA (c) 3ms, 8.7kA

(d) 4ms, 9.1kA (e) 5ms, 8.5kA (f) 6ms, 7.2kA

(g) 7ms, 5.3kA (h) 8ms, 3.2kA (i) 9ms, 1.1kA

Fig. 3.13 High-speed photographs of copper vapour distribution of test b4 (Cu contact in N_2 at 10kA, framerate 5000fps, F22 aperture, 2μs exposure time, ND64 filter and narrow band filter 522nm±2nm).

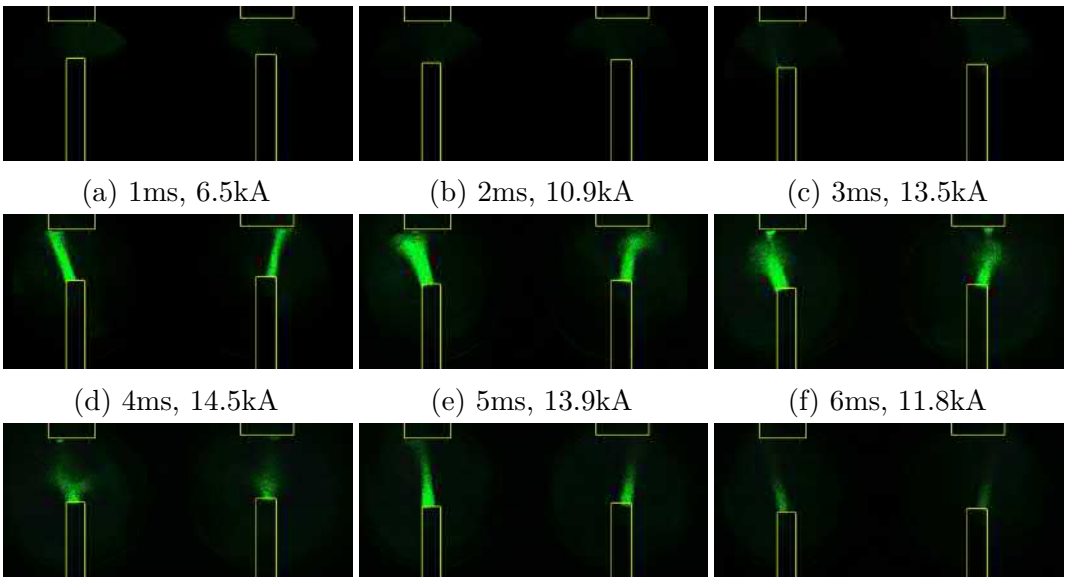

(a) 1ms, 6.5kA (b) 2ms, 10.9kA (c) 3ms, 13.5kA

(d) 4ms, 14.5kA (e) 5ms, 13.9kA (f) 6ms, 11.8kA

(g) 7ms, 8.9kA (h) 8ms, 5.4kA (i) 9ms, 1.9kA

Fig. 3.14 High-speed photographs of copper vapour distribution of test c5 (Cu contact in N_2 at 15kA, framerate 5000fps, F22 aperture, 2μs exposure time, ND64 filter and narrow band filter 522nm±2nm).

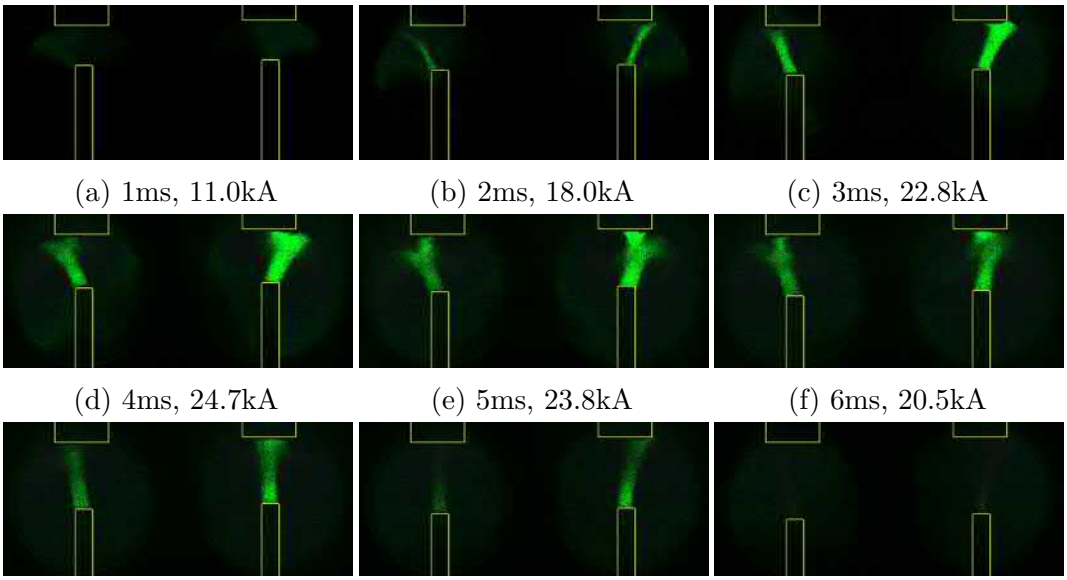

(a) 1ms, 11.0kA (b) 2ms, 18.0kA (c) 3ms, 22.8kA

(d) 4ms, 24.7kA (e) 5ms, 23.8kA (f) 6ms, 20.5kA

(g) 7ms, 15.8kA (h) 8ms, 9.9kA (i) 9ms, 3.7kA

Fig. 3.15 High-speed photographs of copper vapour distribution of test e4 (Cu contact in N_2 at 25kA, framerate 5000fps, F22 aperture, 2μs exposure time, ND64 filter and narrow band filter 522nm±2nm).

enlarged as well. At 6ms, there was a copper jet emanating from the tulip contact. The encounter of the copper jets from both arcing contacts in the arcing channel formed a "vapour disk" and perturbed the original flow of copper vapour resulting in an irregular distribution of vapour. A similar phenomenon was observed at 25kA (Figure 3.15). In addition, the arc attachment point on the tulip contact was always on its edge thus the direction of the copper vapour jet was not vertical. This coincided with the phenomena observed without using the narrow band filter in Section 3.4.1.

Figure 3.15 shows the spatial distribution of the copper vapour at 25kA. The onset of intense vaporisation of contact material was further advanced to 2ms and the diameter of the copper vapour was also further increased. In particular, the copper vapour emanating from the tulip contact surface appeared to be more intensive. In this case, the light emission from the arcing channel was the superposition effect of both arcing jets.

3.4.3 Mobility of the Arc Root

By using the high-speed camera configuration as shown in Figure 2.7, the detailed arc root movement on the contact surface can be captured. Figure 3.16 to 3.23 show the high-speed photographs of the arc root movement on CuW contact surfaces in SF_6 at eight different currents from 5kA to 40kA.

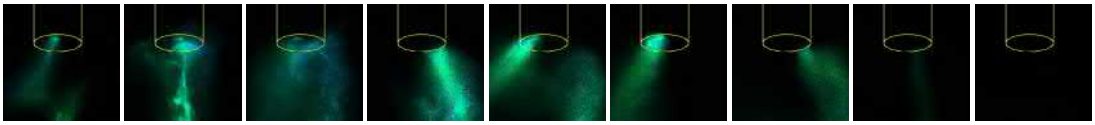

(a) 1ms (b) 2ms (c) 3ms (d) 4ms (e) 5ms (f) 6ms (g) 7ms (h) 8ms (i) 9ms

Fig. 3.16 Movement of arc root of test f3 (CuW contact in SF_6 at 5kA, framerate 10000fps, F22 aperture, 2μs exposure time, ND64 filter, no narrow band filter).

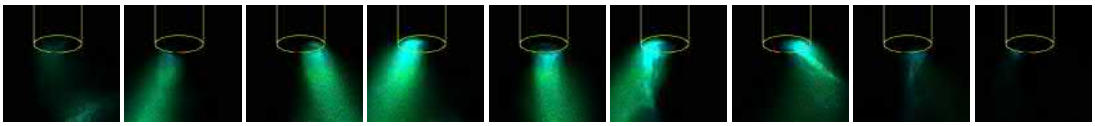

(a) 1ms (b) 2ms (c) 3ms (d) 4ms (e) 5ms (f) 6ms (g) 7ms (h) 8ms (i) 9ms

Fig. 3.17 Movement of arc root of test g3 (CuW contact in SF_6 at 10kA, framerate 10000fps, F22 aperture, 2μs exposure time, ND64 filter, no narrow band filter.)

(a) 1ms (b) 2ms (c) 3ms (d) 4ms (e) 5ms (f) 6ms (g) 7ms (h) 8ms (i) 9ms

Fig. 3.18 Movement of arc root of test h3 (CuW contact in SF_6 at 15kA, framerate 10000fps, F22 aperture, 2μs exposure time, ND64 filter, no narrow band filter.)

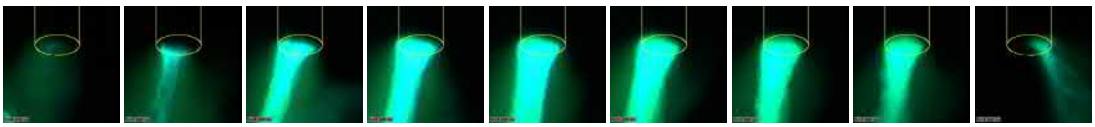

(a) 1ms (b) 2ms (c) 3ms (d) 4ms (e) 5ms (f) 6ms (g) 7ms (h) 8ms (i) 9ms

Fig. 3.19 Movement of arc root of test i2 (CuW contact in SF_6 at 20kA, framerate 10000fps, F22 aperture, 2μs exposure time, ND64 filter, no narrow band filter.)

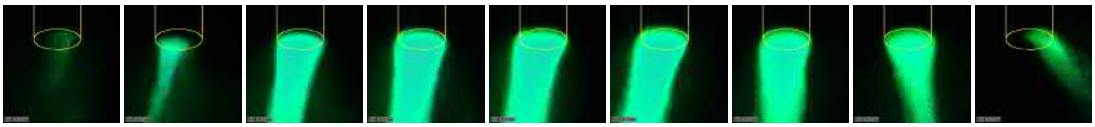

(a) 1ms (b) 2ms (c) 3ms (d) 4ms (e) 5ms (f) 6ms (g) 7ms (h) 8ms (i) 9ms

Fig. 3.20 Movement of arc root of test j3 (CuW contact in SF_6 at 25kA, framerate 10000fps, F22 aperture, 2μs exposure time, ND64 filter, no narrow band filter.)

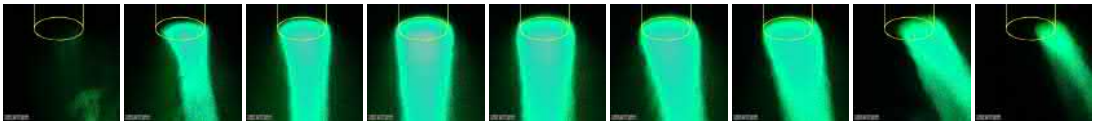

(a) 1ms (b) 2ms (c) 3ms (d) 4ms (e) 5ms (f) 6ms (g) 7ms (h) 8ms (i) 9ms

Fig. 3.21 Movement of arc root of test k3 (CuW contact in SF_6 at 30kA, framerate 10000fps, F22 aperture, 2μs exposure time, ND64 filter, no narrow band filter.)

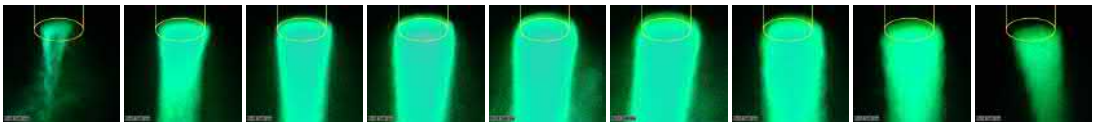

(a) 1ms (b) 2ms (c) 3ms (d) 4ms (e) 5ms (f) 6ms (g) 7ms (h) 8ms (i) 9ms

Fig. 3.22 Movement of arc root of test l3 (CuW contact in SF_6 at 35kA, framerate 10000fps, F22 aperture, 2μs exposure time, ND64 filter, no narrow band filter.)

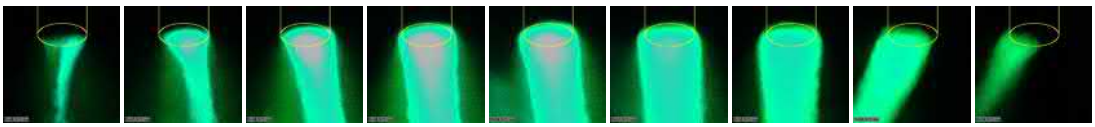

(a) 1ms (b) 2ms (c) 3ms (d) 4ms (e) 5ms (f) 6ms (g) 7ms (h) 8ms (i) 9ms

Fig. 3.23 Movement of arc root of test m3 (CuW contact in SF_6 at 40kA, framerate 10000fps, F22 aperture, 2μs exposure time, ND64 filter, no narrow band filter.)

Figures 3.16 and 3.17 show the arc root movement on CuW contact surface at 5kA and 10kA, respectively. These show that the arc root is more likely to be tangential to the edge of the contact surface rather than located at the centre. For both 5kA and 10kA tests, the diameters of the arc roots were much smaller than the diameter of plug contact. The arc roots were observed moving on the contact surface continuously.

Figures 3.18 and 3.19 show the high-speed photographs of an arc root at 15kA and 20kA, respectively. As the current increased, the diameters of the arc roots were increased, therefore, the mobility was decreased. At 15kA, it was also found the arc

root were always tangential to the edge of the contact surface (Figure 3.18). At 20kA, a similar phenomenon was observed (Figure 3.19), and the arc root occupied almost the entire contact surface during the peak current time approximately from 5ms to 7ms.

Figures 3.20 to 3.23 show the high-speed photographs of an arc root at 25kA, 30kA, 35kA and 40kA, respectively. At these current levels, the arc roots occupied the entire surface of the plug contact for most of the arcing time and even expanded to the lateral surface of the contact (Figure 3.22 and 3.23), thus there was no spare space for the free movement of the arc root. The brightness of the arc column region adjacent to the contact surface was intense which might be caused by the severe vaporisation of contact material.

High-speed photographs of the arc root have also been obtained for two other contact shapes namely spherical and trapezoidal (Figure 3.4) in addition to the planar shape as shown on Figure 3.24 to 3.25, respectively. The movement of the arc root shows different patterns on these two types of plug contacts. The arc root moves rapidly without fixing at any specific locations on the spherical contact. On contract, the movement of the arc root on the trapezoidal contact surface appeared to be less pronounced.

(a) 1ms (b) 2ms (c) 3ms (d) 4ms (e) 5ms (f) 6ms (g) 7ms (h) 8ms (i) 9ms

Fig. 3.24 Movement of arc root on spherical CuW contact in SF_6 at 4.5kA. (Framerate 10000fps, F22 aperture, 2μs exposure time, ND4 filter, no narrow band filter.)

(a) 1ms (b) 2ms (c) 3ms (d) 4ms (e) 5ms (f) 6ms (g) 7ms (h) 8ms (i) 9ms

Fig. 3.25 Movement of arc root on trapozoidal CuW contact in SF_6 at 4.5kA. (Framerate 10000fps, F22 aperture, 2μs exposure time, ND4 filter, no narrow band filter.)

3.4.4 Metallic Droplet Ejection of CuW Contact

Figure 3.26 shows photographs of metallic droplet ejection from a CuW contact surface 0.5ms after current zero subjected to different numbers of operations at 35kA. After the first current breaking operation, there was no obvious molten droplet to be seen in the arcing channel (Figure 3.26(a)) indicating that the droplet ejection phenomenon was very less remarkable on new contacts. After the fifth test (Figure 3.26(b)), small droplets ejected from the contact surface can be clearly observed. After the tenth test, not only the size, but also the spread of the molten droplets became significant (Figure 3.26(c)).

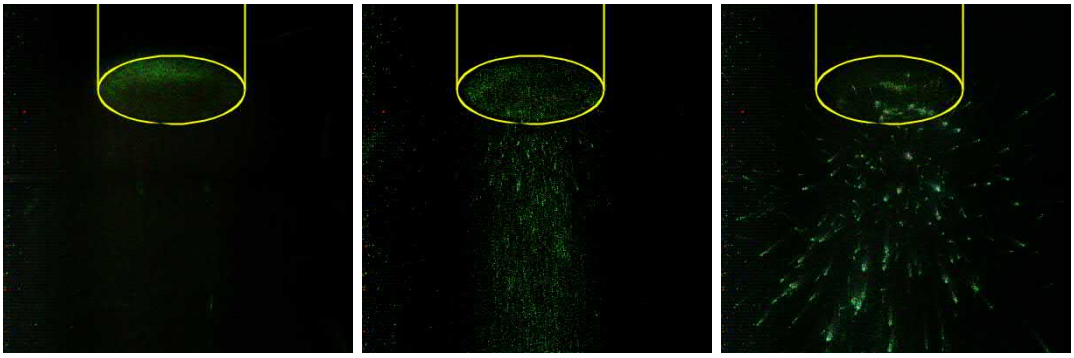

(a) after 1st test (b) after 5th test (c) after 10th test

Fig. 3.26 Photographs of metallic droplet ejection from CuW contact 0.5ms after current zero at 35kA.

3.5 Optical Fibre Movement Detection

By using the arrangement of optical fibre sensors shown in Figure 2.9 and the PDD unit, the arc light emission at the cathode region can be measured from three different radial directions. When the arc root moves on the arcing contact surface, the distance between the centre of the arc root and the sensor varies, which will result in the changing of the output voltages of the PDD unit.

A typical result is given on Figure 3.27 which shows the outputs from the three sensors (designated as I_1, I_2, I_3) as a function of time for different peak currents (5, 15, 40kA). Figure 3.27(a) corresponds to a 5kA current. It shows the I_3 output to have two main peaks at 47 and 51ms, the I_1 output to also have two main peaks but

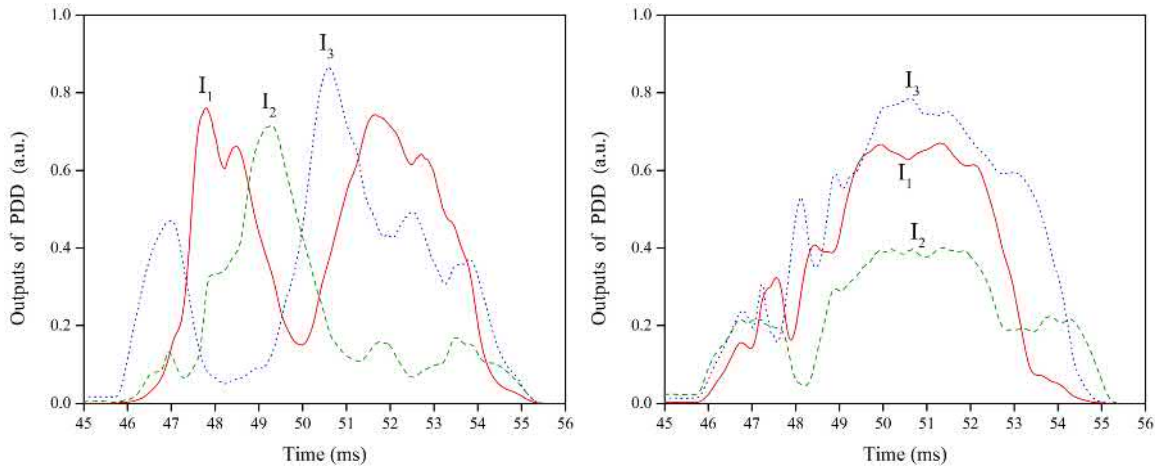

(a) 5kA

(b) 15kA

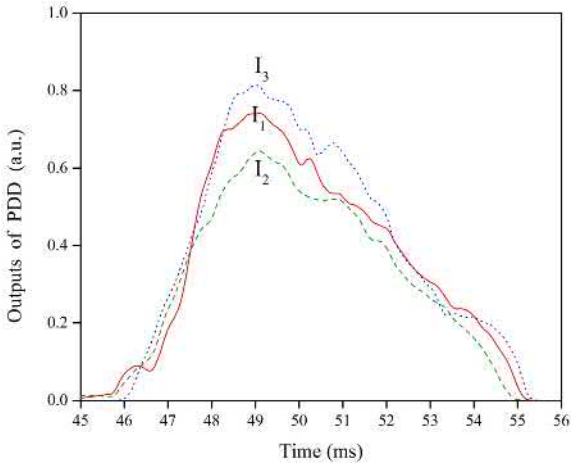

(c) 40kA

Fig. 3.27 Outputs of PDD units for arc root movement on CuW contact surface in SF_6 at various currents. (I_1, I_2 and I_3 represent the outputs of fibre optic sensor at angular positions 0°, 120° and 360°, respectively)

at 48 and 53kA whilst the I_2 output has only one main peak at 49.5ms. Each peak output correspond to the arc root being closest to that detection channel so that the displacement of the I_1, I_2, I_3 peaks with respect to each other represents the rotation of the arc. For a current of 15kA (Figure 3.27(b) the main feature is a single broad peak for each output (I_1, I_2, I_3) occurring in the time range 49 – 54ms. This indicates a broader arc with less movement. Also $I_{2,peak} < I_{1,peak} < I_{3,peak}$ suggesting that the broad arc is furthest from the detector of channel 2 and nearest to the detector of channel 3. For a current of 40kA, the three outputs I_1, I_2, I_3 overlap and have a single broad peak at about 49ms. The peaks are asymmetric initially increasing quite rapidly

and decaying more gradually. This is indicative of the arc cross-section growing rapidly but decaying more slowly.

3.6 Time-resolved Spectra

3.6.1 Time-resolve Spectra of Cu Contact

The time-resolved spectra of the arc light emission of test set CuN2-S (Cu contact in N_2) at various peak currents are shown in Figure 3.28. As the reversed-structure of HVCB was used, the optical fibre sensor used for capturing the arc spectra was mounted at the centre of one observing window (Figure 2.6). Therefore, the light emission from the entire arc column could be captured. There were approximately 10 spectra from 51ms to 61ms during the positive half cycle of AC current. The amplitudes of spectra of different tests are not to scale.

At low currents, 5kA, the arc spectra were mainly composed of line emission (Figure 3.28(a)). The spectra lines from nitrogen atom/ion were predominant. On contrast, the emission from copper atom/ion was less significant. As the current increased, at current levels higher than 15kA, the continuum spectrum started to be significant (Figure 3.28(c) and (e)). Especially in the wavelength range close to near infrared (NIR) band ($\geq$610nm), the relative spectral intensity was much higher than that in green band (410-480nm).

Figure 3.28(b), (d) and (f) show the captured spectra at peak current time ($\sim$56ms). At 5kA, the spectral emission from the blue band ($\leq$495nm) account for a large part of the overall optical energy. The line-spectrum of copper atoms at 510.6nm, 515.3nm and 521.8nm were weak compared with the emission from nitrogen. At 15kA, the spectral lines of copper atoms became significant before the emission from the orange/red band ($\geq$590nm) became the dominating component at 25kA.

3.6.2 Time-resolved Spectra of CuW Contact

Without Nozzle

The time-resolved spectra of the arc emission light of test set CuWSF6-S (CuW contact in SF_6) at various peak currents are shown in Figure 3.29. Since the forward-structure

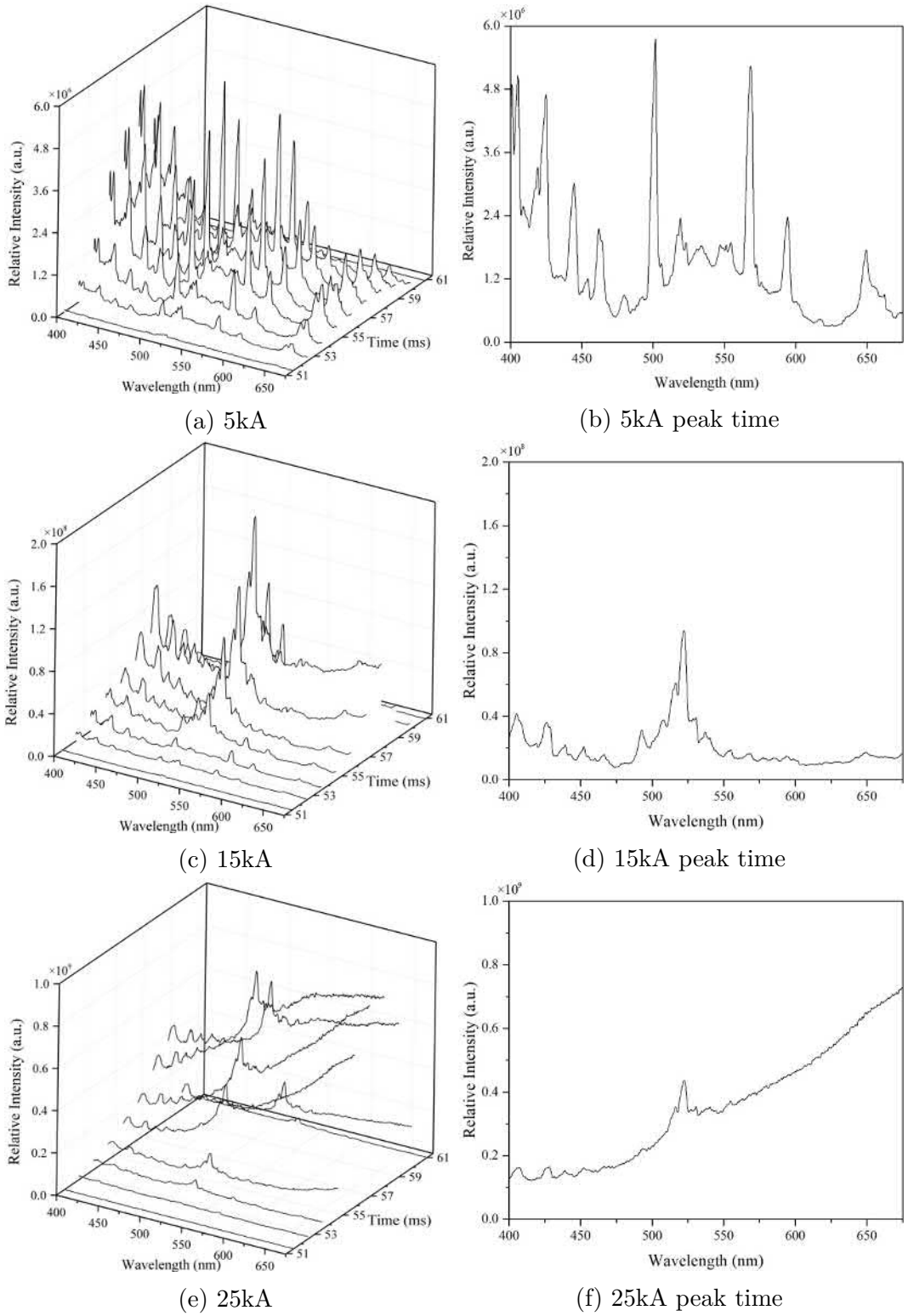

(a) 5kA (b) 5kA peak time

(c) 15kA (d) 15kA peak time

(e) 25kA (f) 25kA peak time

Fig. 3.28 Arc spectra captured for Cu contact arc in N_2 at various currents.

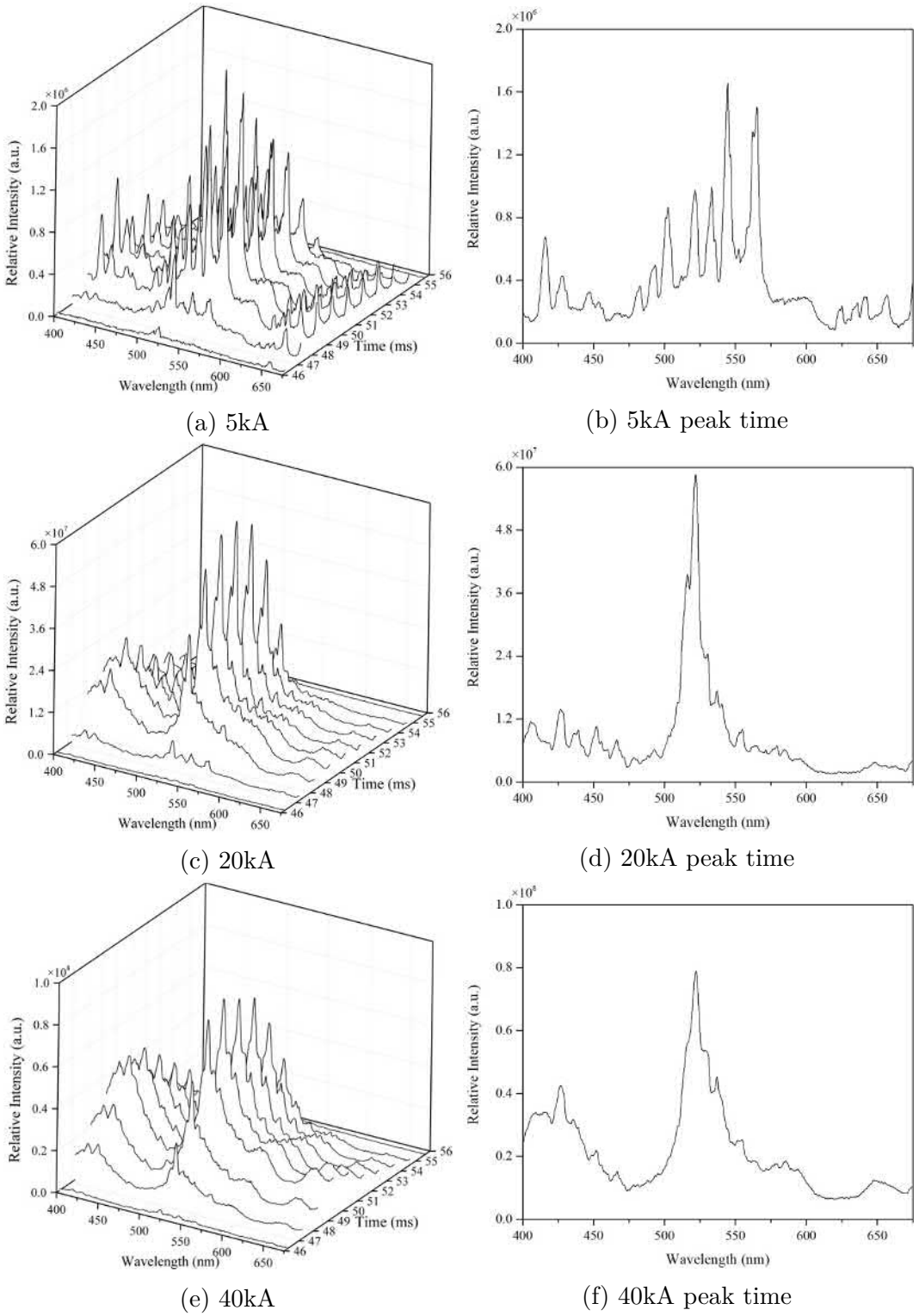

(a) 5kA (b) 5kA peak time

(c) 20kA (d) 20kA peak time

(e) 40kA (f) 40kA peak time

Fig. 3.29 Arc spectra captured for CuW contact in SF_6 at various currents.

of HVCB was used (Figure 2.2(b)), the apertures of the optical fibre sensors were restricted to the arc root region adjacent to the plug contact surface. There were approximately 10 spectra from 46ms to 56ms during the positive half cycle of alternating current. The amplitudes of spectra of different tests are not to scale.

At 5kA, the arc spectra were mainly composed of line emission (Figure 3.29(a)). Since the apertures of the optical fibre sensors were restricted to the contact surface region, the spectral emission from copper atom lines (i.e. 510.6nm, 515.3nm and 521.8nm) were always predominant. It can be seen from Figure 3.29(c) and (e) that the profiles of arc spectra in wavelength domain were similar to each other, however their time variations appeared to be diverse. Figure 3.29(b), (d) and (f) show the arc spectra captured at peak current time. It is clear that the profiles of spectrum at higher current levels (20kA and 40kA) were similar.

With PTFE Nozzle

The time-resolved spectra of the arc emission light from CuW contact in SF_6 subject to gas flow at various current amplitudes are shown in Figure 3.30. Since a PTFE nozzle was used, the captured spectra were characterized not only by the arc-cathode interaction, but also by the arc-nozzle interaction. There were approximately 10 spectra from 46ms to 56ms during the positive half cycle of alternating current. The amplitudes of spectra of different tests are not to scale.

At low current, the intensities of the arc light penetrating the nozzle wall were pretty low and some of the spectral lines were submerged in the background noise of readout which cannot be distinguished clearly (Figure 3.30(a)). As the current increased, at 19kA and 33.5kA, the line spectrum of copper became predominant. At the initial stage of the arc (approximately from 46ms to 50ms), the relative intensities of the spectra were low. A clear view of the spectrum at 53.6ms of each current level is shown in Figure 3.30 (b), (d) and (e).

3.7 Summary

This chapter presented all the experiments undertaken in this study along with the main results obtained. The mass loss of Cu and CuW arcing contacts in N_2 and SF_6, with

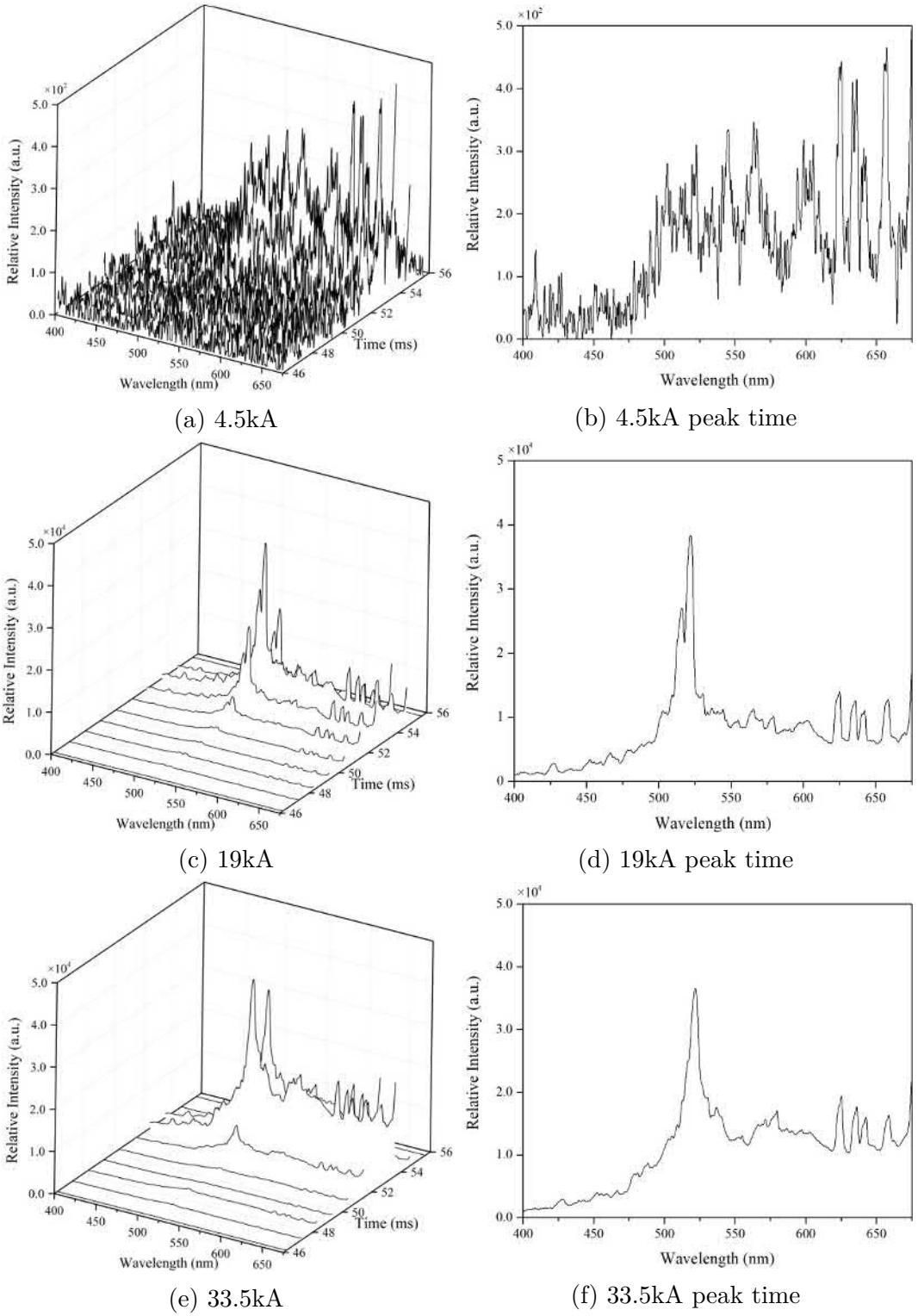

(a) 4.5kA (b) 4.5kA peak time

(c) 19kA (d) 19kA peak time

(e) 33.5kA (f) 33.5kA peak time

Fig. 3.30 Arc spectra capture for CuW contact in SF_6 with a PTFE nozzle at various currents.

or without gas flow, were measured at various current amplitudes. The photographs of arcing contact surface morphologies after arc erosion are shown afterwards. The high-speed photographs of the arc column and arc root are listed. The original outputs of PDD unit which is used for arc root movement detection are provided. The original time-resolved arc spectra are also plotted for various peak currents. Detailed analysis and discussion of these experimental results will be presented in the following chapters.

Chapter 4

Study of Macroscopic Arc Behaviour in HVCB and Its Effect on Arcing Contacts Erosion

In this chapter, the macroscopic arc behaviour in HVCB and the correlation between arc root movement and arcing contacts erosion are considered using the range of experimental results described in Chapter 3. By using the high-speed photographies, the symmetry of the arc column, the mobility of the arc root and the metal droplets ejection from the arcing contact surface were analysed. The quantitative relationship between the movement of the arc root and the mass loss of arcing contact was analysed by using the spatial domain chromatic method.

4.1 Macroscopic Arc Behaviour in an HVCB

4.1.1 Arc Column

Symmetry of the Arc Column

For the modelling of current breaking process and contacts erosion in an HVCB, a 2D axial symmetrical geometry is always used[21, 38, 78]. The simplification of the arc geometry can largely boost the speed of scientific computation. However, while dealing with the task of monitoring the erosion of arcing contact and providing an accurate

mass loss value, the symmetry of the arc column will play an important role and need to be carefully verified. Without the validity of axial symmetry, the reverse Abel transform can not be applied, therefore the local temperature and particle densities of the arc plasma can be hardly derived within an acceptable range of error[62].

The shape of arc column is the results of competition of arc jets from both arcing contacts. At low current, as observed from Figure 3.11, strong arc jet was emanating from the tulip contact during the high current phase and met the arc jet from the plug contact in the middle of arcing channel leading to the instability and perturbation of the arc column. At high current (Figure 3.12), due to the difference of contact material, the arc jet emanating from the plug contact was remarkably stronger than that from tulip contact. Therefore, the shape of the arc column was determined by the shape of the arc jet of plug contact. As the conducting position of the tulip contact was on one of its fingers, the arc column was always deviate from the axis of contacts. Taken together, the shape of the arc column was not cylindrically symmetrical which was especially so at low currents. However, the widths of the arc root were approximately the same from both observing directions at all times, implying that the arc root may be circular.

From the perspective of modelling, the assumption of axisymmetry is generally accepted at high currents but needs to be adjusted at low currents. It also can be preliminarily summarised that the interaction between the arc and arcing contacts are essentially not the same at different current levels.

From the perspective of on-line monitoring, the selection of optical sensors' position is one of the essential tasks. A global picture of the arc column provides the information of arc jets emanating from arcing contacts which cannot be treated separately and the perturbation of arc column may introduce higher uncertainty of measurements. Therefore, the utilization of optical sensors focusing on the cathode (plug contact) region may be helpful to obtain reliable data.

Spatial Distribution of Metallic Vapour

The presence of metallic vapour in the arc column will significantly alter the properties of the arc plasma, thus the current breaking capability and dielectric recovery speed of the HVCB[79]. As the metallic vapour is basically generated from the arcing contacts,

the spatial distribution (and its time variation) of metallic vapour can offer much information regarding the erosion of arcing contacts.

The distribution of metallic vapour in the arcing channel was found closely related to the peak current magnitudes. At high currents, the diameter of the copper vapour jet was larger than that at low currents. However, there was no strong relation between the metallic vapour concentration and the instantaneous current. For instance, in Figure 3.15, the instantaneous current at 2ms was 18.0kA, the diameter of the copper vapour jet was smaller than that in Figure 3.14 at 5ms (instantaneous current was 13.9kA). Therefore, it is unreliable to estimate the severity of evaporation of arcing contact material using instantaneous spectrum. Instead, the time-resolved spectra are of greater importance containing the information of arcing contacts erosion.

From the perspective of on-line monitoring, the measurement of total mass loss of the arcing contact during a current breaking process, if only evaporation is considered, requires the space and time integration of the metallic vapour which is a extreme complicated task. Therefore, the exploration of the correlation between the optical emission from the arc and the mass loss of arcing contacts becomes a natural choice.

4.1.2 Mobility of the Arc Root

The movement of the arc roots on CuW contact surface at various currents are shown in Figures 3.16 to 3.23.

From the high-speed photographs, it is observed that the arc root was more likely to be tangential to the edge of the contact surface rather than located at the centre. This is because, on one hand, the last contact point of the arcing contacts before separation was on the edge of the plug contact (see Figure 2.1) and the arc was always ignited on the edge of the contact surface; on the other hand, the electric field strength on the edge was higher[80] than the centre area which results in a higher possibility of electric breakdown and sustaining the conductivity.

The interaction between the arc root and the arcing contact has various patterns at different peak current because the mobility of the arc root is decreased as the peak current increased. At low current, e.g. 5kA and 10kA, the diameters of the arc roots were much smaller than the diameter of plug contact and there was large space for the free movement of arc root. Due to the rapid movement of the arc root, the heating

effect to the arcing contact at fixed locations was significantly reduced. Therefore, at low currents, the mobility of the arc root plays a significant role of the mass loss of plug arcing contact. At high currents, since the diameter of the arc root was comparable to the diameter of the plug contact, there was no free space for the movement of the arc root. Without considering the current density distribution, the entire contact surface was subjected to continuous heating from the arc root.

The movement of the arc roots on the spherical and trapezoidal CuW contact surface are shown in Figures 3.24 and 3.25, respectively. Through comparison of the arc root movement on different contact surfaces, it was found that the arc roots have the lowest mobility on the trapezoidal contact, followed by the planar contact, and the highest on the spherical contact, which can be primarily ascribed to the difference of the contact top surface area (spherical contact is approximately twice of the planar contact and 6.5 times of the trapezoidal contact). Considering the mass loss values shown in Figure 3.5, it is inferred that, at the same current level, the mass loss of the arcing contact is inversely proportional to the mobility of the arc roots qualitatively. In other words, the higher the mobility of the arc root, the lower the mass loss of the contact.

4.1.3 Metal Droplet Ejection from Arcing Contact Surface

Vaporisation and droplet ejection are the two main material removal mechanisms causing mass loss of arcing contact. However, the latter mechanism has always been overlooked due to the lack of experimental data. Since the melting and boiling temperature of copper and tungsten are different, a layered structure is always formed on the CuW arcing contact during the process of erosion (Figure 1.3) leading to the ejection of molten material a extreme complicated process. So far, there is no reported contact erosion model considering the molten droplet ejection of CuW material, however this phenomenon can be studied qualitatively via high-speed photographs.

From the high-speed photographs shown in Figure 3.26, it is found that the ejection of the metallic droplets becomes increasingly remarkable as the number of breaking operation increased. Therefore, it can be deduced that, as the test number increased, the ratio of mass loss due to droplet ejection also increased and it is very likely due to the change of the arcing contact surface morphologies. At present, the ratio of mass loss

caused by vaporisation and droplet ejection can be hardly determined experimentally. However, Kolacinski[81] suggested that the majority of the ejected molten droplets will be heated up in the arc column and be vaporised shortly. This will result in the increasing of the metal vapour concentration in the arc column and spectral emission intensities of metal atom lines. According to this, from the perspective of on-line monitoring, the effect of droplet ejection can be reflected implicitly via the spectral measurement of the arc to a certain degree.

4.2 Chromatic Monitoring of Arc Root Movement

In HVCB, due to the symmetrical structure of the device, it is generally assumed that the arc is located on the axis of contacts and has a symmetrical distribution. From the discussions in the previous section, it has been found the arc column is not cylindrically symmetrical in space and the arc root position changes continuously during the breaking process. The measurement of the arc root movement in an enclosed arcing chamber is a burdensome task. However, the techniques developed by Yokomizu[82], allows the instantaneous positions of the arc root on the plug contact surface to be measured based on the utilization of three photodiode detectors and the use of spatial domain chromatic processing algorithms. The quantitative relationship between the arc root mobility and the mass loss of arcing contact is discussed in this way.

4.2.1 Treatment of PDD Unit Outputs

The outputs of photodiode detectors are inversely proportional to the square of the distance between the arc root centre and each fibre optic sensor. To simplify the calculation of the photodiode detector outputs, the following assumptions were made:
(1) the arc root is treated as a zero-diameter filament located at a position with polar coordinates (r, θ);
(2) the optical radiation leaves the arc uniformly in all directions;
(3) the optical radiation of the arc is absorbed indiscriminately by the transmitting medium between the arc and each detector;
(4) the angular response of the fibre optic sensor is treated as a constant within its small optical aperture; (5) the photodiode detectors have the same characteristics.

The output voltage of the three photodiode detectors can be designated as I_i (i = 1, 2, 3) which can be written as[82]:

$$I_i = kQ_i(r, \theta) \tag{4.1}$$

where k is a parameter which is independent of the arc root position and $Q_i(r, \theta)$ is expressed in terms of geometrical variables dependent on the arc root centre coordinates (r, θ). They can be written as

$$k = \Delta z L_F \int \epsilon(\lambda)\kappa(\lambda)A_F(\lambda)S(\lambda)d\lambda \tag{4.2}$$

$$Q_i(r, \theta) = \frac{1}{r^2 + r_i^2 - 2rr_i cos(\theta - \theta_i)}. \tag{4.3}$$

In Equation (4.2), Δz and L_F designate the axial length of the arc being monitored and the length of the optical fibre, respectively. The terms in the integral formula $\epsilon(\lambda)$, $\kappa(\lambda)$, $A_F(\lambda)$ and $S(\lambda)$ represent the emission coefficient of the arc, absorption coefficient of the ambient gas, attenuation of the optical fibre and optical sensitivity as function of wavelength λ. In Equation (4.3), r_i and θ_i indicate the polar coordinates of the three fibre optic sensors.

4.2.2 Chromatic Processing

The coordinates of the arc root central position can be derived via careful calibration of the optical measuring system using Equations (4.1) to (4.3). However, a sophisticated optical measuring system may not be able to withstand the harsh environments of an HVCB in service. The application of absolute intensity measurement seem not to be the best option. Moreover, with regard to a condition monitoring system, the pattern of arc root movement is more of interest rather than its precise location. According to this, two concepts of dominant angle (θ_d) and a nominal radius (r_n) are introduced to define the relative position of the arc root centre on the contact surface based on the

HLS transformation (Equation (A.4) and (A.8)) which are given by

$$\begin{aligned} \theta_d &= 240 - 120\frac{G_i}{G_i + B_i} \quad if \quad R_i = 0 \\ &= 360 - 120\frac{B_i}{B_i + R_i} \quad if \quad G_i = 0 \\ &= 120 - 120\frac{R_i}{R_i + G_i} \quad if \quad B_i = 0 \end{aligned} \tag{4.4}$$

$$r_n = \frac{max(I_1, I_2, I_3) - min(I_1, I_2, I_3)}{max(I_1, I_2, I_3) + min(I_1, I_2, I_3)} \tag{4.5}$$

where

$$\begin{aligned} R_i &= I_1 - min(I_1, I_2, I_3) \\ G_i &= I_2 - min(I_1, I_2, I_3) \\ B_i &= I_3 - min(I_1, I_2, I_3) \end{aligned} \tag{4.6}$$

$Max(I_1, I_2, I_3)$ and $min(I_1, I_2, I_3)$ represent the highest and lowest values of (I_1, I_2, I_3), respectively.

The utilization of the chromatic technique for position monitoring in a 2D plane was based on the circular deployment of chromatic processors (Figure 4.1(a)) which has a significant difference from the linear deployment (Figure 4.1(b)). The circular deployment of the processors with the delta configurations leads to the responsivity of each processor overlapping with the responsivity of both the other processors, unlike the linear processor deployment when only one processor responsivity overlapping with two others. As a result H values in the range 240°–360° each represents a real location in physical space (unlike the linear parameter case, e.g., frequency, where it can only represent the superposition of two or more signals).

Figure 4.2 shows the relative positions of seven selected points (P1 - P7) on a plug arcing contact surface in order to validate the above technique for arc root movement monitoring.

The values of polar coordinates, normalized outputs of photodiode detectors, calculated dominant angle (θ_d) and nominal radius (r_n) of P1 - P7 are listed in Table 4.1. In Figure 4.3, it is clearly shown that the physical positions of P1 - P7 are unambiguously represented by the calculated dominant angle and nominal radius on a 2D polar diagram. The relative uncertainties in r and θ coordinates were estimated to

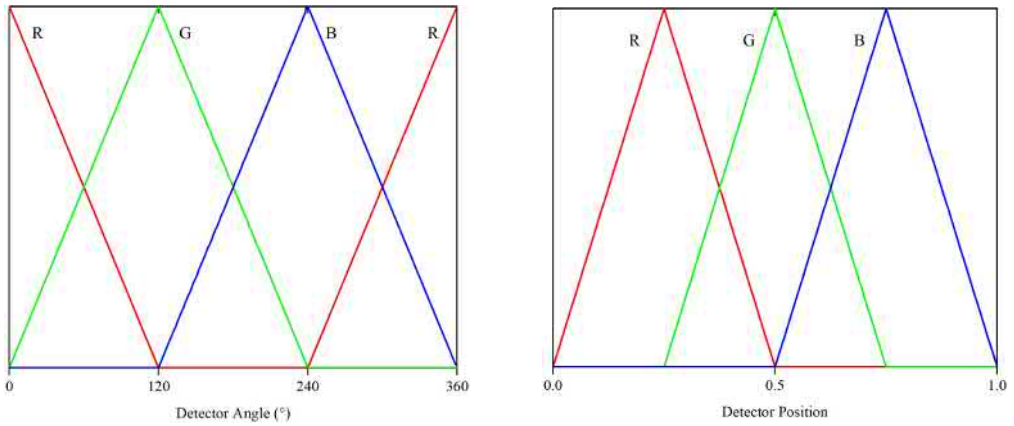

(a) circular deployment (b) linear deployment

Fig. 4.1 Deployment of chromatic processors

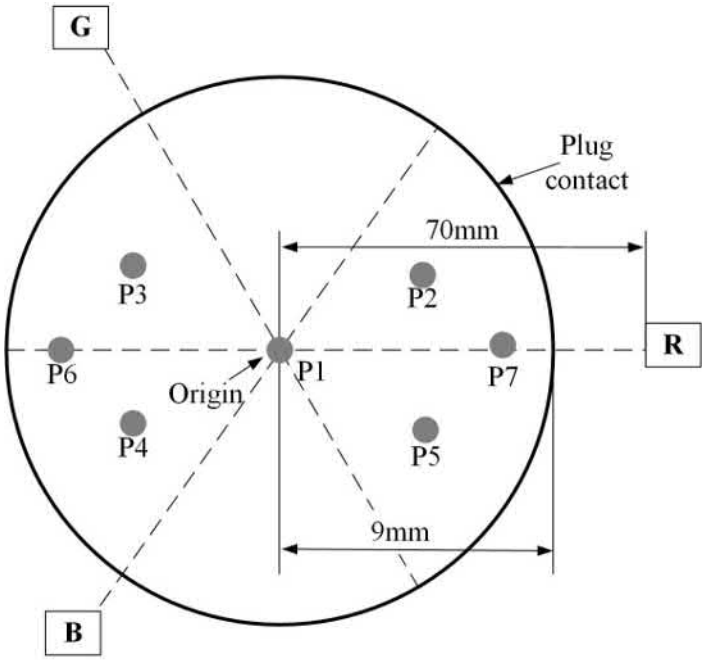

Fig. 4.2 Schematic diagram of the positions of seven selected points on a plug arcing contact (not to scale).

be less than 6% and 2.3%, respectively. Therefore, it is satisfactory to directly use the values of r_n and θ_d derived with the chromatic technique as approximate of the arc root coordinates (r, θ).

Table 4.1 Polar coordinates, dominant angle θ_d and nominal radius r_n of P1-P7.

Points	r(mm)	$\theta(^\circ)$	I_1	I_2	I_3	r_n	$\theta_d(^\circ)$
P1	0.0	0	0.45	0.45	0.45	0.00	0.0
P2	4.5	30	0.74	0.44	0.19	0.56	37.7
P3	4.5	150	0.19	0.74	0.44	0.56	157.7
P4	4.5	210	0.19	0.44	0.74	0.56	202.3
P5	4.5	330	0.74	0.19	0.44	0.56	322.3
P6	7.0	180	0.00	0.69	0.69	0.71	180.0
P7	7.0	0	1.00	0.20	0.20	0.79	0.0
R	70.0	0	-	-	-	-	-
G	70.0	120	-	-	-	-	-
B	70.0	240	-	-	-	-	-

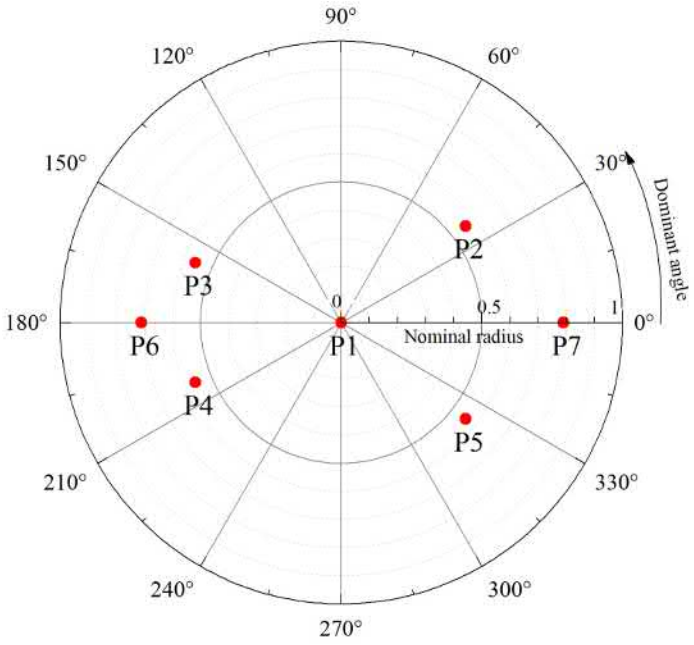

Fig. 4.3 Calculated dominant angle and nominal radius of P1-P7.

4.2.3 Trajectory of Arc Root Movement

By substituting the outputs of each PDD unit channel into Equations (4.4) and (4.5), the dominate angle θ_d and nominal radius r_n of test group CuWSF6-S can be calculated which are plotted in Figure 4.4 as function of time.

The variation of θ_d and r_n indicate circular and radial movement of the arc root respectively. At 5kA, θ_d varied largely from 0° to 330° indicating circular movement of the arc root while at 15kA and 40kA, θ_d kept constant at around 300° during the

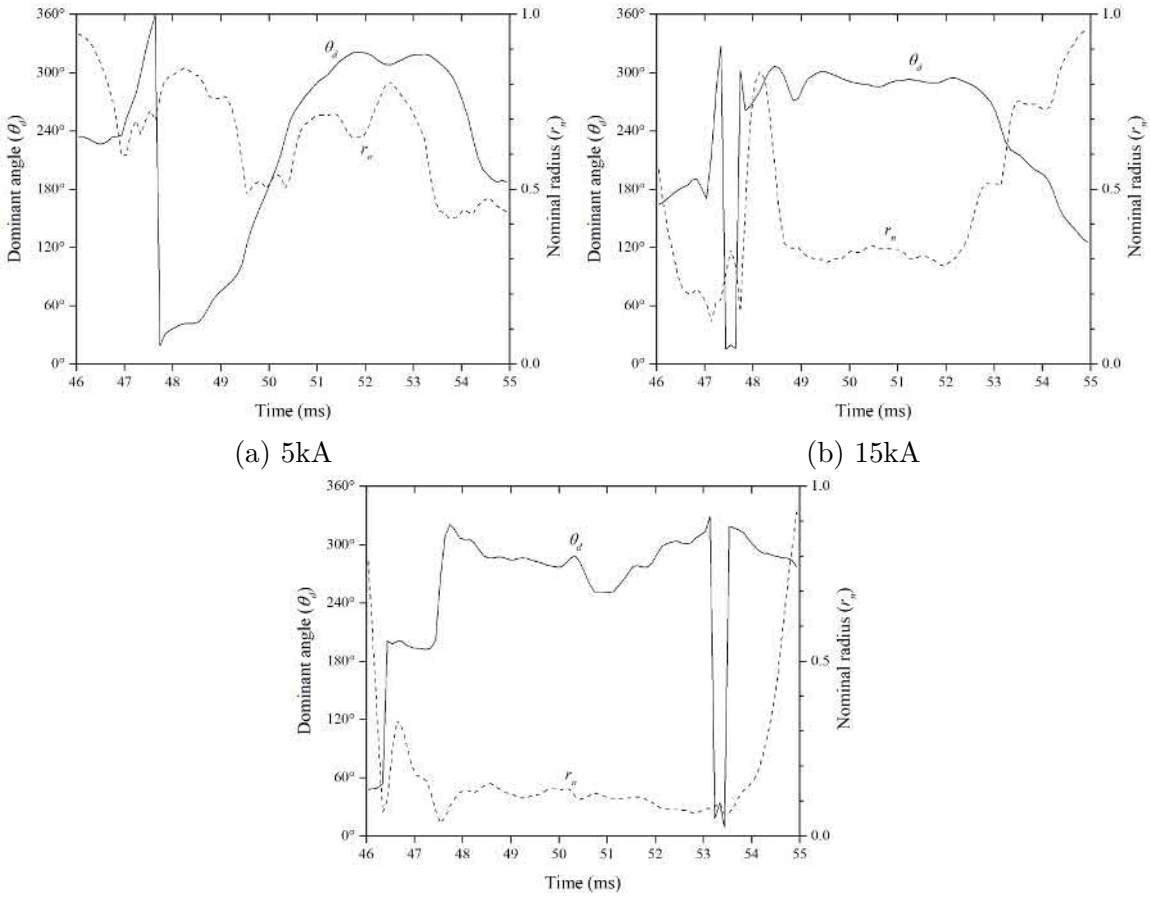

(a) 5kA (b) 15kA

(c) 40kA

Fig. 4.4 Dominant angle and nominal radius versus time at various currents.

middle/peak period of arcing. The value of r_n was larger than 0.5 at 5kA implying that the arc root was closer to the edge of the contact than the contact centre. As the current increased, the value of r_n decreased (approximate 0.3 at 15kA and 0.1 at 40kA) showing that the arc root moved closer to the centre of the contact surface. By plotting the dominant angle and nominal radius on polar plots, the trajectories of the arc root can be intuitively perceived, as shown in Figure 4.5.

4.2.4 Relationship of Arcing Contact Erosion and Activity of Movement of Arc Root

The analysis of high-speed photographs of the arc root (Section 3.4.3) and the measured arc root trajectories above, indicate that the patterns of interaction between the arc

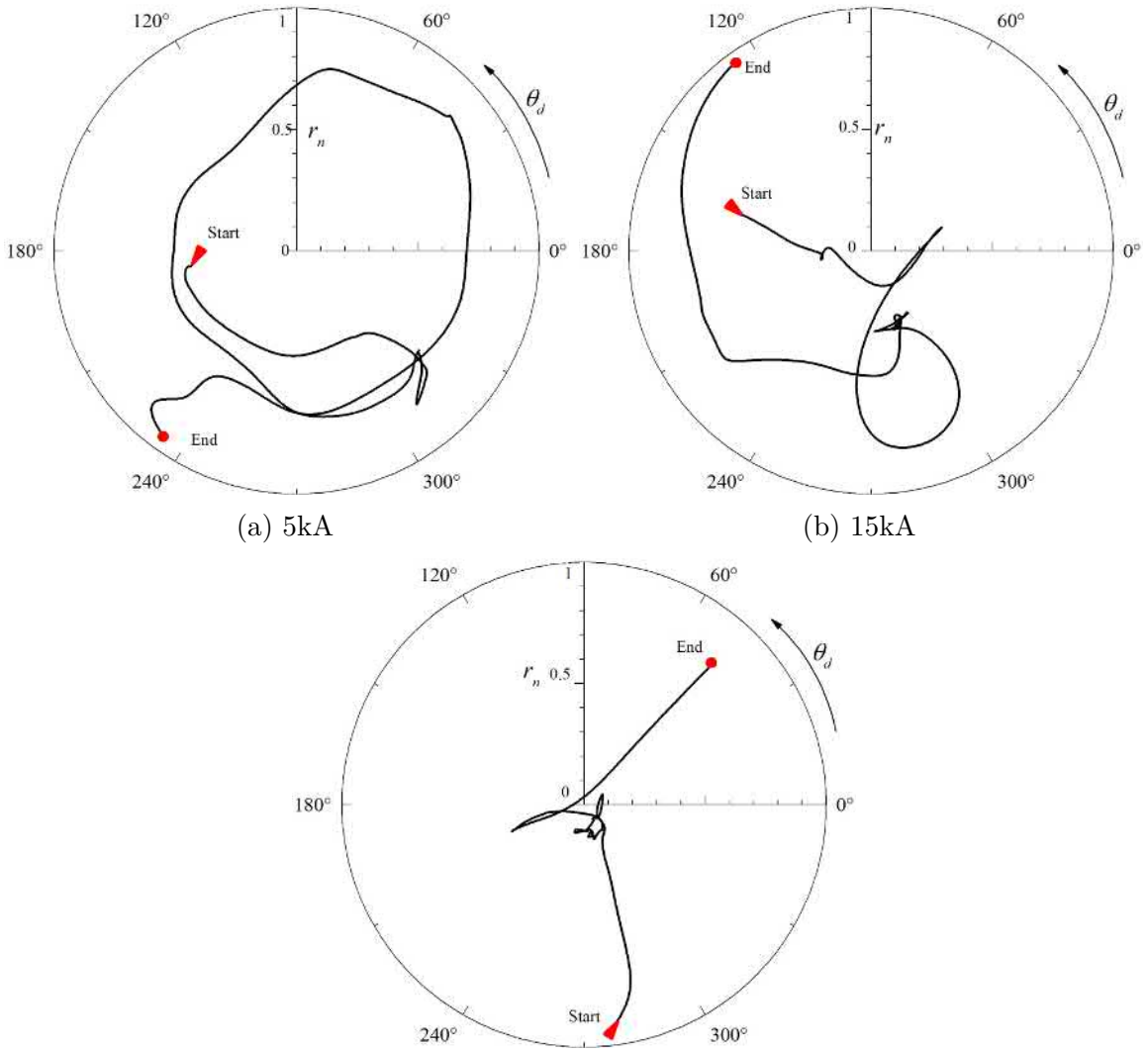

(a) 5kA (b) 15kA

(c) 40kA

Fig. 4.5 Trajectories of arc root on the contact surface at various currents.

root and arcing contact surface at various peak currents are different. The movement of the arc root at low currents (generally less than 10kA) is substantial. To investigate the effect of arc root movement on arcing contact mass loss, a parameter being called activity of movement d_{act} is introduced according to a simplified thermophysical model based on the following assumptions[83, 84]:

(1) the current density within the arc root j is constant value of j=1 $\times$ 10^8A/m^2 was used in this study[7];

(2) the arc root has a circular shape of radius r which can be derived as $r = \sqrt{i(t)/\pi j}$,

where $i(t)$ is the arc current as a function of time;

(3) the condition of the arcing contact surface is homogeneous in all directions.

The movement of the arc root on the contact surface can be illustrated by the model shown in Figure 4.6. At time t_1, the arc root has a radius r_1 and its centre locates at O_1. After a certain period of time Δt (=t_2-t_1), at t_2, the radius of the arc root changes to r_2, and the centre of the arc root moves a distance of d to the location of O_2. The arc root at t_1 and t_2 overlap in the shaded area (Figure 4.6) which suffers double heating from the arc. It follows that a larger overlapping area can potentially cause greater mass loss from the arcing contact.

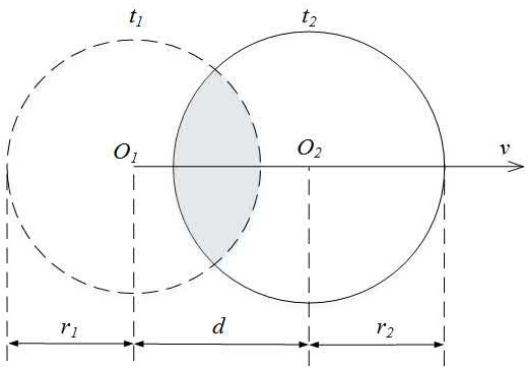

Fig. 4.6 Schematic diagram of arc root movement (r_1 and r_2 are the radius of the arc root at t_1 and t_2, respectively, d is the distance between the centres of arc roots O_1 and O_2).

For DC, the radius of the arc root may be assumed to be dependent of time i.e. r = constant so that $r_1 = r_2$. Thus the same value of d always represents the same area of overlapping. The sum of d during the discharging period is proportional to the repeated heating area which can sufficiently represent the mobility of the arc root. However, for AC, the radius of the arc root is a function of instantaneous current $i(t)$. For a certain value of d, it can be much larger than the arc radius at low current but smaller than the arc radius at high current. The activity of movement d_{act} is written as

$$\begin{aligned} d_{act} &= \frac{d}{r_1 + r_2} \qquad if \quad d < r_1 + r_2 \\ &= 1 \qquad\qquad\quad if \quad d \geq r_1 + r_2 \end{aligned} \tag{4.7}$$

Equation (4.7) indicates that d_{act} is a dimensionless parameter within the range 0-1. When $d < r_1 + r_2$, there is overlapping between the arc roots. A larger value of

d_{act} indicates a higher mobility of the arc root. d_{act}=0 implies that the arc root was stationary within the time interval of Δt. On the contrary, when $d \geq r_1 + r_2$, the overlapping area equals zero which indicates that the arc root has completely moved away from its last location within time Δt. In the range of 0-1, the larger the value of d_{act}, the longer the distance that the arc root effectively moves, and the weaker the heating at a fixed location on the arcing contact surface.

If the value of Δt is sufficiently large, there is always no overlapping area regardless of the mobility of the arc roots leading to a meaningless value of d_{act}=1 at all times. Therefore, an upper limit of the time interval Δt should be given as

$$\Delta t_{max} = \frac{\overline{D}}{\overline{v}} = \frac{2\sqrt{\overline{I}/\pi J}}{d_{tot}/t_{tot}} \tag{4.8}$$

where $\overline{D}$, $\overline{v}$, $\overline{I}$, J, d_{tot} and t_{tot} are the average arc root diameter, average arc root velocity, average current, current density, total arc root movement distance and total arcing time, respectively. According to the experimental results, for a test at 10kA, the value of Δt_{max} is approximately 0.5ms. The comparison of activity of movement among tests should be based on a consistent Δt.

The time of a current breaking test can be arbitrarily divided into n time slots, and $d_{act,i}$ (i = 1, 2, ..., n.) of each time interval can be calculated. The average activity of movement of the test is written as

$$\overline{d_{act}} = \frac{\sum_{i=1}^{n} d_{act,i}}{n}. \tag{4.9}$$

Since the mass loss of a CuW contact in SF_6 at 5kA was small (Figure 3.3), the analysis of arc root movement at this current level was excluded from the following discussion. The average activity of movement of an arc root on a CuW arcing contact in SF_6 from 10kA to 40kA were calculated (Δt=0.01ms was specified for all tests) and plotted in Figure 4.7.

Figure 4.7 shows that, generally, the mobility of the arc root decreased as the current increased. At 10kA and 15kA, the mass loss of arcing contact showed an exponential relationship with the activity of movement $\overline{d_{act}}$ of the arc root. A larger activity of movement always led to a lower mass loss at the same current level. By using

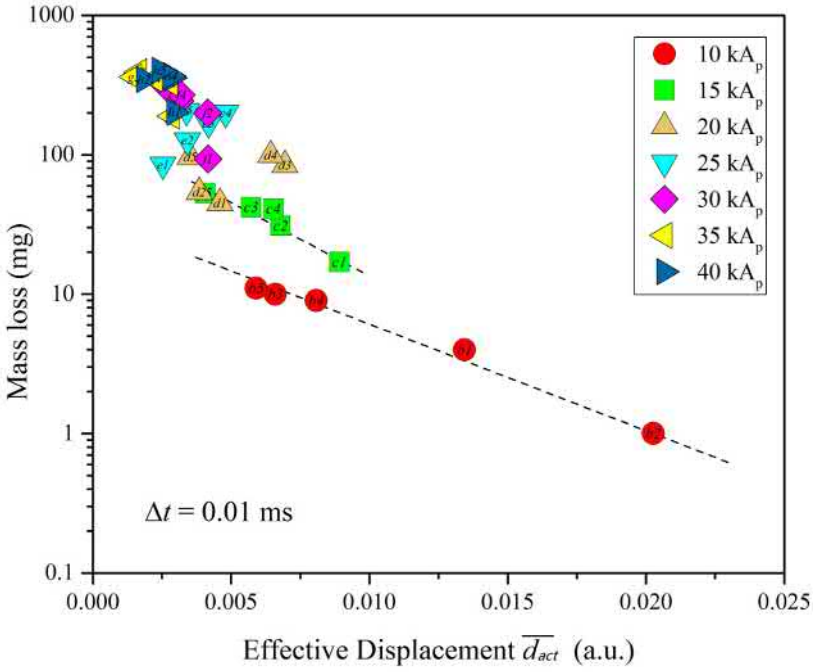

Fig. 4.7 Relationship between CuW contact mass loss in SF_6 and average activity of movement $\overline{d_{act}}$ of arc root.

the fitted curve to the 10kA and 15kA data shown in Figure 4.7, the mass loss of a plug contact can be estimated according to the calculated $\overline{d_{act}}$ at corresponding current levels. As the current increased, from 20kA to 40kA, the activity of movement of the arc roots were reduced to a relatively low level, and there was no strong correlation with mass loss. This is chiefly due to the following reasons. On the one hand, as discussed in Section3.4.3, once the area of the arc root became comparable to the area of the contact surface, the mobility of the arc root will be significantly reduced. On the other hand, at high currents, the mass loss of a single test was sufficiently high (up to approximately 400mg), therefore the change of the contact surface morphology became a prominent factor affecting the erosion process of the arcing contact.

In terms of the traditional arcing energy method, the average mass loss of arcing contact is always used as prediction value ignoring the influence of other factors. Using the spatial domain chromatic method, the contact mass loss is predicted by calculating the activity of arc root movement, which is essentially different from the traditional arcing energy method[85]. For the arc erosion test of the CuW contacts in SF_6, the

accuracy of mass loss prediction at 10kA and 15kA is increased by 31.0% compared with the arcing energy method (see Table 4.2).

Table 4.2 Comparison of accuracy of mass loss prediction of arcing contact: activity of arc root movement method vs arcing energy method.

Test code	Measured mass loss (g)	Arcing energy method (g)	Relative error of arcing energy method	Activity of movement method (g)	Relative error of activity of movement method
b1	0.004	0.007	70.0%	0.003	15.0%
b2*	0.001	0.007	580.0%	0.001	0.0%
b3	0.010	0.007	32.0%	0.010	4.0%
b4	0.009	0.007	24.4%	0.008	7.8%
b5	0.011	0.007	38.2%	0.012	10.0%
c1	0.017	0.037	116.5%	0.019	11.8%
c2	0.031	0.037	18.7%	0.031	0.3%
c3	0.042	0.037	12.4%	0.041	1.9%
c4	0.041	0.037	10.2%	0.036	12.2%
c5	0.053	0.037	30.6%	0.059	10.9%
Average relative error			39.2%		8.2%

* Since the mass loss measured by this experiment is too small, there is a large experimental error, so it is excluded from the accuracy analysis.

4.3 Summary

In this chapter, the macroscopic arc behaviour in HVCB and its effect on arcing contacts erosion have been studied from two aspects.

First, the arc behaviour was derived by using the high-speed photographs presented in Chapter 3. The photographs showed that the shape of the arc column was not cylindrically symmetrical which was especially so at low currents. As the current increases, the diameter of arc column increases and the arc stability is also enhanced. The temporal distribution of copper vapour in the arc column is closely related to the amplitude of the peak current. The arc root is more likely to occupy the edge position and moves rapidly on the contact surface. As the current increases, the arc root area

gradually approaches the contact surface area, and the mobility of the arc is reduced. As the test number increases, the ejection of metallic droplets from the plug contact surface is gradually enhanced.

Second, a quantitative relationship between the activity of movement of the arc root ($\overline{d_{act}}$) and mass loss of a plug arcing contact was derived by using the spatial domain chromatic methods. The activity of movement of the arc root is inversely correlated with the mass loss of the plug contact at currents lower than 15kA. The prediction accuracy of the mass loss of arcing contact is improved by 31.0% compared to the arcing energy method.

Chapter 5

Study of Arcing Contact Erosion Based on Chromatic Analysis of Arc Spectra

The arc plasma emission spectrum contains a large amount of information related to the arc state. Through the traditional spectral analysis, a number of parameters such as temperature, pressure and particle density can be derived. However, traditional optical emission spectroscopy techniques requires that the arc plasma satisfy the strict conditions such as LTE, collision-dominated and optically thin, which are not always applicable to the breaking arc in HVCB. Therefore, the utilization of conventional OES methods has been limited.

In this chapter, time-resolved spectra of the arc plasma are processed and analysed using chromatic methods. Firstly, the chromatic analytic techniques and procedures - wavelength and time domain chromaticity - are demonstrated and the linear regression method is also briefly introduced. Secondly, the time-resolved arc spectra of various experimental conditions are processed using wavelength and time domain chromatic methods successively. The raw graphs of chromatic parameters x, y, z, H, L, S are presented for wavelength domain chromaticity at peak current and the time domain chromaticity. Thirdly, the processed chromatic parameters are presented and interpreted. The quantitative relationship between the chromatic parameters of the arc

spectra and the mass loss of the arcing contact is built up based on linear regression method.

5.1 Analysis Techniques and Procedures

5.1.1 Chromatic Analysis

The arc spectra $S(\lambda, t)$ captured by the high-speed spectrometer is a function of both wavelength λ and time t. On one hand, the wavelength domain contains information, at least, regarding the species of the arc; on the other hand, the time domain includes the information of time variation of the compositions of the arc.

Wavelength Domain Data Processing

Unlike the spatial domain chromaticity, in which the wavelength domain data processing involves three signal processors distribute along the wavelength axis. The outputs of the spatial domain fibre optic sensors are determined by their installed locations and response parameters, the outputs of wavelength domain processors are primarily determined by their wavelength response profiles. With respect to an unknown system, it is always the first choice to select a set of evenly distributed Gaussian processors which covers the whole parameter (i.e., wavelength) range of interest as shown in Figure 5.1. The overlap between neighbouring processors is set to 50% of the peak height leading to a relative uniform response of the value of Hue (derived from HLS transformation, Section A.2.2)[86].

The wavelength domain processors are designated as $R_{w,ev}$, $G_{w,ev}$ and $B_{w,ev}$ (the subscript w represents "wavelength" and ev represents "evenly", and the centre of each processor locates at 475nm, 550nm and 625nm, respectively. To avoid confusion, it should be stressed that, in this context, the letters R, G and B do not correspond to the colour of red, green and blue in the visible spectral range.

The outputs of the processors, namely R_0, G_0, B_0, can be calculated according to Equations (A.1) to (A.3). The primary wavelength domain chromatic parameters H_w, L_w, 1-S_w (representing the dominant wavelength, effective signal strength and nominal signal spread, respectively) are derived using the HLS transformation (Equations (A.4)

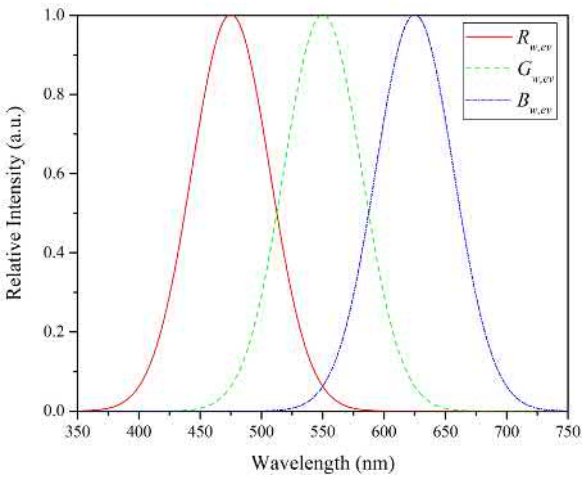

Fig. 5.1 Evenly distributed wavelength domain processors $R_{w,ev}$, $G_{w,ev}$ and $B_{w,ev}$.

to (A.8)), and parameters x_w, y_w, z_w (representing the relative signal strength under the coverage of processors $R_{w,ev}$, $G_{w,ev}$, $B_{w,ev}$, respectively) are derived using the xyz transformation (Equations (A.12) to (A.14)).

Time Domain Data Processing

During the current breaking operation, the AC arc changes continuously without reaching a steady state, therefore, the time variation of the arc spectra contains much information related to the arcing contact erosion. To address the characteristics of time variation of the arc spectra, the wavelength domain chromatic parameters can be plotted as function of time. Chromatic time domain precessing of the arc spectra deals with the variation of the wavelength domain chromatic parameters ($x_w(t)$, $y_w(t)$, $z_w(t)$, $H_w(t)$, $L_w(t)$ and 1-$S_w(t)$), rather than the spectra at a specific wavelength ($S(\lambda_i, t)$). Therefore, the time domain chromatic processing can be regarded as a secondary chromatic processing of the arc spectra. Accordingly, the wavelength domain chromatic processing is a primary chromatic processing of the arc spectra.

The selection of time domain processors is determined by the arcing time. In general, the processors need to cover the entire period of arcing. According to the time of the AC trigger of different test sets (Table 3.1), the selected time domain processors used in this study are shown in Figure 5.2.

The time location of the maximum of the processors for CuN2-S are at 53ms, 56ms and 59ms (Figure 5.2 (a)), and for CuWSF-S and CuWSF-G are at 48ms, 51ms and

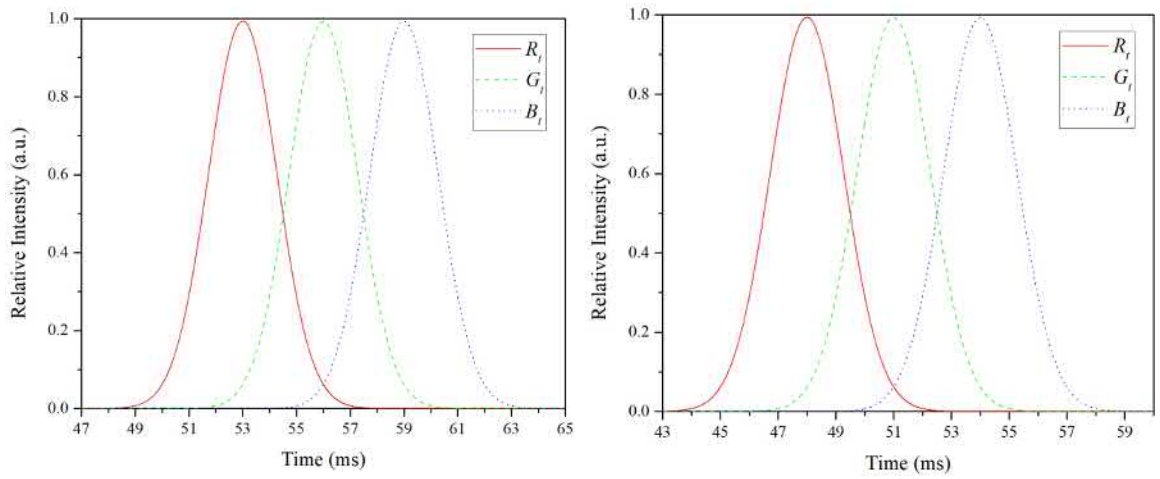

(a) CuN2-S (b) CuWSF-S and CuWSF-G

Fig. 5.2 Time domain processors for different test sets.

54ms (Figure 5.2 (b)), respectively. The overlap between the neighbouring processors is set to be 50% of the peak height. The time domain processors are designated as R_t, G_t and B_t (the subscript t represents "time").

When the time domain chromatic processors are applied to each of the wavelength domain parameters and the outputs of these processors can be expressed as following

$$\begin{aligned} R0_{t,W} &= \int_t W(t) \cdot R_t(t)dt \\ G0_{t,W} &= \int_t W(t) \cdot G_t(t)dt \\ B0_{t,W} &= \int_t W(t) \cdot B_t(t)dt \end{aligned} \tag{5.1}$$

where W represents the wavelength domain chromatic parameters namely x_w, y_w, z_w, H_w, L_w and 1-S_w. By using HLS and xyz transformations (Equation (A.4)-(A.14)), another six time domain chromatic parameters can be derived for each wavelength domain chromatic parameter. Therefore, a total of 36 time domain chromatic parameters can be obtained as listed in Table 5.1. For example, $z_{t,hw}$ represents the time domain parameter z_t related to H_w (time range covered by B_t of $H_w(t)$).

To provide a holistic view of the chromatic methods of data processing used in this chapter, Figure 5.3 shows the flow chart of chromatic processing of arc spectra where both m and n can be x, y, z, H, L or S.

Table 5.1 List of secondary (time domain) chromatic parameters.

Transformations	$x_w(t)$	$y_w(t)$	$z_w(t)$	$H_w(t)$	$L_w(t)$	1-$S_w(t)$
xyz	$x_{t,xw}$	$x_{t,yw}$	$x_{t,zw}$	$x_{t,hw}$	$x_{t,lw}$	$x_{t,sw}$
	$y_{t,xw}$	$y_{t,yw}$	$y_{t,zw}$	$y_{t,hw}$	$y_{t,lw}$	$y_{t,sw}$
	$z_{t,xw}$	$z_{t,yw}$	$z_{t,zw}$	$z_{t,hw}$	$z_{t,lw}$	$z_{t,sw}$
HLS	$H_{t,xw}$	$H_{t,yw}$	$H_{t,zw}$	$H_{t,hw}$	$H_{t,lw}$	$H_{t,sw}$
	$L_{t,xw}$	$L_{t,yw}$	$L_{t,zw}$	$L_{t,hw}$	$L_{t,lw}$	$L_{t,sw}$
	$S_{t,xw}$	$S_{t,yw}$	$S_{t,zw}$	$S_{t,hw}$	$S_{t,lw}$	$S_{t,sw}$

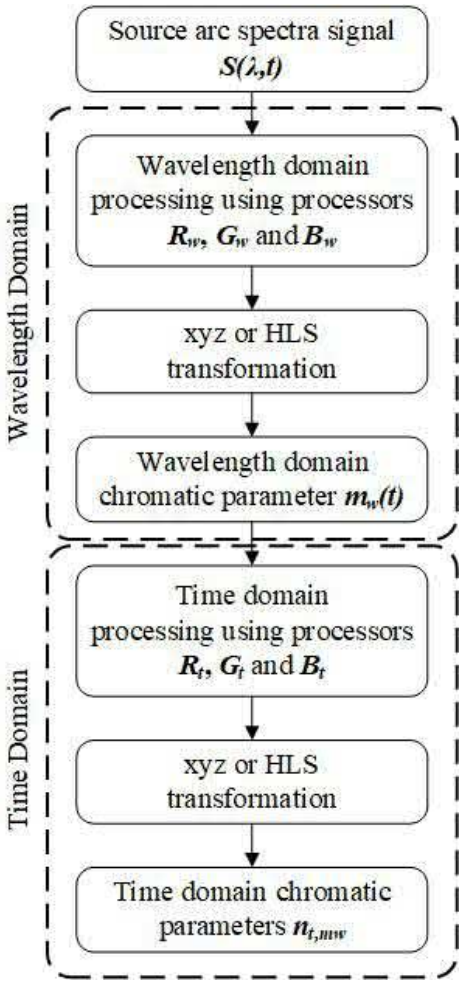

Fig. 5.3 Flow chart of chromatic processing of arc spectra.

5.1.2 Linear Regression Method

In the previous investigations of arcing contacts erosion, the average mass loss value of contacts were always used to represent the degree of erosion after a number of

consecutive tests under the same experimental conditions. However, the mass loss of each single test was unknown and could vary substantially (Figure 3.2 and 3.3). For the purpose of on-line monitoring of contact erosion of HVCB, it is necessary to offer a specific value of mass loss to represent the erosion degree of arcing contact after each single operation.

By using the obtained chromatic parameters (both in wavelength and time domains), the quantitative relationship between the mass loss of arcing contact and the arc spectra can be evaluated using the Linear Regression methods. It is assumed that the mass loss Δm (unit: mg) can be given by the following formula

$$\Delta m = \beta_0 P_0 + \beta_1 P_1 + ... + \beta_n P_n + C \tag{5.2}$$

where β_n is the regression coefficient, P_n is the chromatic parameter, the subscript n represents the number of parameters used in the expression and C is a constant.

Based on the actual measured arcing contact mass loss data and chromatic parameters of arc spectra, the regression coefficient β_{n} and the constant C can be solved by using the method described in the literature [87] and the data analysis software SPSS[88].

5.2 Chromatic Processing of Arc Spectra

5.2.1 Wavelength Domain Processing at Peak Arc Current

Cu Contact Erosion in N_2

By using the processor distributions shown in Figure 5.1, the arc spectra of a test set CuN2-S (Cu arcing contact in N_2) at current peak time t_p (Figure 3.28) are processed. The outputs of the processors are denoted as $R0_{w,ev}$, $G0_{w,ev}$ and $B0_{w,ev}$. Then the wavelength domain chromatic parameters $x_w(t_p)$, $y_w(t_p)$, $z_w(t_p)$, $H_w(t_p)$, $L_w(t_p)$ and 1-$S_w(t_p)$ are derived. Each of these parameters is displayed graphically as a function of mass loss of a plug arcing contact as shown in Figure 5.4. Each circle represents a single test and the test number is designated inside the circle. The colour of the circle represents the value of mass loss according to the colour bar of Figure 3.2.

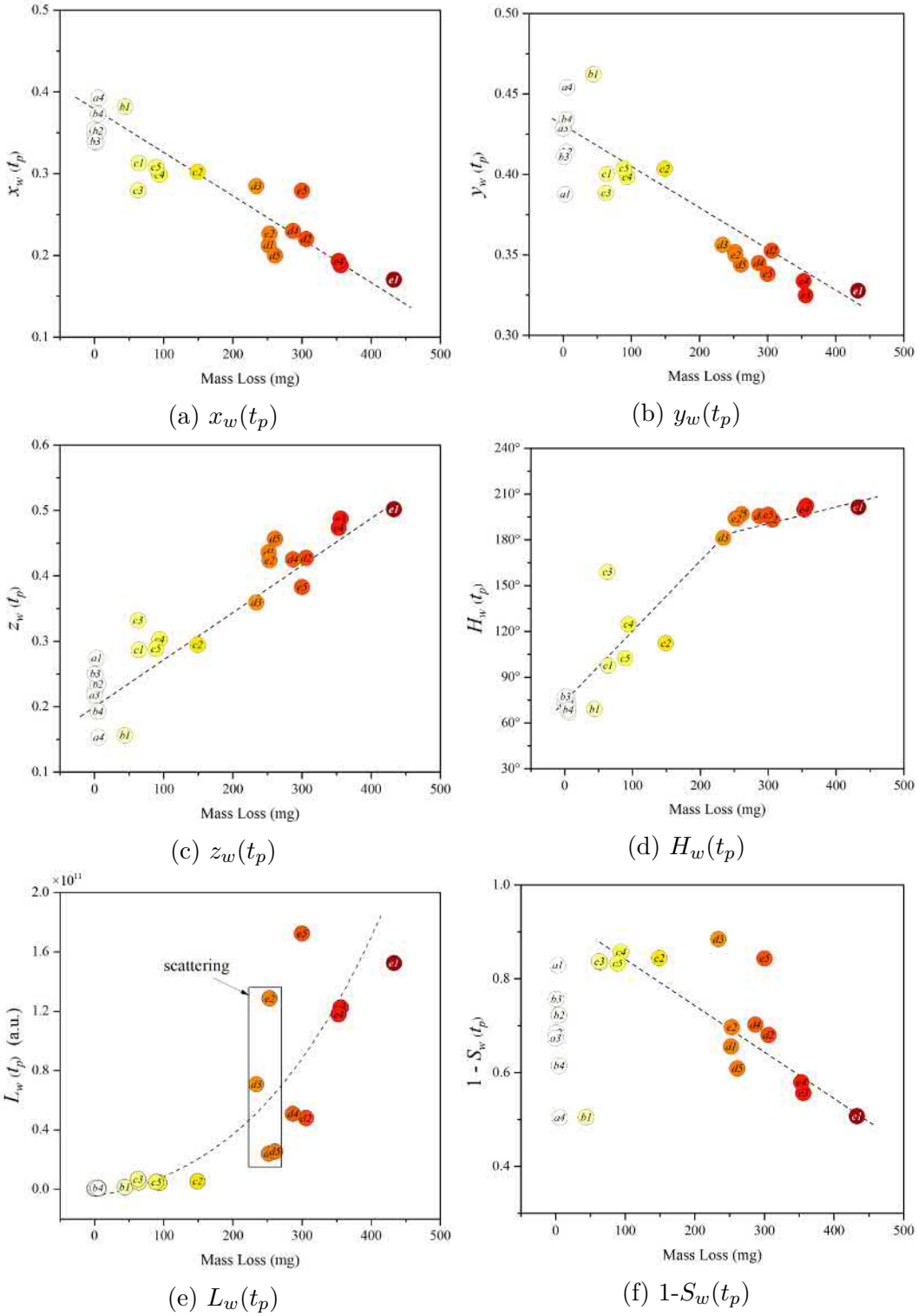

(a) $x_w(t_p)$ (b) $y_w(t_p)$

(c) $z_w(t_p)$ (d) $H_w(t_p)$

(e) $L_w(t_p)$ (f) 1-$S_w(t_p)$

Fig. 5.4 Wavelength domain chromatic parameters at peak current moment t_p versus mass loss of Cu arcing contact in N_2.

As shown in Figure 5.4, all six wavelength domain chromatic parameters have monotonic relationship with the mass loss values. Generally, $x_w(t_p)$, $y_w(t_p)$ and 1-$S_w(t_p)$ decreased with mass loss while $z_w(t_p)$, $H_w(t_p)$ and $L_w(t_p)$ increased with mass loss.

Specifically, the chromatic parameters $x_w(t_p)$, $y_w(t_p)$ and $z_w(t_p)$ provide the information of spectral changes in different wavelength bands according to the selected processors. In Figure 5.4 (a), the value of $x_w(t_p)$ is roughly in the range of 0.17-0.40 which indicates that the relative signal strength of the wavelength band covered by the processor $R_{w,ev}$ accounts for 17% to 40% of the entire wavelength range. In Figure 5.4 (b), the variation of $y_w(t_p)$ has a similar trend to $x_w(t_p)$, and its value lies in the range of 0.32-0.46. In Figure 5.4 (c), $z_w(t_p)$ is approximately in the range of 0.14-0.51. It is found that, in the case of small mass loss (<200mg), the relative spectral emission from $R_{w,ev}$ and $G_{w,ev}$ bands (Figure 5.4 (a), (b)) are higher than that of $B_{w,ev}$ (Figure 5.4 (c)). As the mass loss increased, the relative spectral emission from $B_{w,ev}$ band account for approximately 51% of the total radiative energy in the visible wavelength range. Reference to Figure 3.28 (e) and (f) indicates that the increasing $z_w(t_p)$ is associated with the increasing of continuum spectral emission.

The other three wavelength chromatic parameters $H_w(t_p)$, $L_w(t_p)$ and 1-$S_w(t_p)$ can provide information of holistic variations of the arc spectra.

Figure 5.4 (d) shows that the dominant wavelength $H_w(t_p)$ varies in the range of approximately 70° to 210°. At low mass loss (tests $a1 - a5$, $b1 - b5$), the value of $H_w(t_p)$ is around 70° implying that the equivalent centre of the arc spectrum is at a position between the processors $R_{w,ev}$ and $G_{w,ev}$ (i.e., ∼520nm) which can be observed from Figure 3.28 (a) and (b). In the case of high mass loss (tests $d1 - d5$ and $e1 - e5$), the $H_w(t_p)$ value increases up to approximately 210° indicating that the dominant wavelength is in between the centre of $G_{w,ev}$ and $B_{w,ev}$. Reference to Figure 3.28 (e) and (f), indicates that the continuum spectrum accounts for a great major part of the total optical energy (this is presumed the main cause of the change of $H_w(t_p)$ value). In respect to tests $c1 - c5$, $H_w(t_p)$ varies substantially in a large range. This is probably due to the perturbation of the arc column in the arcing channel.

Figure 5.4 (e) shows the effective signal strength $L_w(t_p)$ as function of mass loss suggests that the optical emission intensity generally increases with mass loss. To a

certain degree, the value of $L_w(t_p)$ provides an indication of the peak current values. However, for low mass loss, the scattering of $L_w(t_p)$ can be high. The optical energy dispersed in the surroundings of the arc column does not sufficiently related to the mass loss of arcing contact. Therefore, it is not wise to simply used the effective signal strength of the arc spectra (of the arc column) as an indicator of arcing contact erosion.

Figure 5.4 (f) shows the variation of 1-$S_w(t_p)$ against mass loss. At low mass loss, the value of 1-$S_w(t_p)$ is high and does not vary with contact mass loss. This is probably due to the movement of the arc root on the contact surface resulting in the arc spectral emission not being synchronized with the peak current time. During a half cycle of current, the movement of the arc root is unpredictable, and the arc root may stay at any specific location at any moment. If the arc root remains fixed during the current peak period, there will be strong emission from Cu atoms which will result in a distinguishing peak around 522nm, and therefore a low value of 1-$S_w(t_p)$. Otherwise, if the arc root does not remain fixed at the time of current peak, a large value of 1-$S_w(t_p)$ will be obtained. As the current increased, the value of 1-$S_w(t_p)$ shows a decreasing trend with mass loss which is primarily caused by the intense optical emission from the band of $B_{w,ev}$ (an effective peak in the band of $B_{w,ev}$).

From the above discussion, it has been found that each of the six wavelength domain chromatic parameters ($x_w(t_p)$, $y_w(t_p)$, $z_w(t_p)$, $H_w(t_p)$, $L_w(t_p)$ and 1-$S_w(t_p)$) corresponds to a specific aspects of the arc emission. Instead of using six individual plots against mass loss (Figure 5.4), the information contains in these parameters can be represented more concisely using three chromatic maps as shown in Figures 5.5 and 5.6.

With regard to Figure 5.5 it should be noted that since $x+y+z = 1$ (Equation A.15) the z parameter is also represented on this figure. Therefore, the information implied by xyz values can be unambiguously expressed in one Cartesian plot compactly with the mass loss value denoted by the colour of the points, as shown in Figure 5.5. This map shows that the values of x_w and y_w both decreased as the mass loss increased. The dashed line represents the value of x=y, and the solid black dot represents the equivalence point where $x_w = y_w = z_w = 0.33$. The point located near the equivalence point indicate that the optical energy is relatively evenly distributed throughout the entire visible wavelength range. By contrast, the further the points are away from the equivalence point, the imbalance of the optical energy distribution is more

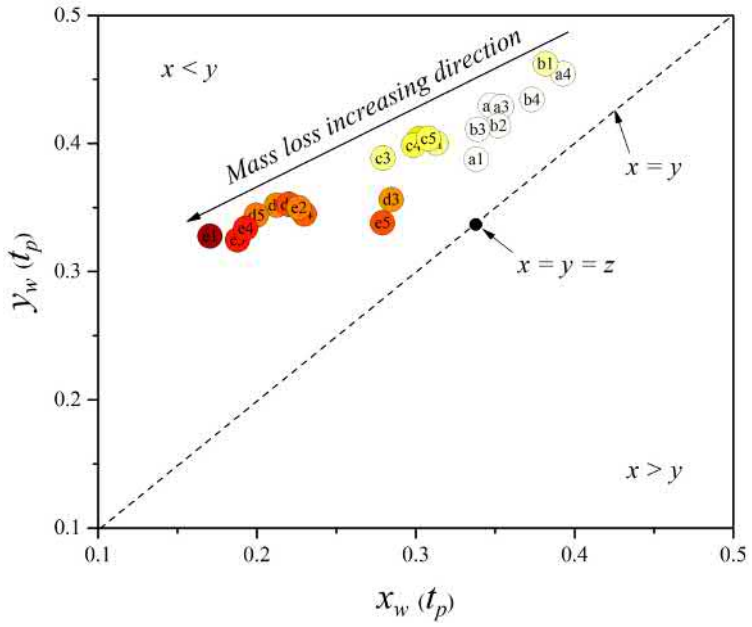

Fig. 5.5 Erosion trend of Cu arcing contact in N_2 represented by $x_w(t_p)$ and $y_w(t_p)$.

pronounced. Consequently, the relative signal strength of different wavelength bands can be conveniently compared.

The value of HLS can be shown on two polar maps, namely H-L and H-(1-S) as shown in Figure 5.6. In these two plots, the variation of dominant wavelength (H), effective signal strength(L) and nominal signal spread(1-S) as function of mass loss can be intuitively observed.

Figure 5.6 (a) shows the variation of $H_w(t_p)$ and $L_w(t_p)$ along with mass loss. For the tests of low mass loss (tests a1-a5, b1-b5, c1-c5), the effective signal strength $L_w(t_p)$ is very low (close to zero point). As the mass loss increased, the effective signal strength $L_w(t_p)$ also increased. In addition, for the high mass loss tests, the increasing of $H_w(t_p)$ indicates the direction of mass loss increasing (as designated by the bold arrow).

Figure 5.6 (b) shows the variation of $H_w(t_p)$ and 1-$S_w(t_p)$ along with mass loss. From this plot, the variation of $H_w(t_p)$ with mass loss is more clearly apparent. The dominant wavelength of the low mass loss tests lie mostly in the range between 60° and 90°. As the mass loss increased, $H_w(t_p)$ shifted to around 200°. In addition, the nominal spread of the arc spectra 1-$S_w(t_p)$ generally shows a scatter before increasing along with mass loss (Figure 5.4 (f)).

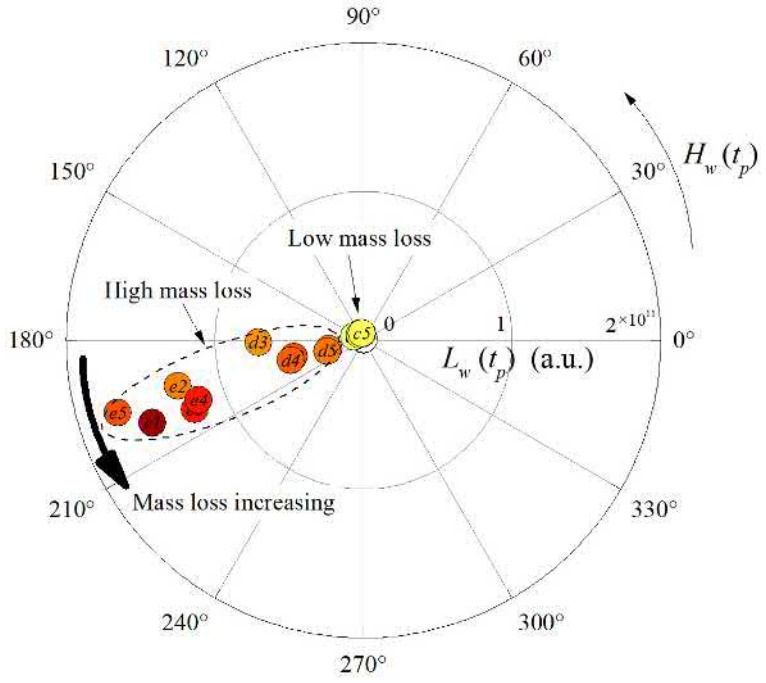

(a) H-L

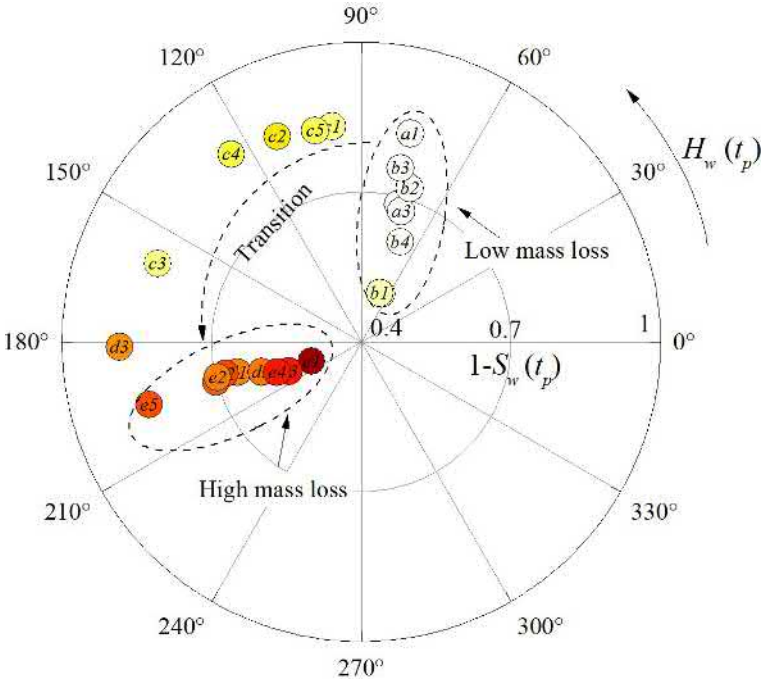

(b) H-(1-S)

Fig. 5.6 Chromatic polar maps of erosion trend of Cu arcing contact in N_2.

CuW Contact Erosion in SF_6

The characteristics of arc emission from the plug contact region of test set CuWSF6-S (CuW arcing contact in SF_6) have been studied using the similar methods to those

described in the previous section (Section 5.2.1). It should be noted that the optical arrangement in this case was different from that used for the test set CuN2-S of Section 5.2.1.

Figure 5.7 presents the wavelength domain parameters $x_w(t_p)$ versus $y_w(t_p)$ of the test set CuWSF6-S. The colour of each point represents the mass loss of the test according to the colour bar in Figure 3.3. Two different patterns of chromatic parameter variation are shown in the figure with respect to low current and high current, respectively.

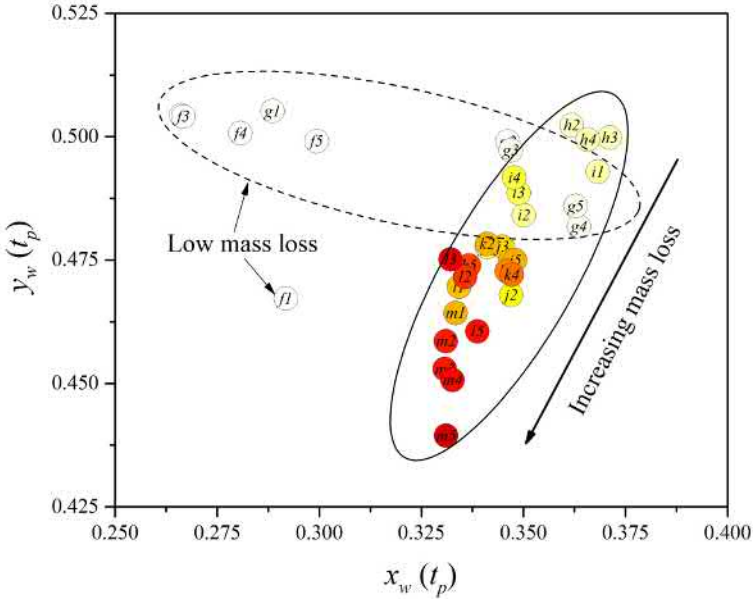

Fig. 5.7 Erosion trend of CuW arcing contact in SF_6 represented on a $x_w(t_p)$ versus $y_w(t_p)$ map.

At high currents (over 10kA$_p$, tests h1-m5), the data points primarily locate in the solid ellipse area and vary according to the solid arrow as the mass loss increases. Information about the arc spectra as a function of mass loss can be deduced from this pattern. First, since $y_w(t_p)$ is approximately between 0.43 and 0.51, it indicates that there is strong emission in the $G_{w,ev}$ band. Detailed arc spectra (Figure 3.29) show that the spectral line emission from Cu atoms is overriding at high currents which is covered by the processor $G_{w,ev}$. Secondly, as the mass loss increased, the values of both $x_w(t_p)$ and $y_w(t_p)$ decreased indicating that the optical emission in the $B_{w,ev}$ band became influential for the tests of high mass loss.

At low currents (from 5kA$_p$ to 10kA$_p$, tests f1-g5), the data points fall in the dash circle area which is different from the high current tests. As shown in Figure 3.29 (a) and (b), the spectral line emission from the metallic atoms is not predominant implying that the vaporisation of contact material is less prominent. The arc root has been shown to have a substantial effect on arcing contact erosion at low currents(Section 4.2.4), thus, the spectral emissions are also effected. The scattering of the chromatic parameters is mainly caused by the arc root movement.

Figure 5.8 (a) shows the variation of wavelength domain chromatic parameters $H_w(t_p)$ and $L_w(t_p)$. The solid arrow represents the direction of mass loss increasing. As the mass loss increases, the value of $L_w(t_p)$ increases indicating that the total optical energy received by the sensors was increased. The value of $H_w(t_p)$ remains at around 80° for most of the test especially at high currents. A relative constant $H_w(t_p)$ indicates that the shape of the arc spectra does not change significantly. This is different from the case of tests in CuN2-S (Figure 5.6 (a)) because the aperture of the optical sensor was limited to the arc root region where the line emission from metallic atoms was dominant for most cases.

Figure 5.8 (b) shows the variation of wavelength domain chromatic parameters 1-$S_w(t_p)$ along with $H_w(t_p)$. As the mass loss increases, the nominal spread of the spectral signal 1-$S_w(t_p)$ increases as well. This indicates that although the emission from copper atoms (in $G_{w,ev}$ band) was always prominent, the relative intensities of emission from $R_{w,ev}$ and $B_{w,ev}$ bands also increased. As expanded view of the results (solid rectangle insert Figure 5.8 (b)) show that the increasing trend of 1-$S_w(t_p)$ is not strictly monotonic, some tests of relative low mass loss such as l1 and m1 have larger value of 1-$S_w(t_p)$.

5.2.2 Time Domain Processing

In the previous section, the characteristics of the arc spectra $S(\lambda, t)$ in wavelength domain under various experimental conditions were investigated. It was found that, regardless of the experimental conditions, the variation of wavelength domain chromatic parameters at the peak current time t_p (i.e. $x_w(t_p)$, $y_w(t_p)$, $z_w(t_p)$, $H_w(t_p)$, $L_w(t_p)$, 1-$S_w(t_p)$) are closely related to the mass loss of plug arcing contact. Further, the time

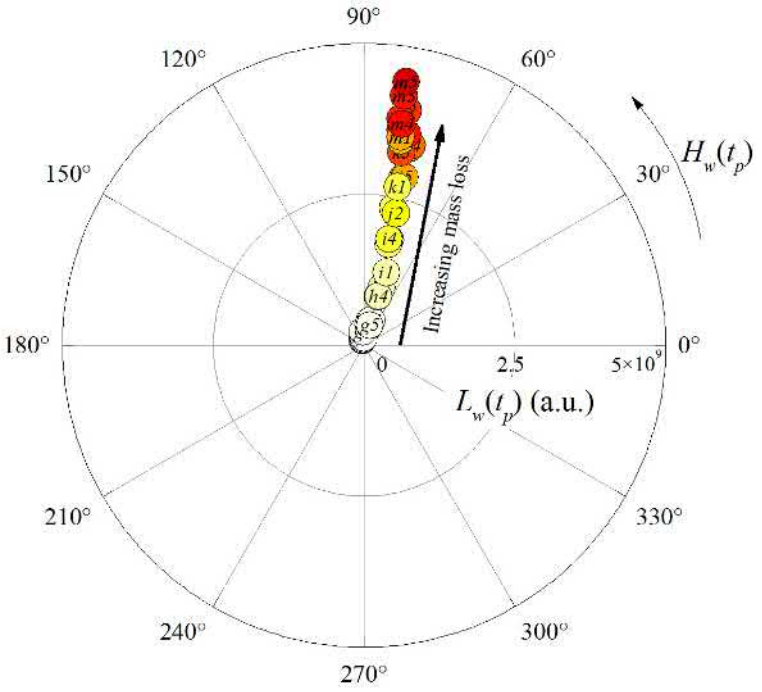

(a) H-L

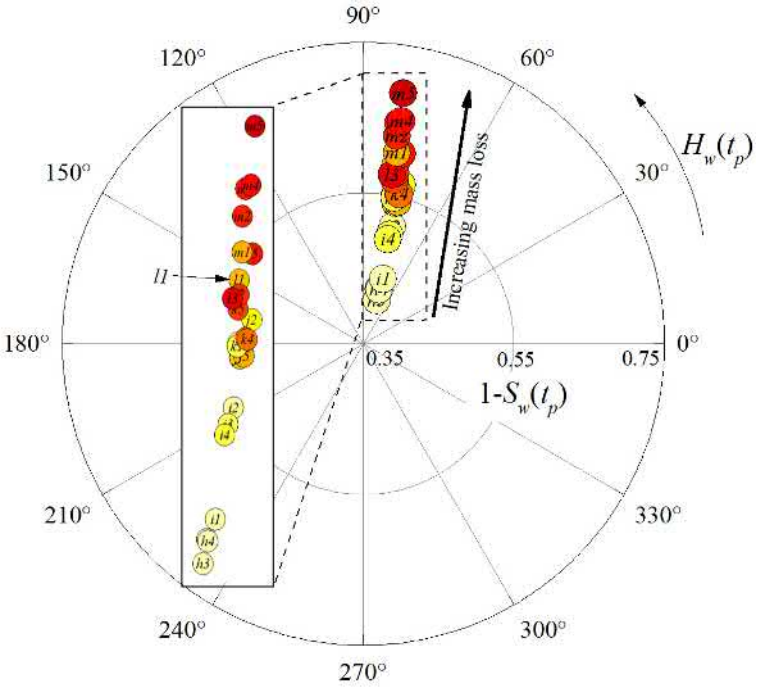

(b) H-(1-S)

Fig. 5.8 Chromatic polar maps for the erosion trend of CuW arcing contact in SF_6.

variation of the wavelength domain chromatic parameters are studied and associated with the mass loss of arcing contact in this section.

Cu Contact Erosion in N_2

Figure 5.9 shows the time variation of wavelength domain chromatic parameters $x_w(t)$, $y_w(t)$, $z_w(t)$, $H_w(t)$, $L_w(t)$ and 1-$S_w(t)$ for various peak current amplitudes.

Figure 5.9 (a) shows that amplitudes of $x_w(t)$ (initial time interval of 8ms) generally decreases as the current increases. At 5kA, $x_w(t)$ increases slightly with time. By contrast, for a test of high mass loss (at 25kA), the value of $x_w(t)$ decreases sharply at the beginning of the test, reaches its minimum at the current peak time (56ms) and then increases gradually during the time interval 56-61ms. Figure 5.9 (b) shows that $y_w(t)$ also gradually decreases as the current increases. For a specific test, the value of $y_w(t)$ generally increases over time and reaches a maximum at the end of each test. Because of the chromatic relationship $z_w(t)$ = 1- $x_w(t)$-$y_w(t)$ (Equation A.15), the value of $z_w(t)$ shows opposite trends against $x_w(t)$ and $y_w(t)$ (Figure 5.9 (c)), i.e. $z_w(t)$ increases with current.

Figure 5.9 (d) shows the time variation of the dominant wavelength $H_w(t)$. As the current increases, the maximum value of $H_w(t)$ increases from approximately 70° at 5kA$_p$ to 200° at 25$_p$ over the time of arcing. The higher the current, the earlier $H_w(t)$ reached its maximum. Figure 5.9 (e) shows time variation of the effective signal strength (i.e. optical intensities) $L_w(t)$ of the tests which generally increases as the current increases. Figure 5.9 (f) shows the time variation of the nominal signal spread 1-$S_w(t)$. At high currents, i.e. 20kA and 25kA, a sudden decline of 1-$S_w(t)$ is observed in the medium time period.

From the above analysis, it is clearly shown that the mass loss of arcing contacts has strong correlation with the time domain chromatic parameters.

In Figure 5.10, $x_{t,xw}$ and $y_{t,xw}$ represent the relative amplitudes of $x_w(t)$ (Figure 5.4 (a)) at the early and middle time periods. As the mass loss increases, the value of $x_{t,xw}$ increases and $y_{t,xw}$ decreases.

In Figure 5.11, $H_{t,hw}$ represents the time of the maximum "dominant wavelength" appearing and $L_{t,hw}$ represents the effective signal strength corresponding to the "dominant wavelength". For the low mass loss, the value of of $H_{t,hw}$ is between 240° and 360° indicating that there are two peaks of $H_w(t)$ appearing at the early and late time periods, respectively. The value of $L_{t,hw}$ is relatively low implying that the dominant wavelength locates in the range of $R_{w,ew}$ and $G_{w,ev}$ for most of the time (low value

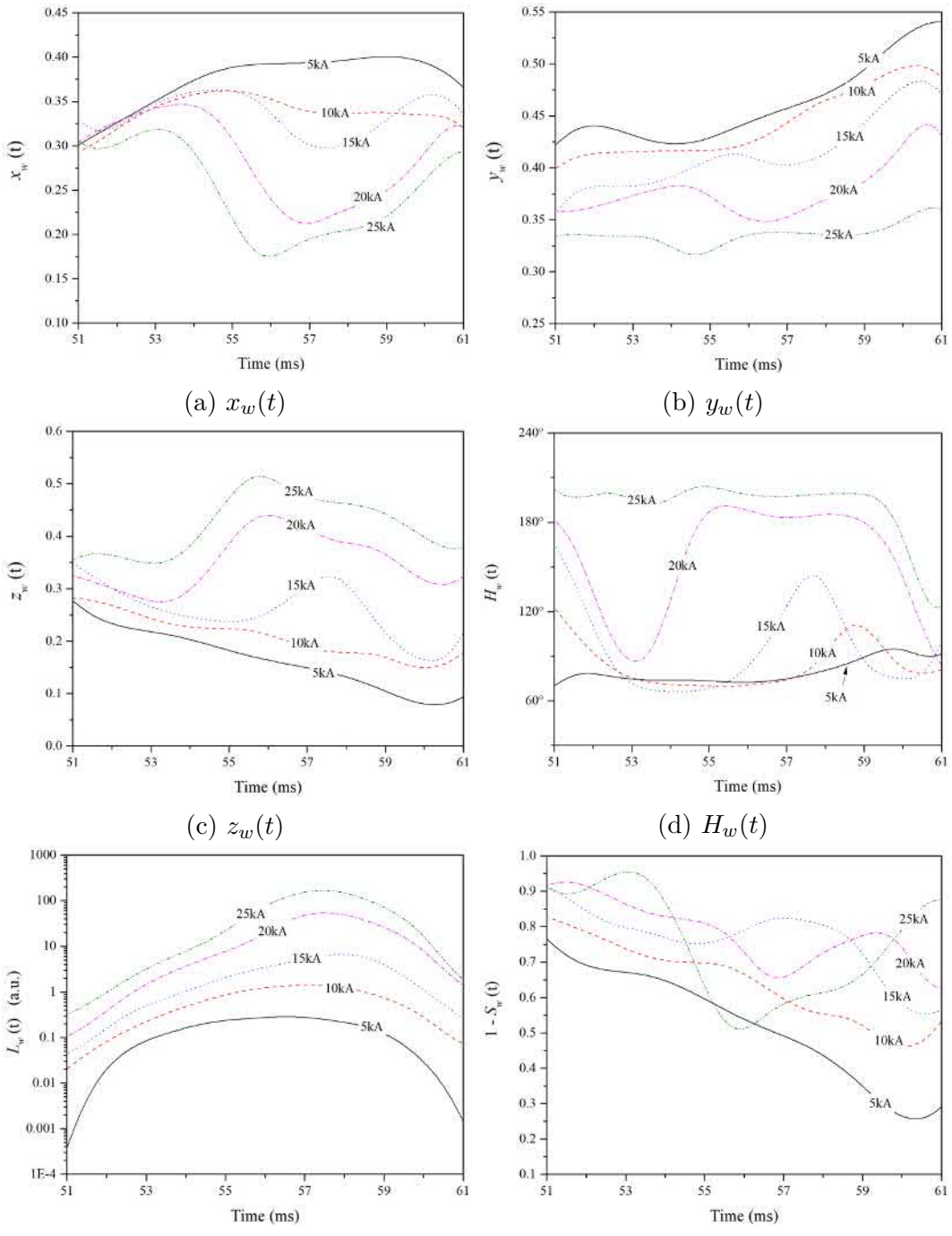

(a) $x_w(t)$ (b) $y_w(t)$

(c) $z_w(t)$ (d) $H_w(t)$

(e) $L_w(t)$ (f) 1-$S_w(t)$

Fig. 5.9 Time variation of wavelength domain chromatic parameters of Cu arcing contact in N_2.

of $H_w(t)$). As the mass loss increases, $H_{t,hw}$ moves clockwise, i.e. the peak of $H_w(t)$

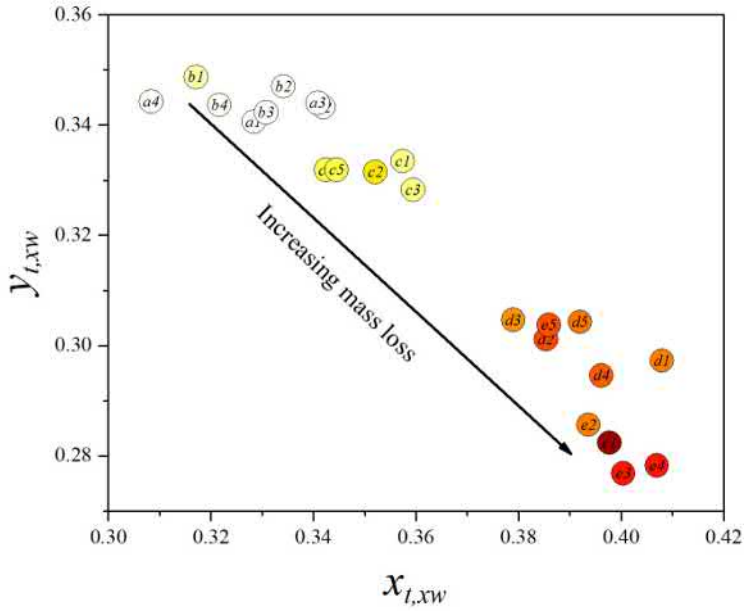

Fig. 5.10 $x_{t,xw}$ versus $y_{t,xw}$ plot of Cu arcing contact in N_2.

appears earlier. The value of $L_{t,hw}$ increases showing that the dominant wavelength shifts to the range of $B_{w,ev}$ (high value of $H_w(t)$).

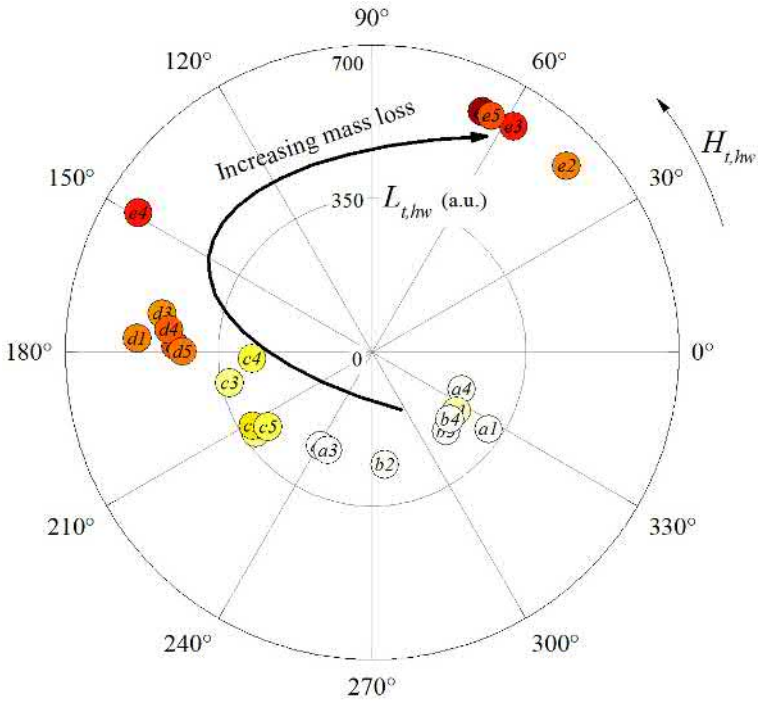

Fig. 5.11 $H_{t,hw}$ versus $L_{t,hw}$ plot of Cu arcing contact in N_2.

CuW Contact Erosion in SF_6

According to the analysis in Chapter 4, it is known that the the mass loss of CuW arcing contact at low currents is mostly determined by the arc root movement and has only a weak correlation with the wavelength domain chromatic parameters (Figure 5.7). In this section, only the time variation of arc spectra for currents higher than 15kA$_p$ are considered.

Figure 5.12 shows the time variation of the wavelength domain chromatic parameters $x_w(t)$, $y_w(t)$, $z_w(t)$, $H_w(t)$, $L_w(t)$ and 1-$S_w(t)$ for various peak current amplitudes of test set CuWSF6-S (colour scale refer to Figure 3.3).

Figure 5.12 (a) shows that, as the current (mass loss) increases, the absolute value of $x_w(t)$ decreases slightly, but it did not vary significantly over a time interval of 48-55ms. In Figure 5.12 (b), the value of $y_w(t)$ is mainly in the range between 0.42-0.51 indicating that the optical emission from the $G_{w,ev}$ band account for the largest section of entire visible wavelength range. As the current increases, $y_w(t)$ decreases. In addition, $y_w(t)$ shows a clear increasing trend with time. Figure 5.12 (c) shows that as the current increases, the value of $z_w(t)$ increases. At various currents, $z_w(t)$ shows decreasing trend over time which is the opposite to that of $y_w(t)$.

Figure 5.12 (d) shows that $H_w(t)$ stays at around 75° showing little variation for most of the arcing time. This is different from the $H_w(t)$ of Cu arc in N_2 (Figure 5.9 (d)). The cause of the difference is most likely due to the different sensor installation positions (for tests of CuN2-S is at the centre of observing window and for CuWSF-S is at the contact surface plane). Therefore, overwhelmingly strong line emission from Cu atoms (around 521nm, in the overlapping area between processors $R_{w,ev}$ and $G_{w,ev}$) was captured leading to a relatively constant value of $H_w(t)$. Figure 5.12 (e), shows that the relative intensity $L_w(t)$ of the spectra increases as the current increases, and have similar profiles to the arcing current. In Figure 5.12 (f), the nominal signal spread 1-$S_w(t)$ shows a decreasing trend over time and increases as current increases.

By applying the time domain processors (Figure 5.2 (b)) to each of the above wavelength domain chromatic parameters, the time domain chromatic parameters can be derived (Table 5.1). Using correlation analysis, it is found that the parameters $L_{t,lw}$ and 1-$S_{t,yw}$ (representing the effective spectra intensity and the nominal time domain spread of y_w, respectively) have strong linear correlation with the measured

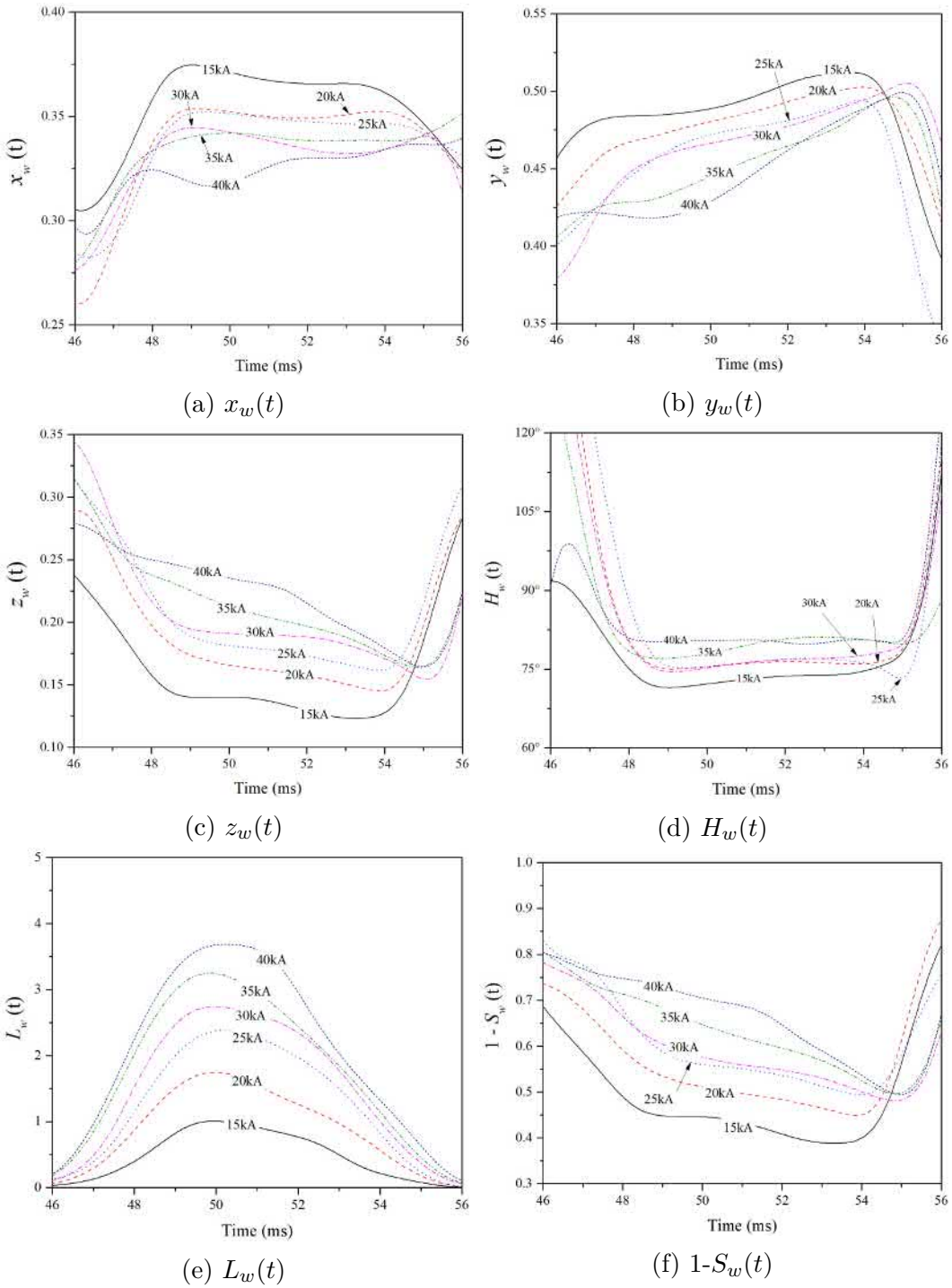

Fig. 5.12 Time variation of wavelength domain chromatic parameters of CuW arcing contact in SF_6.

mass loss of CuW arcing contact. Figure 5.13 shows that as the mass loss increases, $L_{t,lw}$ increases and 1-$S_{t,yw}$ decreases with only a small degree of scattering.

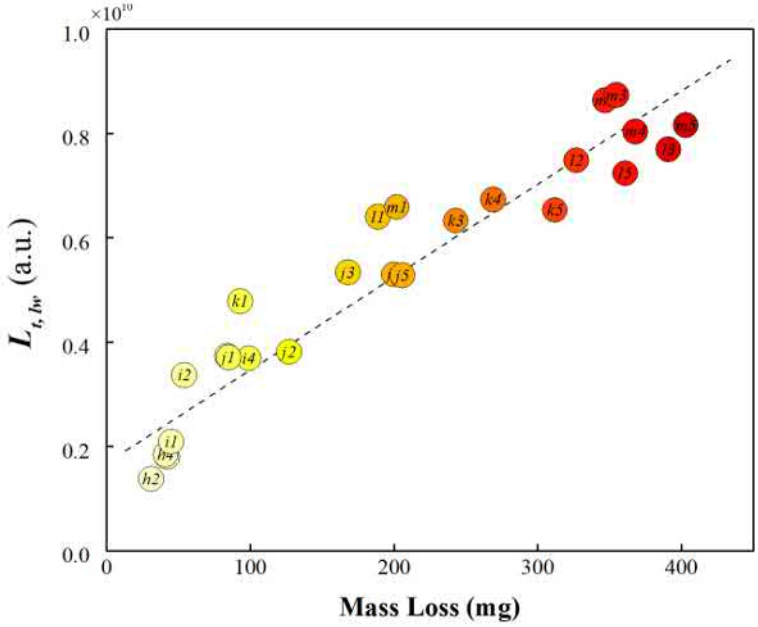

(a) $L_{t,lw}$ vs mass loss

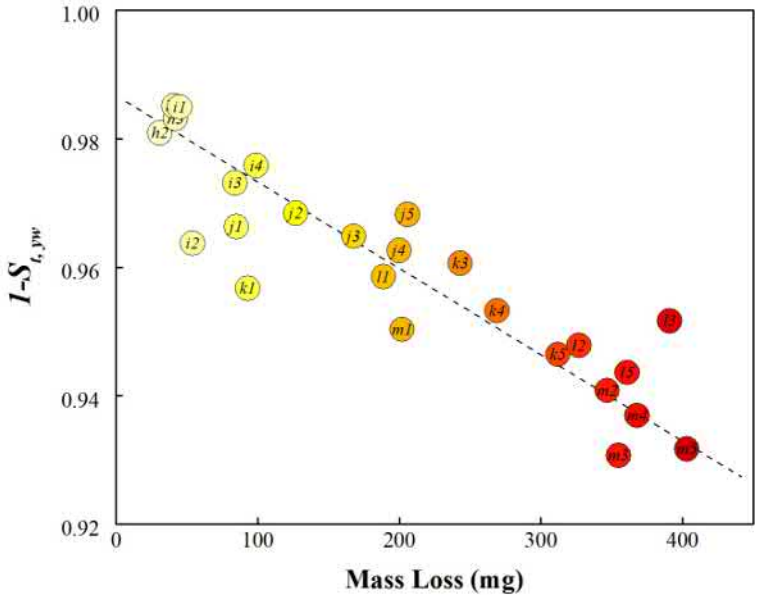

(b) 1-$S_{t,yw}$ vs mass loss

Fig. 5.13 Linear correlation between arcing contact mass loss and time domain chromatic parameters of CuW arcing contact in SF_6.

Conventionally, by using the peak current value as the predictor of the contact mass loss, large errors may be introduced at high currents (Figure 3.3) since, for example, the effect of the morphology change of the contact surface during the process of erosion was not considered. From the on-line monitoring perspective, it is required that a

precise prediction of mass loss is needed. To achieve this, the time domain chromatic parameters $L_{t,lw}$ and 1-$S_{t,yw}$ may be combined on a single map(Figure 5.14). The variation of CuW contact mass loss is clearly apparent on this map. In general, as the mass loss increases, the values of $L_{t,lw}$ increases and 1-$S_{t,yw}$ decreases. As an example, for tests at 35kA$_p$ (i.e. tests l1-l5), the position of test l1 on the graph is distinctively away from the rest of the tests at the same current amplitude (within the dash circle). A similar phenomenon is observed for tests at 40kA$_p$ (m1 is away from the gathering of m2-m5). It is indicating that, by using the time domain chromatic parameters, the essential process of contact erosion is addressed and the accuracy of prediction of contact mass loss may be improved accordingly.

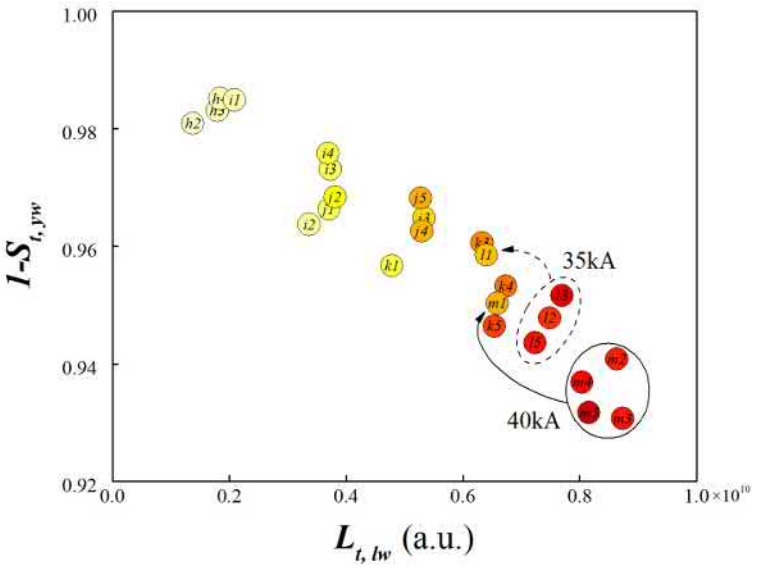

Fig. 5.14 Time domain chromatic parameters $L_{t,lw}$ versus $S_{t,yw}$ of CuW arcing contact in SF_6.

5.3 Interpretation of Chromatic Analysis Results

In this section, the prediction of mass loss of arcing contact using the square of peak current I^2_{peak} and chromatic parameters (wavelength and time domains) are interpreted and compared.

5.3.1 Wavelength Domain Parameter Analysis

For tests of Cu contact in N_2, it is found that parameters $x_w(t_p)$ and $y_w(t_p)$ both have significant linear correlation with the arcing contact mass loss and are therefore selected as predictors P_0 and P_1 (Figure 5.5 (a) and (b)). Using the linear regression technique, the regression coefficients are derived as listed in Table 5.2. Substituting the coefficients in Equation 5.2, the mass loss of Cu arcing contact can be obtained. The standard error of the estimate (SEE) may be determined by comparing with the measured mass loss (Chapter 3). The error from the chromatic results is 54.1mg which is slightly larger than the value (48.3mg) obtained using the square of the peak current I^2_{peak} as an predictor of contact mass loss.

For tests of CuW contact in SF_6, by using the chromatic graphs obtained in the previous section, the mass loss for an arcing contact can be evaluated using Linear Regression methods. Figure 5.8 indicates that the parameters $L_w(t_p)$ and 1-$S_w(t_p)$ have relatively strong linear correlation with the arcing contact mass loss. These are therefore selected as the predictors P_0 and P_1. The constant C in Equation (5.2) is excluded in this case. The derived regression coefficients are listed in Table 5.2. Substituting these coefficients into Equation 5.2 yields the predicted mass loss of CuW arcing contact and the SEE value of 51.3mg. Using the square of the peak current (I^2_{peak}) as a predictor of contact mass loss, the SEE value is 66.0mg. Thus, the wavelength domain chromatic parameters improve the accuracy of the CuW contact mass loss by 22.3%. The improvement is due to the weak effect of droplet ejection on erosion and elimination of spectral emissions from the anode region.

Table 5.2 Regression coefficients of mass loss prediction using wavelength domain chromatic parameters.

Test Code	β_0	β_1	C
CuN2-S	-1238.4 (P_0:$x_w(t_p)$)	-1211.6 (P_1:$y_w(t_p)$)	974.8
CuWSF6-S	1.26×10^{-7} (P_0:$L_w(t_p)$)	-268.5 (P_1:1-$S_w(t_p)$)	n/a

For now, the wavelength domain chromatic parameters not only improve the accuracy of mass loss prediction of arcing contact, but also contain valuable information regarding the state of the arcing system. For instance, the value of $L_w(t_p)$ represents the effective optical energy radiated from the arc column which can be regarded as an

indicator of current amplitude; the value of $H_w(t_p)$ represents the dominant wavelength which can be treated as an indicator of the onset of contact erosion etc. To summary, by using the six wavelength domain chromatic parameters, the characteristics of the spectral arc emission can be deduced, the trend of mass loss increasing can be intuitively traced on the x-y, H-S and H-L plots, and the mass loss values can be estimated using linear regression method.

5.3.2 Time Domain Parameter Analysis

The time domain chromatic parameters represent the time variation of wavelength domain chromatic parameters which is expected to be more reliable for mass loss prediction. For tests of Cu contact in N_2, it is found that $x_{t,xw}$ and $y_{t,xw}$ have a strong linear correlation with the Cu arcing contact mass loss (Figure 5.10). The time domain parameter $y_{t,xw}$ is selected as the only predictor P_0. The derived regression coefficient and the constant are listed in Table 5.3. By substituting these coefficients in Equation 5.2, the mass loss of the Cu arcing contact can be obtained and the SEE value is 40.2mg which is much improved in comparison with the SEE value of 54.1mg when using the wavelength domain parameters as predictors. By using the time domain chromatic parameter $y_{t,xw}$, the accuracy of the prediction of Cu contact mass loss is improved by 16.8% comparing with arc energy method.

For tests of CuW contact in SF_6, the time domain chromatic parameters $L_{t,lw}$ and 1-$S_{t,yw}$ are selected as the predictors of CuW contact mass loss (i.e. P_0 and P_1) and the constant C is omitted. The derived regression coefficients are listed in Table 5.3. Substituting the coefficients in Equation 5.2, the mass loss of CuW arcing contact can be obtained and the SEE value is reduced to 40.2mg. The accuracy of mass loss prediction is improved by 39.1% comparing with arc energy method.

Table 5.3 Regression coefficients of mass loss prediction using time domain chromatic parameters.

Test Code	β_0	β_1	C
CuN2-S	-5502.4 (P_0:$y_{t,xw}$)	n/a	1910.6
CuWSF6-S	5.25×10^{-8} (P_0:$L_{t,lw}$)	-85.47 (P_1:1-$S_{t,yw}$)	n/a

5.3.3 Analysis of Accuracy of Mass Loss Prediction

Table 5.4 compares the the SEE values of mass loss prediction using different predictors (i.e. the square of peak current, the wavelength domain chromatic parameters and the time domain chromatic parameters).

Table 5.4 Comparison of Standard Error of Estimate (SEE) of Mass Loss Prediction using Various Predictors.

Predictor	CuN2-S	CuWSF6-S
I^2_{peak}	48.3mg	66.0mg
Wavelength Domain Parameters	54.1mg	51.3mg
Time Domain Parameters	40.2mg	40.2mg

For Cu arcing contact in N_2, the SEE value of mass loss prediction using I^2_{peak} is 48.3mg and increases to 54.1mg when using the selected wavelength domain chromatic parameters ($x_w(t_p)$ and $y_w(t_p)$). In this case, the lower accuracy of the prediction using the wavelength domain chromatic parameters is probably due to three reasons. First, the melting and boiling temperature of copper are relatively low so that molten droplet ejection is expected to be severe during the period of arcing. Overall the amount of mass loss caused by molten droplet ejection (the portion which is not vaporized in the arc column) can be significant which is not effectively represented by the arc spectra. Second, the install position of the optical sensor is at the centre of the observing window (Figure 2.6), thus the spectral emission from the anode (tulip contact) region is superimposed upon that of cathode (plug contact) which will inevitably result in larger errors especially at high currents. Third, since the arc current is sinusoidal, the arc spectra are always mid transient without reaching a steady state. The analysis of the arc spectra at a specific moment overlooks information which might exist in the time domain.

For CuW arcing contact in SF_6, the SEE value of mass loss prediction using I^2_{peak} is 66.0mg and decreases to 51.3mg when using the selected wavelength domain chromatic parameters ($L_w(t_p)$ and 1-$S_w(t_p)$).

5.4 Study of CuW Arcing Contact Erosion with a Nozzle

In many HVCBs the arcing environment can be complicated by the use of gas flow controlled by a PTFE nozzle within which the arc and contacts may be located. There is then the added complication of monitoring the optical emissions in the presence of the moving nozzle. To address this issue, tests were first performed to check the chromatic time domain variations for the arc spectra with the nozzle moving followed by the chromatic wavelength domain analysis at a selected time.

5.4.1 Time Variation of Chromatic Wavelength Domain Parameters

Figure 5.15 shows the time variation of wavelength domain chromatic parameters $x_w(t)$, $y_w(t)$, $z_w(t)$, $H_w(t)$, $L_w(t)$ and 1-$S_w(t)$ at various current amplitudes of test sets CuWSF6-G. The vertical dash line in each graph represents the selected time for wavelength domain processing which is identical for all chromatic parameters at different currents.

Due to the existence and the movement of the PTFE nozzle, the characteristics of the captured arc spectra are significantly affected. For example, it is found that the fluctuations of these six wavelength domain chromatic parameters are relatively high at the middle time of the arc (∼51ms). This is ascribed to the nozzle. During the first half time of the arc, the spectral emission of the arc is largely absorbed by the PTFE nozzle (which is located in the gap between the arcing contact and the optical sensors) before reaching the optical sensors. As the driving mechanism drives the nozzle (attached to the moving arcing contact) away from the stationary contact, the thickness of the nozzle wall blocked in between the arc root and the optical sensor becomes thinner (refer to Figure 2.3 (c) and (d)). Therefore, the influence of the nozzle on the captured spectra is reduced showing a rapid change of the wavelength chromatic parameters over time.

Figure 5.15 (a) shows the time variation of $x_w(t)$ at various peak currents. It can be seen that the curve at 4.5kA is substantially different from the curves for the other two

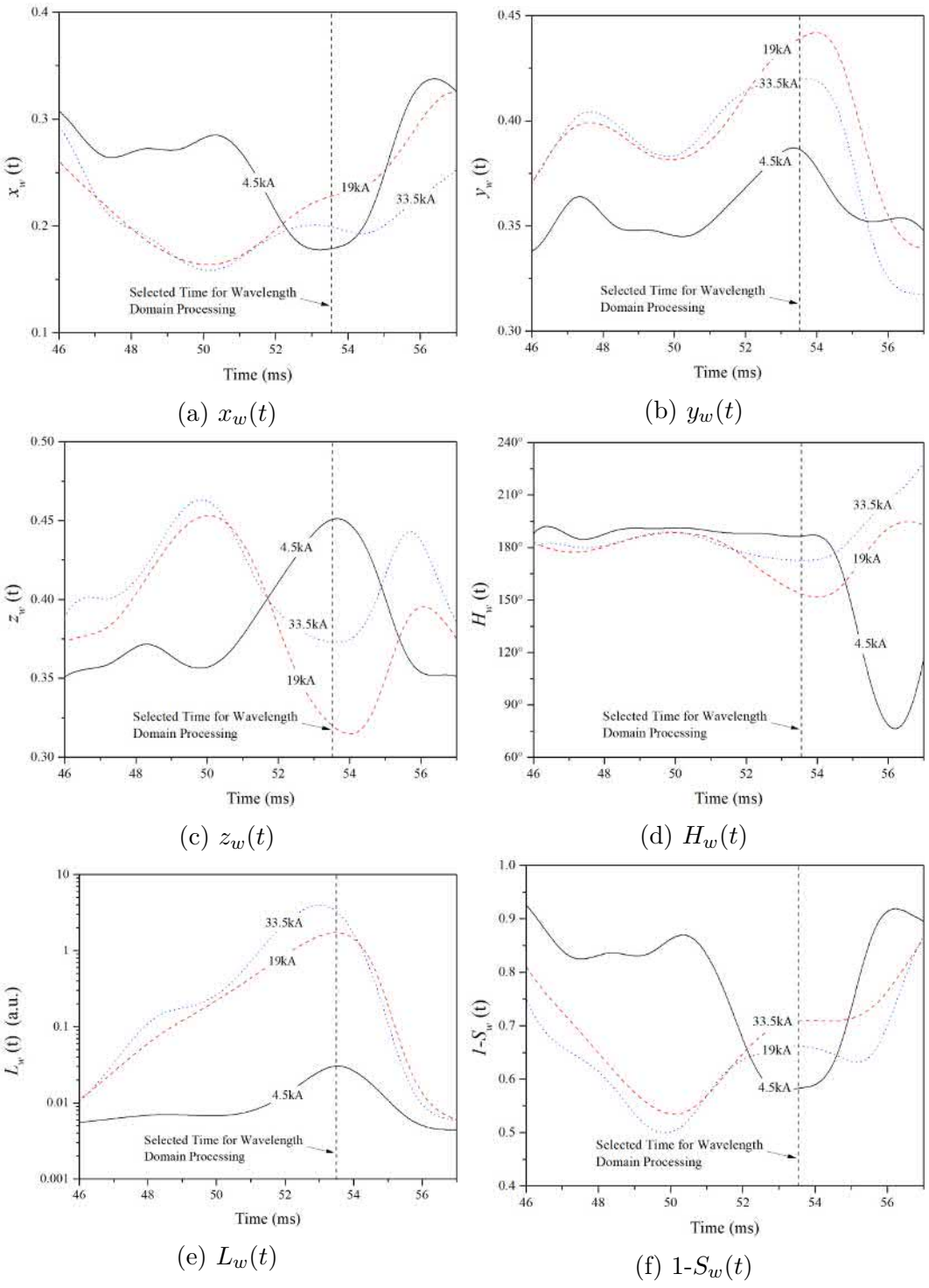

(a) $x_w(t)$ (b) $y_w(t)$

(c) $z_w(t)$ (d) $H_w(t)$

(e) $L_w(t)$ (f) 1-$S_w(t)$

Fig. 5.15 Time variation of wavelength domain chromatic parameters of CuW arcing contact in SF_6 subjected to gas blast.

currents 19 and 33.5kA. This indicates that the erosion process at low current is not the same as those at high currents. This phenomenon is consistent with the case without having the nozzle installed (i.e. test set CuWSF6-S, Figure 5.7). Figure 5.15 (b) shows the time variation of $y_w(t)$ which represents the relative amplitudes of emission from Cu atoms as the processor $G_{w,ev}$ covers the strong Cu atom lines. From the amplitudes of the curves, it can be deduced that the Cu vapour at 19 and 33.5kA are much higher than at 4.5kA. Figure 5.15 (c) shows the time variation of $z_w(t)$ which represents the relative emission from the wavelength range of processor $B_{w,ev}$.

Figure 5.15 (d) to (f) show the time variation of $H_w(t)$, $L_w(t)$ and 1-$S_w(t)$, respectively. $H_w(t)$ keeps stable during the first half of the time interval and changes during the second half indicating that the captured spectra varies significantly. Due to the existence of the nozzle, the peak value of $L_w(t)$ does not appear at the moment of peak current. Unlike the case without nozzle, the effective intensity of the arc is an important factor used for predicting the mass loss, the value of $L_w(t)$ does not vary significantly at high currents (19 and 33.5kA).

By applying the time domain chromatic processors (Figure 5.2 (b)) to each of the wavelength domain chromatic parameters (i.e. $x_w(t)$, $y_w(t)$, $z_w(t)$, $H_w(t)$, $L_w(t)$ and 1-$S_w(t)$), the values of the time domain chromatic parameters $x_{t,xw}$ and $y_{t,xw}$ can be derived. This result is shown in Figure 5.16 (colour scale refers to Figure 3.6). This shows that the data points of the same current amplitudes gathers together with small scattering.

Since the average mass loss value is used for the tests of CuW contact erosion in SF_6 subjected to gas blast, the prediction of contact mass loss using the Linear Regression technique is no longer appropriate. This can be solved in the future when individual mass loss values are obtained.

5.4.2 Chromatic Wavelength Domain Results at Selected Moment

The characteristic of arc spectra in wavelength domain at the selected moment (denoted by the vertical dash line in Figure 5.15) have also been briefly investigated.

Figure 5.17 shows the variation of wavelength domain chromatic parameters $x_w(t_p)$ and $y_w(t_p)$. The colour of each point represents the average mass loss according to

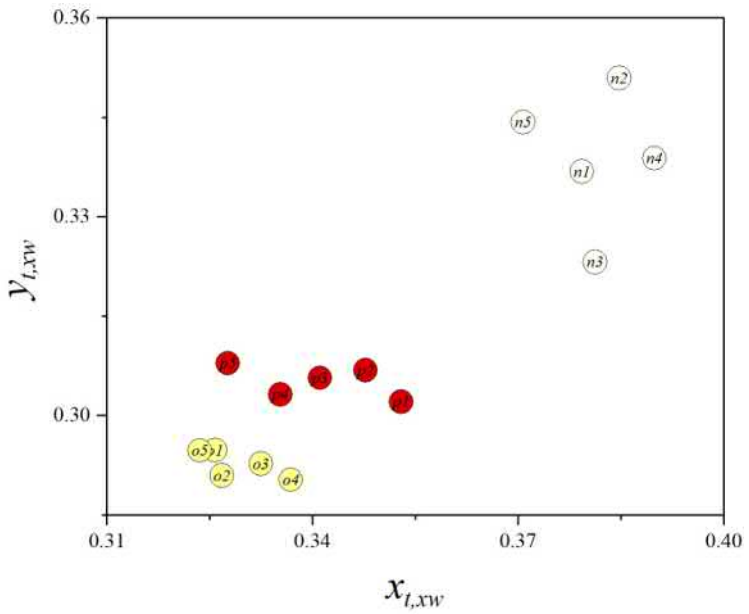

Fig. 5.16 Time domain chromatic parameters $x_{t,xw}$ versus $y_{t,xw}$ of CuW arcing contact in SF_6 subjected to gas flow.

the colour bar of Figure 3.6. The value of $x_w(t_p)$ is between 0.17 and 0.25 indicating the spectral emission from the $R_{w,ev}$ band is less significant. By contrast, the value of $y_w(t_p)$ is between 0.33 to 0.45 indicating that the emission from the $G_{w,ev}$ band is prominent (which mainly consist of line emission from Cu atoms). For low mass loss tests, the $y_w(t_p)$ value is significantly less than the value for high mass loss (dash line ellipse). This is mainly due to the weak emission from the copper atoms (see Figure 3.30 (a) and (b)). At high currents, an increasing trend is observed of both $x_w(t_p)$ and $y_w(t_p)$ as the mass loss increases.

Figure 5.18 shows the variation of wavelength domain chromatic parameters $H_w(t_p)$, $L_w(t_p)$ and 1-$S_w(t_p)$. The solid arrow represents the direction of mass loss increasing. As the mass loss increases, the value of $L_w(t_p)$ increases indicating that the total optical energy received by the sensors increased. The value of $H_w(t_p)$ decreases from 200° to 150° implying that the dominant wavelength shifted from the centre of processor $B_{w,ev}$ (i.e. 240°) to the centre of processor $G_{w,ev}$ (i.e. 120°). Since processor $G_{w,ev}$ covers the spectral lines of Cu atoms, the decreasing of $H_w(t_p)$ relates to the increasing of relative emission from Cu atoms. The value of 1-$S_w(t_p)$ increases along with the increasing mass loss.

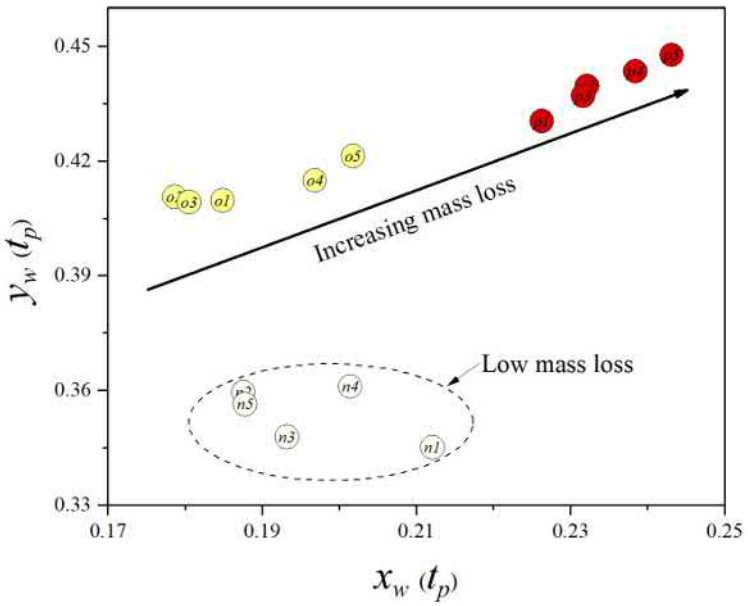

Fig. 5.17 Erosion trend of CuW arcing contact in SF_6 subjected to gas blast represented on a $x_w(t_p)$ versus $y_w(t_p)$ chromatic map.

For the experiments with the PTFE nozzle, the results relate not only to the effect of emissions from the arc contact but also the ablation of the PTFE nozzle material. Figures 5.17 and 5.18 indicate that none the less an indication of contact mass loss may still be possible. Also the chromatic spectral approaches may also contain important information about nozzle wear due to ablation. Further work will be needed to explore such a possibility.

5.5 Summary

In this chapter, the time-resolved arc spectra are processed using chromatic methods in various data domains (i.e. wavelength and time). The correlations between the arcing contact mass loss and the chromatic parameters have been investigated. The limitation of utilizing conventional OES methods for spectral analysis has been avoided. The main conclusions are as follows:

(1) Wavelength domain chromatic parameters of the arc spectra show good correlation with the mass loss of an arcing contact. The arc spectra at the peak current time are processed in the wavelength domain using chromatic methods. It has been found that selected wavelength domain chromatic parameters reflect certain characteristics of

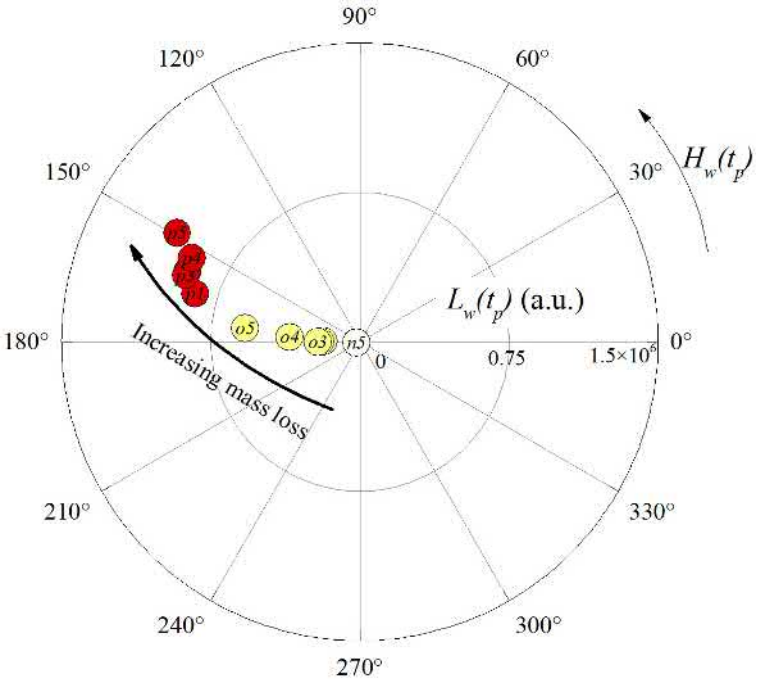

(a) H-L

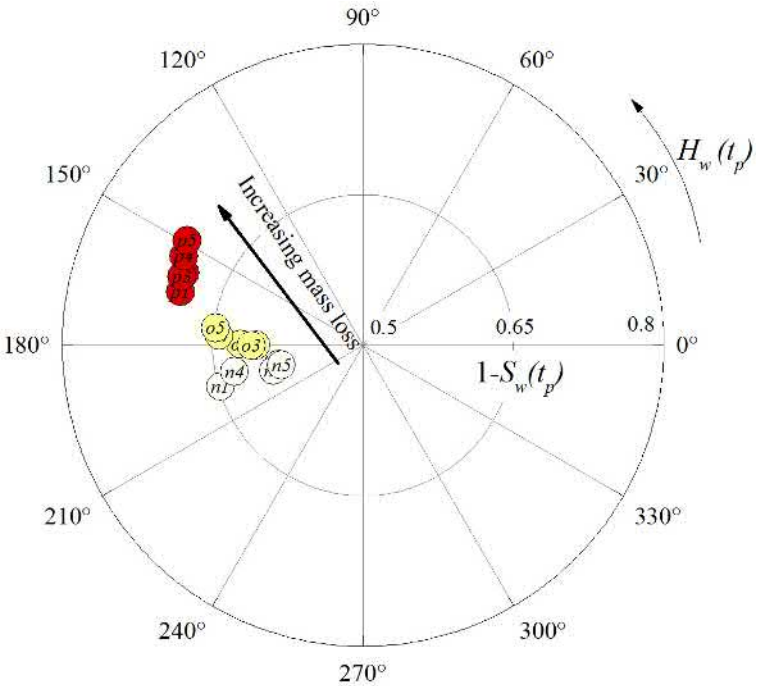

(b) H-(1-S)

Fig. 5.18 Chromatic polar maps for erosion trend of CuW arcing contact in SF_6 subjected to gas blast.

the arc spectra which are directly related to the interaction between the arc and arcing contact. For instance, when the spectra of the arc column are captured, the dominant wavelength $H_w(t_p)$ distinguishes the tests of high mass loss from the low mass loss ones for a Cu arcing contact; when the spectra of the arc root region are captured, it has been found that the effective strength of the arc spectra $L_w(t_p)$ generally increase with the mass loss of the CuW arcing contact.

(2) Time domain (secondary) chromatic parameters have improved features for prediction of arcing contact mass loss which is suitable for on-line monitoring of arcing contact erosion. The time variations of the arc spectra have been investigated using time domain chromatic processing methods. The derived time domain chromatic parameters show strong linear correlation with the mass loss of an arcing contact. Mathematical expressions have been obtained for the prediction of arcing contact mass loss for Cu contacts in N_2 and CuW contacts in SF_6 and for arc currents up to $40kA_p$. The accuracy of prediction of CuW contact mass loss at high currents using time domain chromatic parameters (SEE value 40.2mg) is improved by 39.1% compared with the conventional method of using the arc energy method (SEE value 66.0mg).

(3) Preliminary results have been presented for applying the chromatic spectral monitoring to CuW arc contacts in SF_6 in the presence of a PTFE gas flow controlling nozzle. Although the PTFE of the nozzle affects the spectral signatures, an indication of the mass loss with wavelength domain chromaticity remains possible. However further investigations are needed to confirm such possibilities.

Chapter 6

3D Thermal Model of CuW Contact Erosion Considering the Effect of Arc Root Movement

In the published arcing contact erosion models of HVCB, the shape of the arc root was always assumed to be axially symmetrical and the movement of the arc root was neglected. In this chapter, a 3D thermal model of the plug arcing contact is proposed using the commercial simulation package COMSOL Multiphysics[89], considering the effect of arc root movement on the contact surface. The contact temperature distribution and its time variation, the mass loss of plug contact and the geometry deformation for different peak currents of CuW contact are simulated. The results are compared with experimental data.

6.1 The Micro-process of Arc-Contact Interaction

The electrical-arc discharge is an inevitable phenomenon during the current breaking process in a HVCB, and the arcing contacts are the components directly interacting with the arc. The interaction between the arc and arcing contacts can be roughly divided into four stages[90]:

(1) Liquid metal bridge stage. At the moment of arcing contacts separation, the temperature of the last contacting point is between the melting point and the boiling point of the contact material.

(2) Liquid metal bridge rupture stage. As the spacing of the arcing contacts increases, the liquid metal bridge will eventually rupture and release high pressure metal vapour into the contact gap.

(3) Metal vapour expansion stage. Due to the presence of a pressure gradient, the metal vapour spreads rapidly between the contacts.

(4) Gaseous arc formation. With the injection of arc energy, the metal vapour and the insulating gas in the contact gap are ionized and the gaseous arc is finally formed.

The gaseous arc discharge can be divided into three regions: the cathode region, the arc column and the anode region, as shown in Figure 6.1.

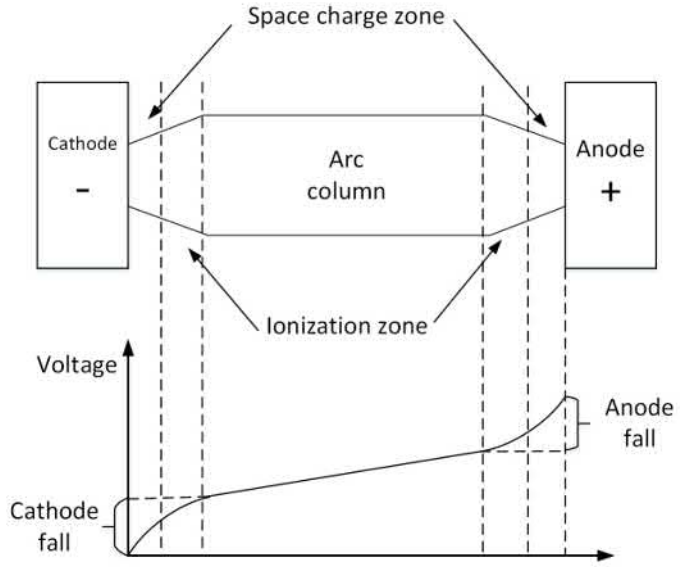

Fig. 6.1 Schematic of an arc and the corresponding voltage distribution[90].

The conductive mechanism of the arc is that the cathode emits electrons relying on field-induced electron emission and thermo-electron emission effects; the arc columns generates free electrons and the positive ions relying on the collisions from the thermal motion of particles, which is called thermal ionization; the anode collects electrons and has only a small impact on the arcing process. In the arc column, in contrast to the

thermal ionization, electrons and positive ions are compounded into neutral particles or diffused outside the arc column which is known as de-ionization. In a stable arc, the rate of ionization equals to the de-ionization rate, forming the ionization equilibrium. The equilibrium state of the column can be described by the Saha equations.

The cathode region of the arc and the interface of the cathode and the arc are shown in Figure 6.2. The cathode contact provides the electrons, and once the electron emission stops, the arc will extinguish. In the cathode region, the electric field intensity and the temperature gradient are usually very high, and the current density is higher than that of the arc column. Especially at high currents, plasma jets will form in this region (Chapter4). The region adjacent to the contact surface is the space charge zone with a spatial scale of several microns. In this region, the electron density is greater than the positive ion density, and there is a large potential gradient. The second region is the ionization zone, where the electron density and the positive ion density are approximately equal.

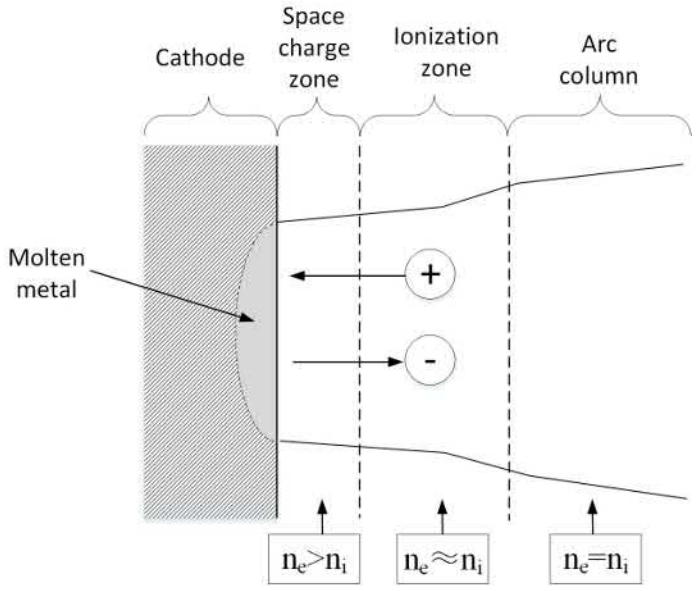

Fig. 6.2 Cathode region of the arc.

6.2 Thermal Modelling

To simulate the effect of the arc root movement on the erosion process of an arcing contact, a 3D thermal model is proposed. The computational domain and boundary conditions are shown in Figure 6.3.

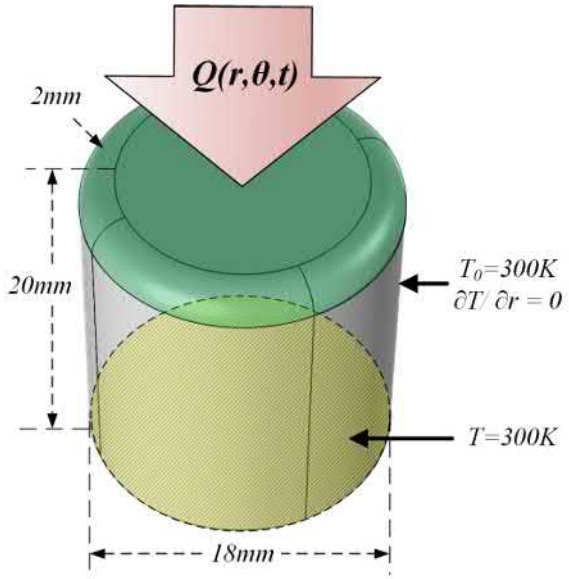

Fig. 6.3 Computational domain and boundary conditions of the thermal model of contact erosion.

The diameter of the plug contact is 18mm, the length is 20mm and there is 2mm round chamfer on the edge of the top contact surface as in practice. The arc column domain is omitted in this model and the holistic heating effect of the arc at the contact surface is treated as a surface heating source $Q(r, \theta, t)$ (as a function of the position on the contact surface (r, θ) and the time t). The current of the arc $i(t)$ is alternating at a frequency of 50Hz and lasts for a half cycle (10ms) which can be given as

$$i(t) = I_{max} \cdot sin(2\pi \cdot 50 \cdot t) \qquad 0 \leq t \leq 10ms \tag{6.1}$$

where I_{max} is the peak current (unit: A). Due to the high conductivity of the contact material and the short duration of arc, the Joule's heating effect in the contact and the heat exchange with surrounding gas are neglected[30]. The initial temperature of the plug contact is T_0 =300K and the temperature of the cool end remains at 300K during the arc.

6.2.1 Governing Equations

The arc-cathode interaction is a complicated physical-chemical phenomenon. The temperature distribution of the arcing contact can be derived by solving the heat transfer equation. The differential form of the energy equation for a general heat transfer problem is shown as follows[91]:

$$\rho C_p \frac{\partial T}{\partial t} = \nabla \cdot (k \nabla T) + Q \tag{6.2}$$

where:

ρ — mass density of contact material, unit: kg/m^3;

C_p — heat capacity of contact material, unit: J/K;

T — temperature, unit: K;

k — heat conductivity of contact material, unit: W/(m $\cdot$ K);

Q — heat source term, unit: W/m^2.

The part on the left side of Equation (6.2) is the time term and the first term on the right side is the thermal conduction term. The heat source term Q is determined by the energy balance at the contact surface which shall be discussed later in detail.

Mass loss may be caused as the boiling temperature of the arcing contact material is reached. The rate of mass loss caused by vaporization can be calculated by the following equation[20]:

$$\dot{m} = \frac{q_{vap}}{h_{vap}} \tag{6.3}$$

where:

$\dot{m}$ — the mass loss rate of vaporization, unit: kg/(m^2 $\cdot$ s);

q_{vap} — the energy flux available for contact vaporization, unit: W/m^2;

h_{vap} — the latent heat of contact material vaporization, unit: J/kg.

The total mass loss of a single test can be obtained by integrating $\dot{m}$ over the contact surface area S and the arcing time t_{arc}:

$$\triangle m = \int_0^{t_{arc}} \int_0^S \dot{m}\, dS\, dt \tag{6.4}$$

6.2.2 Energy Balance at the Contact Surface

The energy balance at the cathode surface is very complex and has been studied by Ecker[26], Donaldson[34] and Slade[90] in detail. Among the components that supply energy are:

(1) Bombardment of positive ions and neutral atoms on cathode surface;
(2) The kinetic energy gained by the positive ions from cathode fall region;
(3) Condensation of positive ions and neutral atoms on cathode surface;
(4) Radiation energy from arc column;
(5) Chemical reaction energy on cathode surface;

Meanwhile, among the components that cause energy loss are:

(1) Energy of electron emission;
(2) Vaporization of cathode material;
(3) Liquid droplet ejection;
(4) Radiation from cathode surface;
(5) Dissociation of gas molecular at contact surface;
(6) Heat conduction into cathode;

However, due to the lack of experimental data, most of the above energy input and output mechanisms of the arc column can not be calculated separately. At the top contact surface, a simple equivalent voltage approach is used to treat the holistic heat effects of all energy mechanisms. The effective energy input from the arc q_{arc} (unit: W/m^2) can be calculated as following:

$$q_{arc} = U_{eff} \cdot j \tag{6.5}$$

where:

U_{eff} — effective voltage drop, unit: V;

j — current density, unit: A/m^2.

The value of the effective voltage drop at the cathode region was found to be in the range of 5.4-11.2V[30, 91, 92] and the value $U_{eff} = 10$V is used in this study.

The heat conduction into the contact q_{cond} (unit: W/m^2) can be calculated as following:

$$q_{cond} = k \cdot \nabla T \tag{6.6}$$

From the above explanation, the power balance at the contact surface can be given

$$q_{vap} = q_{arc} - q_{cond}. \tag{6.7}$$

With Equation (6.3), (6.4), (6.5), (6.6) and (6.7), the mass loss of the arcing contact can be derived. The heat source term Q at the contact surface in Equation 6.2 equals to the effective energy input from the arc q_{arc} minus the energy used for contact vaporization q_{vap}.

6.2.3 Treatment of the Arc Root

The energy of the arc is transferred to the arcing contact via the arc root attachment region on the contact surface. To consider the effects of arc root movement on the arcing contact erosion, the following simplifications have been made:

(1) It is assumed that the shape of the arc root is circular. In practice, the attachment region of the arc on the contact surface is in the form of a large number of small cathode spots. To simplify the description, the effect of these cathode spots on the contact surface is equivalent to a circular arc root which is widely accepted in theoretical investigations[21, 38], and the circular shape of the arc root is also confirmed in Section 3.4.1.

(2) It is assumed that the arc root moves circularly on the contact surface. From the captured high-speed photographies of the arc root, the angular velocity of the arc root (ω) is estimated as 400rad/s. Therefore, the angular coordinate of the arc root centre ($\theta_{root,0}$) is the product of the angular velocity ($\omega = 400\pi$rad/s) and time (t).

(3) The arc root is assumed to be tangential to the edge of the contact surface at all times. In other researchers' models, the arc was always assumed to be axially symmetrical and fixed at the centre of the arcing contact[38, 92]. However, based on the analysis in Chapter 4, it is known that the arc root tended to occupy the

edge area of the contact surface instead of locating at the centre (Figure 3.7). The radial coordinate of the arc root centre ($R_{root,0}$) is the difference between the plug contact radius $R_{contact}$ and the arc root radius R_{root} (the centre of the contact is the origin point).

Based on the above assumptions, the size of the arc root can be uniquely determined by its radius R_{root} which can be calculated as following:

$$R_{root} = \sqrt{\frac{i}{\pi \cdot J_{mean}}} \tag{6.8}$$

where:

J_{mean} — average current density of the arc root, unit: A/m^2.

The average current density J_{mean} of the arc root is approximately a material specific constant in the range between 1×10^7A/m^2 to 2×10^8A/m^2[7, 21, 28]. In this work, the value of average current density is assumed to be 1×10^8A/m^2. Once the calculated radius of the arc root R_{root} is greater than the radius of the plug contact $R_{contact}$ (9mm), then the value of $R_{arc} = 9$mm is used. Therefore, the average current density J_{mean} increases accordingly.

Inside the arc root area, the distribution of the current density is assumed to be Gaussian[93, 94] which can be written as following:

$$j = J_{max} \cdot exp\left(-\frac{r^2}{2 \cdot \sigma^2}\right) \tag{6.9}$$

where:

J_{max} — the maximum current density at the centre of the arc root, unit: A/m^2;

r — the radial position from the centre of the arc root, unit: m;

σ — the standard deviation of Gaussian distribution which determines the width of current distribution, in this work the value of $\sigma = 1.5R_{root}$ is used.

The area integral of the current density inside the arc root equals the instantaneous current value:

$$\int_0^{R_{root}} j \cdot 2\pi r \, dr = i. \tag{6.10}$$

Substitute Equations (6.8) and (6.9) into Equations (6.10), it can be derived that $J_{max} = 1.665 J_{mean}$. For a given location on the contact surface (x, y), the effective

energy input from the arc q_{arc} can be expressed as following:

$$q_{arc} = 1.665\, U_{eff}\, J_{mean} \cdot exp\left(-\frac{(x-x_0)^2 + (y-y_0)^2}{2 \cdot (1.5R_{root})^2}\right) \tag{6.11}$$

where x_0 and y_0 are the coordinates of the arc root centre which can be derived via the following equations

$$\begin{aligned} x_0 &= (R_{contact} - R_{root})\, cos(\omega t), \\ y_0 &= (R_{contact} - R_{root})\, sin(\omega t). \end{aligned} \tag{6.12}$$

6.2.4 Treatment of Material Removal

The CuW contact material is a pseudo alloy, which is also called metal sweating materials and manufactured using the sintered techniques[95]. Cu and W are not mutually soluble matter in neither solid nor liquid states, and there is no chemical reaction which occurs between these two materials.

From the microscopic, metal copper (low melting temperature) is fixed in the skeleton of tungsten (high melting temperature)[30, 96] where copper and tungsten both maintain their own physical and mechanical properties, so that CuW retain not only the high conductivity of copper, but also the anti-ablation property of tungsten.

During the erosion process, as the temperature increases, there are four different mixed states of copper and tungsten as shown in Figure 6.4:

(1) solid copper and solid tungsten;
(2) liquid copper and solid tungsten;
(3) vapour copper and solid tungsten;
(4) vapour copper and liquid tungsten.

At room temperature, both copper and tungsten are in the solid state. Subjected to the heating effect of the arc, the melting and boiling temperatures of copper are reached successively while the skeleton of tungsten is still in a solid state. Therefore, the liquid and gaseous copper will be locked in the tungsten skeleton and can not escape from the arcing contact surface. As the temperature further increases, metal tungsten reaches its melting point and the original material skeleton fails. Consequently, copper vapour begins to escape from the molten contact surface.

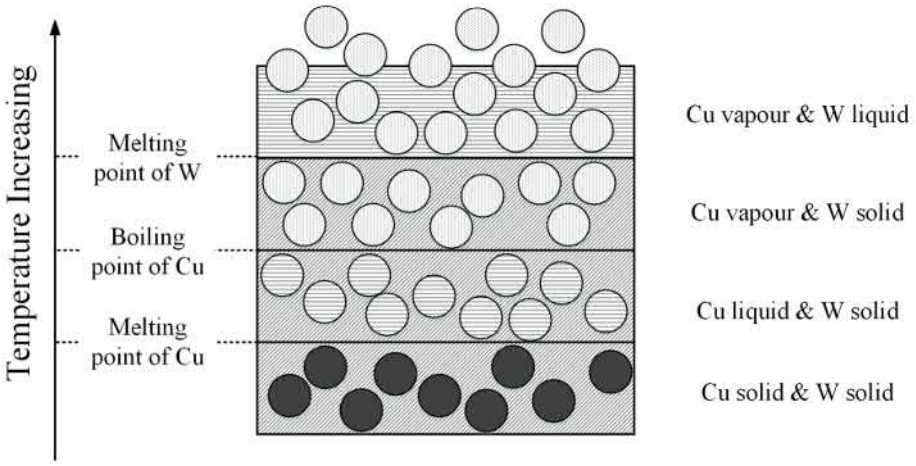

Fig. 6.4 Schematic diagram of layered structure of CuW contact surface along with temperature increase.

Generally, vaporization and molten droplet ejection of CuW material may both take place at the arcing contact surface under the heating effect of the arc. In this model, the ejection of molten droplets is not considered and it is assumed that there is no mass loss before the temperature of the contact surface reaches the melting point of tungsten. Once the melting temperature of tungsten is reached, only the copper vapour escapes while the molten tungsten remains on the contact surface.

In the use of Equation (6.7) to calculate the mass loss of a contact $\dot{m}$, h_{vap} should be brought into the vaporization latent heat of copper $h_{v,Cu}$. The melting latent heat of copper $h_{f,Cu}$ and tungsten $h_{f,W}$ shall be considered in the form of equivalent heat capacity in the erosion model.

The density of CuW ρ_{comp} can be calculated using the law of mixture[97]:

$$\rho_{comp} = \frac{\rho_W \cdot \rho_{Cu}}{\rho_W W_{Cu} + \rho_{Cu} W_W} \tag{6.13}$$

where:

ρ_W — density of tungsten, unit: kg/m^3;

ρ_{Cu} — density of copper, unit: kg/m^3;

W_W — weight percentage of tungsten, W_W=0.8;

W_{Cu} — weight percentage of copper, W_{Cu}=0.2.

The heat capacity of CuW C_{comp} can be calculated using the law of mixture[97]:

$$C_{comp} = W_{Cu}C_{Cu} + W_W C_W \tag{6.14}$$

where:

C_{Cu} — heat capacity of tungsten, unit: $\mathrm{J/(kg \cdot K)}$;

C_W — heat capacity of copper, unit: $\mathrm{J/(kg \cdot K)}$.

The heat conductivity of CuW Q_{comp} can be calculated using the model proposed by German[98]:

$$k_{comp} = \pi R^2 k_{Cu} + (1-2R)^2 k_W + \frac{k_W k_{Cu}(4R - 4R^2 - \pi R^2)}{3/2Rk_W + (1-3/2R)k_{Cu}} \tag{6.15}$$

where:

k_W — heat conductivity of tungsten, unit: $\mathrm{W/(m \cdot K)}$;

k_{Cu} — heat conductivity of copper, unit: $\mathrm{W/(m \cdot K)}$;

R — constant which can be calculated by equation (6.16).

$$R = 0.0113 + 1.58V_{Cu} - 1.83V_{Cu}^{3/2} + 1.06V_{Cu}^3 \tag{6.16}$$

where:

V_W — volume percentage of tungsten, can be calculated using W_W and ρ_W;

V_{Cu} — volume percentage of copper, can be calculated using W_{Cu} and ρ_{Cu}.

The variations of contact material properties, such as density, thermal conductivity and heat capacity, over temperature are neglected.

6.2.5 Treatment of Deformation of the Contact Surface

The deformation of a plug contact surface is simulated by using the "Deformed Geometry" module of COMSOL Multiphysics. It is assumed there is no horizontal flow on the contact surface, only the deformation in the vertical directly is considered.

The deformation of the contact surface is caused by the mass loss and only the vaporization of copper is taken into account. Therefore, the vertical velocity of the mesh in the z direction can be written as $u_z = \dot{m}/\rho_{Cu}$ (unit: m/s).

6.3 Results and Discussions

Simulation has been conducted at various peak current I_{max} from 5kA to 40kA using the commercial package of COMSOL Multiphysics. The temperature distribution of the arcing contact was calculated using the Heat Transfer in Solids module and deformation of the contact surface was obtained using the Deformed Geometry module.

6.3.1 Temperature Distribution of Contact Surface

Figure 6.5 to 6.7 show the time variation of arcing contact surface temperature at 5kA$_p$, 20kA$_p$ and 40kA$_p$, respectively.

As shown in Figure 6.5, at 5kA$_p$, the temperature rise on the edge of the arcing contact surface is more pronounced since the arc root is relatively small and always tangential to the edge of the contact. By contrast, the centre of the contact surface is not significantly affected during the arcing process as the temperature is low. The movement of the arc has greatly reduced the heating effect at fixed locations leading to a maximum temperature of approximately 3070K which does not reached the melting point of tungsten. Ideally, the copper is still restricted in the skeleton of tungsten, thus there is no mass loss is expected.

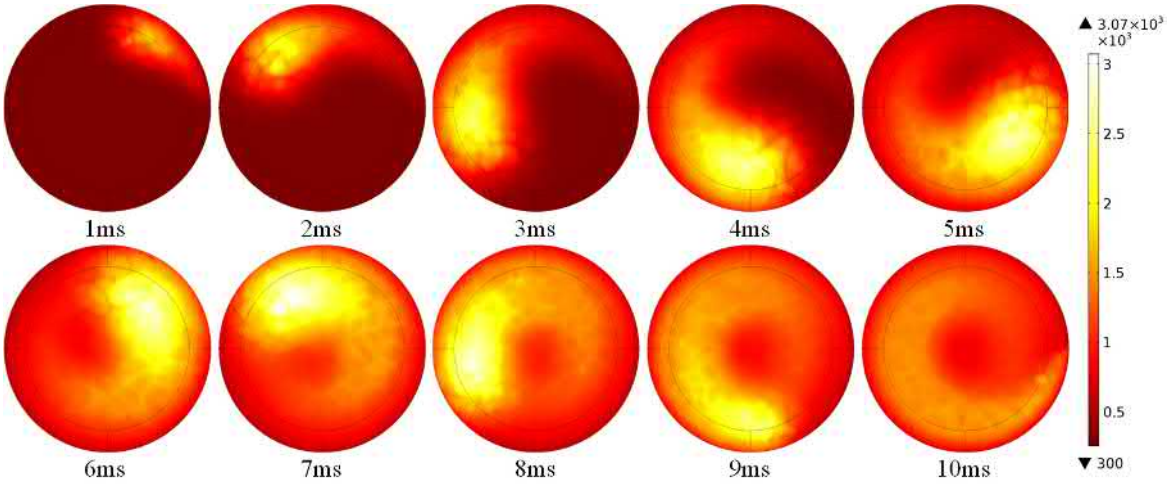

Fig. 6.5 Time variation of surface temperature of CuW contact at 5kA$_p$.

At 20kA$_p$ (Figure 6.6), the temperature rise of the contact surface is intensified in two aspects. Firstly, as the current increases, the radius of the arc root increases

resulting in that the centre of the arc root is close to the centre of the contact. The heating effect for the contact centre is more pronounced than for the edge area which is opposite to the situation at 5kA$_p$. The maximum temperature appears at the central area of the contact surface for the time interval 4ms to 9ms. Secondly, as the radius of the arc root increases, the movement of the arc root reduces. The continuous heating of the central area of the contact surface is enhanced so that the melting temperature of tungsten is reached. For times longer than 3ms, vaporization of copper starts to take place in the area and reaches the melting point of tungsten. The vaporized copper carries away the part of energy from the arc which cannot be conducted into the contact in time, thus the temperature of the site vaporization taken place keeps at the melting point of tungsten (3680K).

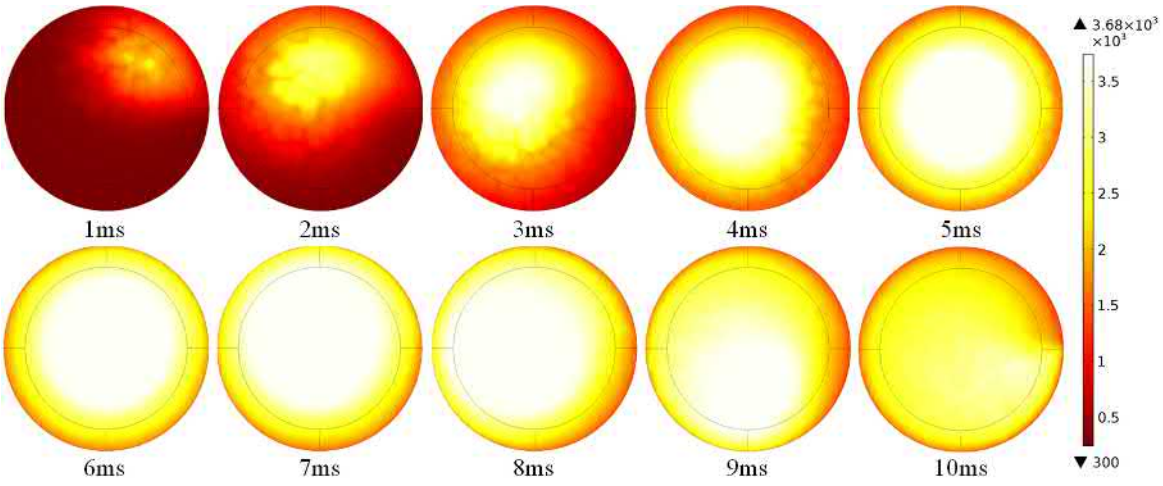

Fig. 6.6 Time variation of surface temperature of CuW contact at 20kA$_p$.

As the current further increased to 40kA (Figure 6.7), the radius of the arc root reaches the radius of the contact surface in a very short time. Once the radius of the arc root reaches the radius of the contact surface, the current intensity increases and it results in a higher energy flux from the arc. As shown in Figure 6.7, from 4ms to 9ms, almost the entire contact surface reaches the melting point of tungsten and mass loss occurs all over the contact surface.

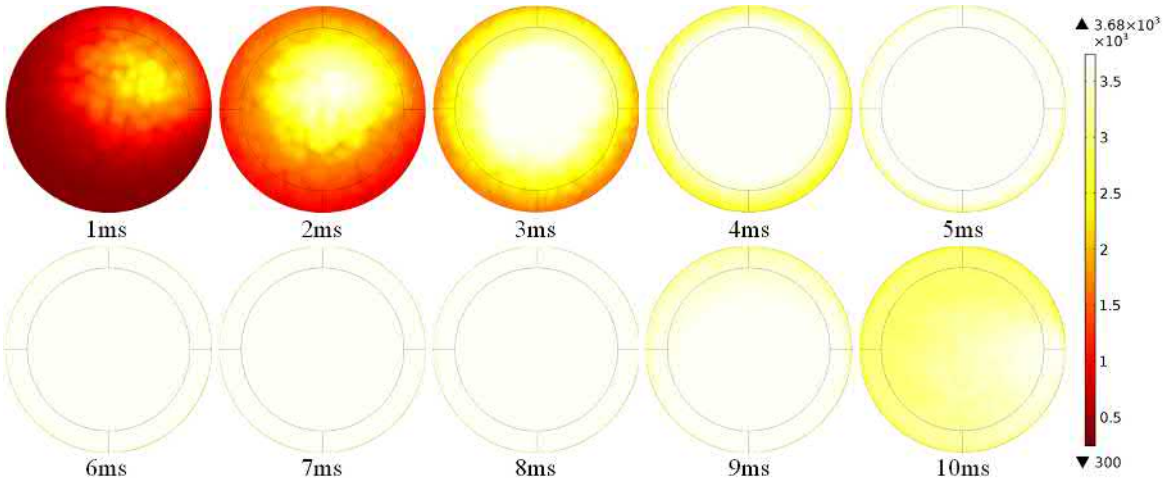

Fig. 6.7 Time variation of surface temperature of CuW contact at 40kA$_p$.

6.3.2 Mass Loss of Arcing Contact

To study the effect of arc root movement on the mass loss of an arcing contact, besides the case of moving arc roots, the case of stationary arc roots has also been conducted using the same model and parameters described above except fixing the arc root at the centre of the contact surface. For both the moving and stationary arc root cases, the mass loss rates of CuW contact as function of time $\dot{m}(t)$ at various peak currents are derived according to Equation 6.3 and plotted in Figure 6.8.

Figure 6.8 (a) shows that the mass loss rate increases as the peak current increases. Mass loss occurs at all current levels. The onset time of mass loss at different currents are relatively constant at 1.5($\pm$0.1)ms. According to the erosion theory proposed by Donaldson[34], it is known that the product of the effective energy flux and onset time of mass loss is a constant for a given material. For the stationary arc case, before the arc root reaches the dimension of the contact surface, the current density and the energy flux at the centre of arc root is a constant. Therefore, the onset time of mass loss is constant.

Figure 6.8 (b) shows the mass loss rate of a moving arc root as a function of time. In general, the mass loss rate increases as the peak current increases which is the same as for the stationary arc. However, it is found that the mass loss rates at low currents are lower than that of stationary arc conditions. Especially, at 5kA$_p$, the mass loss rate is zero during the whole arc period indicating that the movement of arc root has

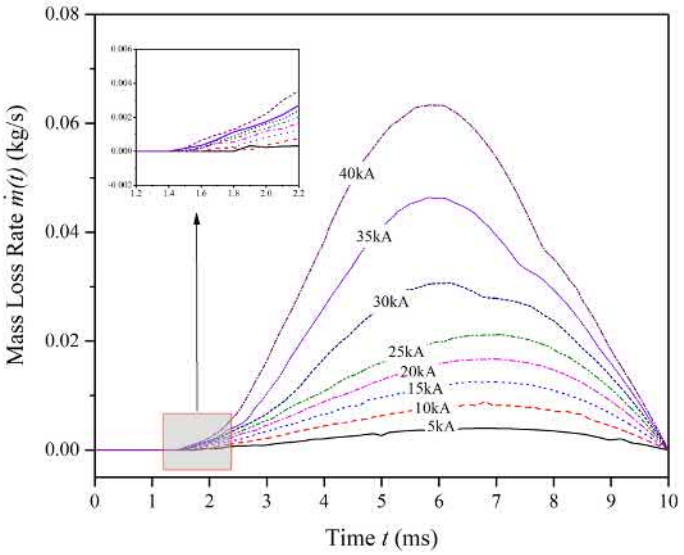

(a) Case of stationary arc root

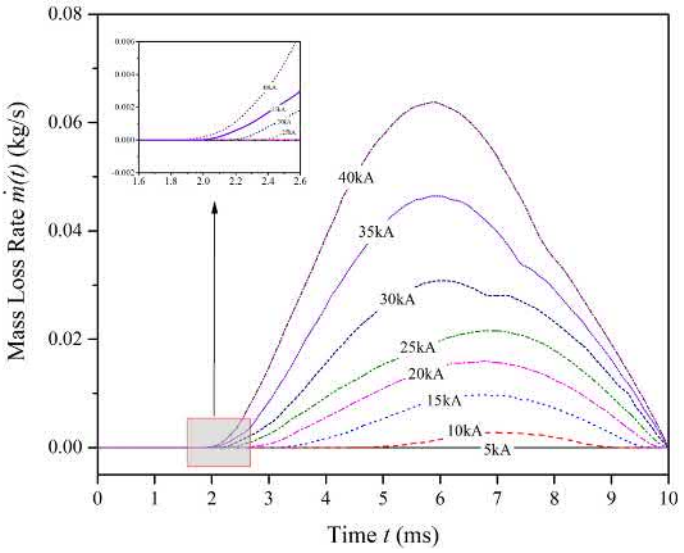

(b) Case of moving arc root

Fig. 6.8 Time variation of mass loss rate $\dot{m}(t)$ of CuW contact at various current amplitudes.

significantly reduced the mass loss. Also, the onset time of mass loss are later than the case of a stationary arc, between 1.9ms to 5.0ms. The variation of erosion onset time is consistent with the occurrence of copper vapour observed from high-speed photographs as shown in Figure 3.13 to 3.15 (Chapter 3). At high currents, such as 35 and 40kA$_p$, the erosion characteristics of a moving arc are not very different from those of the stationary arc.

The total mass loss of a CuW contact at various current amplitudes are derived according to Equation 6.4 and plotted in Figure 6.9. The measured mass loss values of CuWSF6-S (CuW contact in SF_6) are also plotted in the graph, and the test numbers are also designated in the circle.

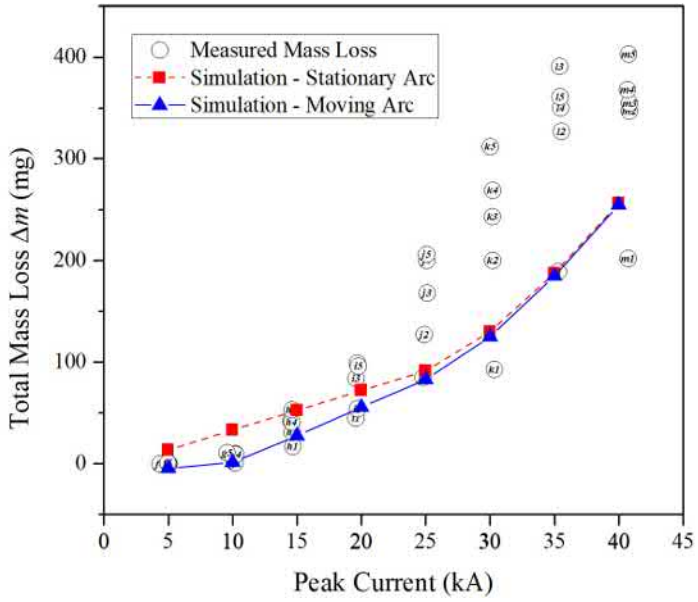

Fig. 6.9 Comparison between the simulated and measured mass loss of CuW contact at various current amplitudes.

Figure 6.9 shows that the simulation results for the stationary arc and moving arc have similar increasing trend with peak current. The predicted mass loss values of the stationary arc are higher than that of the moving arc at low currents. As the current increases, their difference decreases. In terms of the simulation results of a moving arc, it is seen that from 5 to 10kA$_p$, the simulation mass loss values show good agreement with the measured mass loss; from 15 to 40kA$_p$, the simulation mass loss values are generally higher than the theoretical values. However, the mass loss from the first test in each case is similar to the theoretical value. This trend can be explained as following. Refer to the discussion in Chapter 4, the mass loss of the first test on a new CuW contact is mainly caused by vaporization regardless of the magnitude of the current which corresponds to the vaporization condition used theoretically. Therefore, the simulation results from the moving arc model can provide a lower limit of the mass loss of CuW contacts. However, the calculated mass loss values using the stationary arc model at low currents are over estimated. For instance, the relative error at 10kA$_p$

can reach approximately 500%. As the current increases, the effect of the arc root movement on mass loss decreases resulting in small difference between the predicted mass loss of stationary arc and moving arc.

To gain a better prediction at high currents, the surface degradation of the CuW contact and molten droplet ejection should be taken into consideration. With increasing test numbers, the contact surface morphology will be much changed and the mass loss caused by molten droplet ejection will substantially increase. This is the reason why the measured mass loss at high currents are greater than the simulated results.

6.3.3 Arcing Contact Surface Deformation

Along with the calculation of contact mass loss, the surface deformation is simulated at the same time using the Deformed Geometry module[99]. The simulated surface height change of CuW contact (top) and photographies (bottom) are shown in Figure 6.10. The colour bar indicates the decreased height of the contact surface in mm.

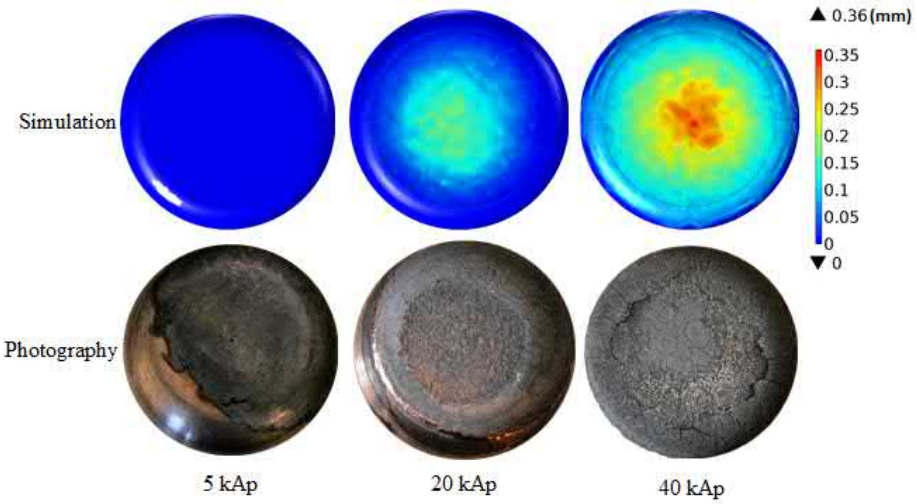

Fig. 6.10 Comparison of the photographies and simulated height change of the CuW contact surface.

As shown in Figure 6.10, at 5kA$_p$, the simulated height change of the contact surface is zero since no mass loss occurred at this current. The photograph of the contact surface after the test at 5kA$_p$ shows the same results - apart from the change of surface colour, there is almost no observable deformation of the contact surface. At 20kA$_p$, the simulation result shows that the mass loss (height change) occurs at the

centre of the contact surface while the edge area is not affected. The maximum height change is approximately 0.2mm at the centre area. A similar pattern is observed on the contact surface photograph after 20kA$_p$ arc erosion. The colour of the contact surface is changed to greyish indicating that the copper has been vaporized on the contact surface. In particular, a sunken area is observed at the centre of the contact which is consistent with the simulation result. At 40kAkA$_p$, the simulation result shows that the area subjected to mass loss expands to the entire contact surface and the height change at the centre is also enhanced. The maximum height change increases to 0.36mm. The photograph of the contact surface shows that the colour of the contact surface has completely changed to dark grey indicating only the tungsten skeleton and solidified tungsten remain on the contact surface layer. In addition, the cracks on the contact surface implies that there is much material eroded from the central area resulting in a pronounced sunken area.

In general, the simulation results of CuW contact surface deformation show good agreement with experimental photographs.

6.4 Summary

A 3D thermal model of the plug arcing contact was proposed using the commercial simulation package COMSOL Multiphysics, considering the effect of arc root movement on the contact surface. The contact temperature distribution and its time variation, the mass loss of plug contact and the geometry deformation for different peak currents of a CuW contact were simulated. The results were compared with experimental data. The following conclusions have been drawn:

(1) The temperature distribution and time-variation of the copper-tungsten contact surface had been simulated considering the effect of arc root movement. The heating effect of the arc root on the contacts (especially at low current) was significantly reduced. For example, at 5kA, the maximum temperature of the contact surface was only 3070K, which was still below the boiling point of metal tungsten, without causing mass loss. In addition, the highest temperature of the contacts at low currents occurred on the edge of the contact. As the current increases, the contact surface temperature rose and remained at the melting point of the metal tungsten.

(2) The mass loss rate of arcing contact erosion at different currents was obtained by simulation. Under the stationary arc root condition, the moment at which the material of the contact vaporized hardly changes with the increase of the current. For the model considering the movement of the arc root, the timing at which the vaporization of the contact material occurs coincided with the occurrence of the metal vapour on the high-speed photographs appearing between 1.9-5.0 ms depending on the current level.

(3) The mass loss values of arcing contact under stationary and moving arc root cases were obtained by simulation and compared with the experimental results. The results showed that the mass loss of arcing contact of stationary arc root is much higher than the experimental results. At 10kA, the relative error exceeded 500%. On the contrary, for the moving arc root model, the simulation results were basically consistent with the mass loss values of the first test of the arcing contacts at each current level.

(3) The simulated height change of CuW contact surface caused by arc erosion showed good agreement with experimental results.

Chapter 7

Conclusions and Future Work

7.1 Conclusions

With the development of social and economic construction, the requirements for safe and stable operation of power systems and reliable supply of power are increasing. As a protection device for the power system, the reliable operation of the SF_6 HVCB is related to the safety and stability of the entire power grid. As the components directly exposed to arcs in HVCBs, the working conditions and electrical lifetime of arcing contacts determine the reliability and service lifetime of the equipment. In this paper, the arcing contact erosion of SF_6 HVCB was taken as the main research object. The combination of experiment and simulation is used to further study the erosion mechanism and prediction method of mass loss of arcing contact. The main conclusions are as follows:

(1) An experimental system based on a commercial 245kV/40kA SF_6 live tank self-blast HVCB was built for arcing contacts erosion research. The macroscopic behaviour of the arc were observed by the combination of a high-speed camera and a group of mirrors. In particular, this work designed a novel fibre-optic sensor system that, in combination with photo-diodes and high-speed spectrometers, can simultaneously monitor the trajectory of the arc root on the surface of the arcing contact and the time-varying spectrum of the arc. In the process of constructing the experimental system, the experimental method based on optical measurement is used to effectively

solve the insulation problem of the monitoring equipment and avoid the adverse effects of electromagnetic interference on the experimental results.

(2) The macroscopic behaviour of arc in SF_6 HVCB and its influence on arcing contact erosion were studied by using spatial domain chromatic method. At low currents (less than 15kA), the mobility of the arc root has an important effect on the erosion of the arcing contacts. Therefore, this thesis uses the optical measurement method to monitor the macroscopic behaviour of the arc in the SF_6 HVCB. By analysing the high speed photographs, it is found that the arc column is non-axisymmetric in space. As the arc current increases, the diameter of the arc column increases gradually and the stability increases. The dynamic distribution of metal vapour in the arc column is closely related to the peak current. The arc root moves rapidly on the surface of the arcing contact while preferentially occupying the edge area of the contact surface. As the current increases, the arc root gradually fills the surface of the arcing contact, and the mobility decreases. For the CuW contact material, as the number of experiments increased, the probability of droplet ejection on the contact surface was gradually increased. Using the spatial domain chromatic method, the trajectory of the arc root movement on the contact surface was measured, and the activity of the arc root movement, i.e. $\overline{d_{act}}$, at different current levels was studied. A quantitative relationship between $\overline{d_{act}}$ and the mass loss of arcing contact erosion was obtained. At the same current (less than 15kA), the activity of the arc root movement was inversely proportional to the mass loss of the arcing contact. The spatial domain chromatic method was used to predict the mass loss of the arcing contact, and the prediction accuracy was improved by 31.0% compared with the widely used arc energy method.

(3) The the wavelength domain and time domain chromatic methods were used to process the time-resolved spectra of the arc, and the quantitative relationship between the mass loss of the arcing contact and the chromatic parameters was explored. At high currents (greater than 15 kA), the erosion of the arcing contacts has a significant effect on the spectral radiation of the arc. Therefore, the time-resolved arc spectra were processed by using the wavelength domain and the time domain chromatic method. The quantitative relationship between the mass loss of the arcing contact and the chromatic parameters were obtained. Using the wavelength domain chromatic parameter $H_{\mathrm{w}}(\mathrm{t_p})$ and $L_{\mathrm{w}}(\mathrm{t_p})$, the equivalent dominant wavelength and the effective signal strength

of the arc spectra were obtained, respectively. Therefore, the erosion pattern and the relative mass loss of the CuW contacts were recognised. Using the time domain chromatic analysis, the time-resolved characteristics of the arc spectra of arc erosion were obtained at different current levels. Furthermore, by combining with the linear regression algorithm, the method of prediction of mass loss of arcing contact at high currents based on chromatic parameters was obtained. The prediction accuracy of mass loss of CuW contacts was improved by 39.1% compared with the widely used arc energy method by using the time domain chromatic parameters.

(4) A 3D thermal model of the plug arcing contact has been proposed considering the effect of arc root movement on the contact surface. The contact temperature distribution and its time variation, the mass loss of plug contact and the geometry deformation for different peak currents of a CuW contact are simulated. At 5kA, the maximum temperature of the contact surface was only 3070K, which was still below the boiling point of metal tungsten, without causing mass loss. For the model considering the movement of the arc root, the timing at which the vaporization of the contact material occurs coincided with the occurrence of the metal vapour on the high-speed photographs appearing between 1.9-5.0 ms depending on the current level. The predicted mass loss of arcing contact of stationary arc root is much higher than the experimental results. At 10kA, the relative error exceeded 500%. On the contrary, for the moving arc root model, the simulation results were basically consistent with the mass loss values of the first test of the arcing contacts at each current level.

7.2 Future Work

During this study, the experimental conditions are set to be as close as possible to the practical operation condition of HVCB. However, due to the complexity of the arcing contact erosion process, it is very difficult to cover all the possible current breaking conditions in one study. In the future, it is necessary to consider a more in-depth study from the following aspects:

(1) Change the arcing time. The current conducted in this study was generated using a synthetic loop circuit which limits the duration of arcing time. During the practical current breaking process in the field, the time of arc quenching varies (generally

last longer than one half cycle). The phase angle of the current at the moment of the arcing contacts separation may also be different from shot to shot. These factors all have effects on the erosion of arcing contact. To provide an accurate prediction of the mass loss of arcing contact, it is necessary to consider the effect of the changing the arcing time during the breaking tests.

(2) The effect of the external gas flow on the erosion of arcing contact need to be studied in detail. The gas flow generated during the current breaking process in the arcing channel not only influences the thermal process between the arc and arcing contacts, but also plays a important role on the material removal at the arcing contact surface.

(3) Replace the high-speed spectrometer with photo-diode and light filters to reduce the cost of the on-line monitoring system. The high-speed spectrometer is costly and the maintenance process is rather complex which is not sufficiently stable for the on-line monitoring applications in the power industry. Thanks to the chromatic processing methods, the high-speed spectrometer can be replaced by three photo-diode with light filters (which can be regarded as wavelength domain processors). On one hand, this measure reduces the cost of the monitoring system; on the other hand, this measure can potentially improve the processing speed of on-line monitoring system by realising the wavelength domain processing on the hardware level.

References

[1] 中国电力企业联合会. 中国电力行业年度发展报告2016. 电器工业, (9), 2016.

[2] 能源局. 2016年全社会用电量. 2017.

[3] IEC Standard. 62271-100 high-voltage switchgear and controlgear. 5, 2001.

[4] A. L. J. Janssen, J. H. Brunke, C. R. Heising, and W. Lanz. Cigre wg 13.06 studies on the reliability of single pressure sf 6 -gas high-voltage circuit-breakers. *IEEE Transactions on Power Delivery*, 11(1):274–282, 1996.

[5] Charles R Heising. Worldwide reliability survey of high-voltage circuit breakers. *IEEE Industry Applications Magazine*, 2(3):65–66, 1996.

[6] G. R. Jones, N. Y. Shammas, and A. N. Prasad. Radiatively induced nozzle ablation in high-power circuit interrupters. *Ieee Transactions on Plasma Science*, 14(4):413–422, 1986.

[7] J. J. Shea. High current ac break arc contact erosion. In *Electrical Contacts, 2008. Proceedings of the 54th IEEE Holm Conference on*, pages xxii–xlvi.

[8] L. H. Germer. Physical processes in contact erosion. *Journal of Applied Physics*, 29(7):1067–1082, 1958.

[9] A. Gleizes, J. J. Gonzalez, and P. Freton. Thermal plasma modelling. *Journal of Physics D-Applied Physics*, 38(9):R153–R183, 2005.

[10] A. B. Murphy. Thermal plasmas in gas mixtures. *Journal of Physics D-Applied Physics*, 34(20):R151–R173, 2001.

[11] V. Abbasi, A. Gholami, and K. Niayesh. The effects of sf6-cu mixture on the arc characteristics in a medium voltage puffer gas circuit breaker due to variation of thermodynamic properties and transport coefficients. *Plasma Science & Technology*, 15(6):586–592, 2013.

[12] O. Coufal and O. Zivny. Composition and thermodynamic properties of thermal plasma with condensed phases. *European Physical Journal D*, 61(1):131–151, 2011.

[13] A. B. Murphy. Calculation and application of combined diffusion coefficients in thermal plasmas. *Scientific Reports*, 4, 2014.

[14] A. Gleizes, B. Rahmani, J. J. Gonzalez, and B. Liani. Calculation of net emission coefficient in n2, sf6 and sf6-n2 arc plasmas. *Journal of Physics D-Applied Physics*, 24(8):1300–1309, 1991.

[15] J. D. Yan, S. M. Han, Y. Y. Zhan, H. F. Zhao, and M. T. C. Fang. Computer simulation of the arcing process in high voltage puffer circuit breakers with hollow contacts. *Xviiith Symposium on Physics of Switching Arc*, pages 99–108, 2009.

[16] B. Chervy and A. Gleizes. Electrical conductivity in sf6 thermal plasma at low temperature (1000-5000 k). *Journal of Physics D-Applied Physics*, 31(19):2557–2565, 1998.

[17] W. Z. Wang, M. Z. Rong, J. D. Yan, A. B. Murphy, and J. W. Spencer. Thermophysical properties of nitrogen plasmas under thermal equilibrium and non-equilibrium conditions. *Physics of Plasmas*, 18(11), 2011.

[18] X. H. Wang, L. L. Zhong, Y. Cressault, A. Gleizes, and M. Z. Rong. Thermophysical properties of sf6-cu mixtures at temperatures of 300-30,000 k and pressures of 0.01-1.0 mpa: part 2. collision integrals and transport coefficients. *Journal of Physics D-Applied Physics*, 47(49), 2014.

[19] M. Z. Rong, L. L. Zhong, Y. Cressault, A. Gleizes, X. H. Wang, F. Chen, and H. Zheng. Thermophysical properties of sf6-cu mixtures at temperatures of 300-30 000 k and pressures of 0.01-1.0 mpa: part 1. equilibrium compositions and thermodynamic properties considering condensed phases. *Journal of Physics D-Applied Physics*, 47(49), 2014.

[20] J. C. Lee and Y. J. Kim. The influence of metal vapors resulting from electrode evaporation in a thermal puffer-type circuit breaker. *Vacuum*, 81(7):875–882, 2007.

[21] J. L. Zhang, J. D. Yan, and M. T. C. Fang. Electrode evaporation and its effects on thermal arc behavior. *Ieee Transactions on Plasma Science*, 32(3):1352–1361, 2004.

[22] V. K. Liau, B. Y. Lee, K. D Song, and K. Y. Park. The influence of contacts erosion on the sf6 arc. *Journal of Physics D-Applied Physics*, 39(10):2114–2123, 2006.

[23] M. Landry, A. Mercier, G. Ouellet, C. Rajotte, J. Caron, M. Roy, and F. Brikci. A new measurement method of the dynamic contact resistance of hv circuit breakers. *2005/2006 Ieee/Pes Transmission & Distribution Conference & Exposition, Vols 1-3*, pages 1002–1009, 2006.

[24] R. Holm. The vaporization of the cathode in the electric arc. *Journal of Applied Physics*, 20(7):715–716, 1949.

[25] WR Wilson. High-current arc erosion of electric contact materials [includes discussion]. *Power Apparatus and Systems, Part III. Transactions of the American Institute of Electrical Engineers*, 74(3), 1955.

[26] G. Ecker. Electrode components of the arc discharge. *Ergebnisse Der Exakten Naturwissenschaften*, 33:1–104, 1961.

[27] X. Zhou, J. Heberlein, and E. Pfender. Theoretical-study of factors influencing arc erosion of cathode. *Electrical Contacts - 1992 : Proceedings of the Thirty-Eighth Ieee Holm Conference on Electrical Contacts*, pages 71–78, 1992.

[28] X. Zhou, J. Heberlein, and E. Pfender. Theoretical-study of factors influencing arc erosion of cathode. *Ieee Transactions on Components Packaging and Manufacturing Technology Part A*, 17(1):107–112, 1994.

[29] X. Zhou and J. Heberlein. An experimental investigation of factors affecting arc-cathode erosion. *Journal of Physics D-Applied Physics*, 31(19):2577–2590, 1998.

[30] J. Tepper, M. Seeger, T. Votteler, V. Behrens, and T. Honig. Investigation on erosion of cu/w contacts in high-voltage circuit breakers. *Ieee Transactions on Components and Packaging Technologies*, 29(3):658–665, 2006.

[31] Y. Nakagawa and Y. Yoshioka. Theoretical calculation of the process of contact arc erosion using a one-dimensional contact model. *IEEE Transactions on Components, Hybrids, and Manufacturing Technology*, 1(1):99–102, 1978.

[32] A. L. Donaldson, M. O. Hagler, M. Kristiansen, G. Jackson, and L. Hatfield. Electrode erosion phenomena in a high-energy pulsed discharge. *Ieee Transactions on Plasma Science*, 12(1):28–38, 1984.

[33] Anthony Lyle Donaldson. *Electrode erosion measurements in a high energy spark gap*. Thesis, 1982.

[34] Anthony L Donaldson. Electrode erosion in high current, high energy transient arcs. 1990.

[35] E. Walczuk. Arc erosion of high current contacts in the aspect of cad of switching devices. In *Electrical Contacts, 1992., Proceedings of the Thirty-Eighth IEEE Holm Conference on*, pages 1–16.

[36] P. Teste, T. Leblanc, R. Andlauer, and J. P. Chabrerie. Copper cathode erosion by an electric arc - the causes of the variations of the erosion rate with the electrode gap. *Plasma Sources Science & Technology*, 10(1):10–16, 2001.

[37] P Borkowski and E Walczuk. Influence of contact diameter on arc erosion of polarised contacts at high current conditions. 2005.

[38] P. Borkowski and A. Sienicki. Contacts erosion modelling using ansys computer software and experimental research. *Archives of Metallurgy and Materials*, 60(2):551–560, 2015.

[39] J. J. Shea. Erosion and resistance characteristics of agw and agc contacts. *Ieee Transactions on Components and Packaging Technologies*, 22(2):331–336, 1999.

[40] H. W. Turner and C. Turner. Choosing contact materials. *Electronics and Power*, 14(Nov):437–&, 1968.

[41] HW Turner, C Turner, and JS Yap. *The relation between wear of copper contacts and arc current*. British Electrical and Allied Industries Research Association, 1966.

[42] HW Turner and C Turner. Contact materials, their properties and uses. *Electrical Times*, (Part 3), 1967.

[43] Y. L. Wang, S. H. Liang, and Z. B. Li. Experiment and simulation analysis of surface structure for cuw contact after arc erosion. *Materials Science and Technology*, 31(2):243–247, 2015.

[44] 李六零, 丁卫东, 石月春, and 邱毓昌. 动态电阻测量法用于评估sf6断路器灭弧室状况的探讨. 高压电器, 38(2):54–55, 2002.

[45] 黄瑜珑and 钱家骊. Sf6断路器不拆卸检测技术. 高压电器, (2):9–12, 1996.

[46] J Michaelson and A Moglestue. Seeing through switchgear. *ABB Review*, (4), 2012.

[47] P. N. Stoving and J. F. Baranowski. Interruption life of vacuum circuit breakers. *Isdeiv: Xixth International Symposium on Discharges and Electrical Insulation in Vacuum, Vols 1 and 2, Proceedings*, 19:388–391, 2000.

[48] 王阳, 朴在林, 王雪梅, and 刘海营. 断路器电寿命在线监测的几种计算方法. 沈阳农业大学学报, 36(2):250–252, 2005.

[49] 关永刚. 高压开关柜在线监测与故障诊断的研究和应用. Thesis, 2001.

[50] R Jeanjean, C Salzard, and P Migaud. Electrical endurance tests for hv circuit-breakers: Edf experience. In *Power Engineering Society Winter Meeting*, pages 294–298 vol.1.

[51] A. Pons, A. Sabot, and G. Babusci. Electrical endurance and reliability of circuit-breakers-common experience and practice of two utilities. *IEEE Transactions on Power Delivery*, 8(1):168–174, 1993.

[52] T Roininen, CE Solver, H Nordli, A Bosma, P Jonsson, and A Alfredsson. Abb live tank circuit breakers, application guide. *Publication 1HSM*, 9543:2013–02.

[53] Y. Tanaka, Y. Yokomizu, T. Matsumura, and Y. Kito. Transient distribution of metallic vapour concentration in a post-arc channel after current zero along the nozzle axis in a flat-type sf6 gas-blast quenching chamber. *Journal of Physics D-Applied Physics*, 29(6):1540–1550, 1996.

[54] P. G. Slade and Schulzgu.E. Spectroscopic analysis of high-current free-burning ac arcs between copper contacts in argon and air. *Journal of Applied Physics*, 44(1):157–162, 1973.

[55] S. Okuda, Y. Ueda, Y. Murai, T. Miyamoto, Y. Doi, and C. Uenosono. Spectroscopic approach to the analysis of high-current arcs in sf6. *Ieee Transactions on Plasma Science*, 8(4):395–399, 1980.

[56] A. B. Murphy. Modified fowler-milne method for the spectroscopic measurement of temperature and composition of multielement thermal plasmas. *Review of Scientific Instruments*, 65(11):3423–3427, 1994.

[57] E. W. Gray. Some spectroscopic observations of the two regions (metallic vapor and gaseous) in break arcs. *IEEE Transactions on Plasma Science*, 1(1):30–33, 1973.

[58] Yasunori Tanaka, Yasunobu Yokomizu, Motohiro Ishikawa, Toshiro Matsumura, and Yukio Kito. Dominant spectra of background radiation in a sf 6 post-arc channel. *Plasma Science, IEEE Transactions on*, 25(5):986–990, 1997.

[59] N. Moriyama, J. Sekikawa, and T. Kubono. Spectroscopic temperature measurement of breaking arcs near cathode and anode surfaces of copper contacts. *Ieice Transactions on Electronics*, E89c(8):1141–1146, 2006.

[60] M. E. Rouffet, Y. Cressault, A. Gleizes, and J. Hlina. Thermal plasma diagnostic methods based on the analysis of large spectral regions of plasma radiation. *Journal of Physics D-Applied Physics*, 41(12), 2008.

[61] S. Franke, R. Methling, D. Uhrlandt, R. Bianchetti, R. Gati, and M. Schwinne. Temperature determination in copper-dominated free-burning arcs. *Journal of Physics D-Applied Physics*, 47(1), 2014.

[62] H.R. Griem. *Plasma Spectroscopy*. McGraw-Hill, 1964.

[63] J. Cooper. Plasma spectroscopy. *Reports on Progress in Physics*, 29:35–+, 1966.

[64] P. C. Russell, R. Haber, G. R. Jones, and W. McGrory. A chromatically addressed optical fibre sensor for non-contact temperature monitoring. *Sensors and Actuators a-Physical*, 76(1-3):231–240, 1999.

[65] M. M. Murphy and G. R. Jones. Optical fiber pressure measurement. *Measurement Science & Technology*, 4(3):258–262, 1993.

[66] L. T. Isaac, J. W. Spencer, J. Humphries, G. R. Jones, and W. Hall. Optical-fibre-based investigations of contact travel, gas pressure and particle concentration in sf₆ puffer circuit breakers. *Generation, Transmission and Distribution, IEE Proceedings-*, 146(5):453–458, 1999.

[67] J. A. Cosgrave, J. W. Spencer, G. R. Jones, K. G. Lewis, and W. B. Hall. An optical fibre-based acoustic sensor for detecting electrical discharges in sf₆ puffer circuit breakers. In *Dielectric Materials, Measurements and Applications, Seventh International Conference on (Conf. Publ. No. 430)*, pages 307–312.

[68] J. A. Cosgrave, A. Vourdas, G. R. Jones, J. W. Spencer, and A. Wilson. Acoustic monitoring of electrical discharges using fiberoptic based techniques. *International Conference on Acoustic Sensing Imaging*, (369):278–283, 1993.

[69] Leslie Thomas Isaac. *Puffer circuit breaker diagnostics using novel optical fibre sensors*. Thesis, 1997.

[70] J. E Humphries, A Koh, J. W Spencer, T Mori, H Ikeda, and Y Kanazawa. Chromatic based method for monitoring electrode wear. 2006.

[71] T Mori, Y Kanazawa, H Kawano, H Ikeda, J. E Humphries, A Koh, and J. W Spencer. Feasibility study of electrode wear monitoring by spectra measurement. 日本磁共医学会, 29:97–103, 2006.

[72] Yasunobu Yokomizu, J. W. Spencer, and G. R. Jones. Position location of a filamentary arc using a tristimulus chromatic technique. *Journal of Physics D: Applied Physics*, 31(23):3373–3382, 1998.

[73] A. Koh, G. R. Jones, J. W. Spencer, and I. Thomas. Chromatic analysis of signals from a driver fatigue monitoring unit. *Measurement Science & Technology*, 18(3):747–754, 2007.

[74] S. Q. Xu and G. R. Jones. Event and movement monitoring using chromatic methodologies. *Measurement Science & Technology*, 17(12):3204–3211, 2006.

[75] L. T. Isaac, G. R. Jones, J. E. Humphries, J. W. Spencer, and W. B. Hall. Monitoring particle concentrations produced by arcing in sf6 circuit breakers using a chromatic modulation probe. *IEE Proceedings: Science, Measurement and Technology*, 146(4):199–204, 1999.

[76] Dimitrios Tomtsis. *Intelligent Plasma Monitoring Systems Based on Optical Methods and Chromatic Modulation*, pages 361–366. Springer, 2010.

[77] Analog Devices. 160db range (100pa-10ma) logarithmic converter ad8304. 2012.

[78] F. Pons and M. Cherkaoui. An electrical arc erosion model valid for high current: Vaporization and splash erosion. In *2008 Proceedings of the 54th IEEE Holm Conference on Electrical Contacts*, pages 9–14.

[79] Y. Tanaka. Influence of copper vapor contamination on dielectric properties of hot air at 300-3500 k in atmospheric pressure. *Ieee Transactions on Dielectrics and Electrical Insulation*, 12(3):504–512, 2005.

[80] H. X. Miao, H. H. Wang, and Y. Xu. The numerical calculation and optimization design of electric field for the high voltage sf(6) circuit breaker arc-quenching chamber. *2009 International Conference on Sustainable Power Generation and Supply, Vols 1-4*, pages 2505–2509, 2009.

[81] Z. Kolacinski. Plasma contamination with electrode metal vapor jets. *Plasma Chemistry and Plasma Processing*, 6(3):299–310, 1986.

[82] Y. Yokomizu, T. Matsumura, and Y. Kito. Approximate numerical calculation method for deriving an asymmetrical temperature distribution in a cross-section of a gas-blasted arc. *European Transactions on Electrical Power*, 7(2):91–97, 1997.

[83] A. L. Donaldson and M. Kristiansen. Electrode erosion as a function of electrode materials in high current, high energy transient arcs. In *Pulsed Power Conference, 1989. 7th*, pages 83–86. IEEE.

[84] A. Marotta and L. I. Sharakhovsky. A theoretical and experimental investigation of copper electrode erosion in electric arc heaters .1. the thermophysical model. *Journal of Physics D-Applied Physics*, 29(9):2395–2403, 1996.

[85] ABB. Circuit breaker sentinel, 2017.

[86] J. W. Spencer, A. Deakin, and G. R. Jones. Monitoring of complex systems. In *Gas Discharges and Their Applications, 2008. GD 2008. 17th International Conference on*, pages 41–48.

[87] Michael H. Kutner, Christopher J. Nachtsheim, and John Neter. Applied linear regression models (5th ed.). *Technometrics*, 26(4), 2004.

[88] Marija J Norušis. *SPSS/PC+ for the IBM PC/XT/AT*, volume 1. Spss, 1986.

[89] Certified Consultants. Comsol multiphysics version 5.2 release highlights.

[90] Paul G Slade. *Electrical contacts: principles and applications*. CRC Press, 2013.

[91] F Mark Lehr and Magne Kristiansen. Electrode erosion from high current moving arcs. *Plasma Science, IEEE Transactions on*, 17(5):811–817, 1989.

[92] P. Teste, T. Leblanc, J. Rossignol, and R. Andlauer. Contribution to the assessment of the power balance at the electrodes of an electric arc in air. *Plasma Sources Science & Technology*, 17(3), 2008.

[93] T. J. Xu, M. Z. Rong, Y. Wu, and Q. Ma. The study on the anode current density distribution in a moving arc root. *2009 Asia-Pacific Power and Energy Engineering Conference (Appeec), Vols 1-7*, pages 3767–3770, 2009.

[94] J. Li and M. Z. Rong. 2-d model for calculating current density distribution and flux-flow resistivity of mcp bscco-2212 rod during quenching process in self field. *Ieice Transactions on Electronics*, E88c(8):1659–1663, 2005.

[95] Y. L. Wang. 电弧作用下cuw触头的热冲击效应分析. 稀有金属材料与工程, 41(2), 2012.

[96] Y. Nakagawa and Y. Yoshioka. Theoretical calculation of process of contact arc erosion using a one-dimensional contact model. *Ieee Transactions on Components Hybrids and Manufacturing Technology*, 1(1):99–102, 1978.

[97] 李达人, 蔡一湘, 刘祖岩, and 王尔德. W-cu合金物理性能模型及理论值计算. 中国钨业, 26(6):35–38, 2011.

[98] R. M. German. A model for the thermal-properties of liquid-phase sintered composites. *Metallurgical Transactions a-Physical Metallurgy and Materials Science*, 24(8):1745–1752, 1993.

[99] Certified Consultants. Deformed geometry module - comsol 5.2 release highlights.

[100] Parry Hiram Moon and Domina Eberle Spencer. *The photic field*. Cambridge (Mass.): MIT Press, 1981.

[101] E. Elzagzoug, G. R. Jones, A. G. Deakin, and J. W. Spencer. Condition monitoring of high voltage transformer oils using optical chromaticity. *Measurement Science and Technology*, 25(6), 2014.

[102] J. H. Zhang, G. R. Jones, A. G. Deakin, and J. W. Spencer. Chromatic processing of dga data produced by partial discharges for the prognosis of hv transformer behaviour. *Measurement Science & Technology*, 16(2):556–561, 2005.

[103] A. A. Al-Temeemy and J. W. Spencer. Invariant spatial chromatic processors for region image description. In *Imaging Systems and Techniques (IST), 2010 IEEE International Conference on*, pages 421–425.

[104] P. J. Scully, R. Holmes, and G. R. Jones. Optical fiber-based goniometer for sensing patient position and movement within a magnetic-resonance scanner using chromatic modulation. *Journal of Medical Engineering & Technology*, 17(1):1–8, 1993.

[105] G. R. Jones, P. C. Russell, A. Vourdas, J. Cosgrave, L. Stergioulas, and R. Haber. The gabor transform basis of chromatic monitoring. *Measurement Science & Technology*, 11(5):489–498, 2000.

[106] Gordon Rees Jones, Anthony Grayham Deakin, and Joseph W. Spencer. *Chromatic monitoring of complex conditions*. Series in sensors. CRC Press, 2008.

[107] Fred W Billmeyer and Max Saltzman. Principles of color technology. *Principles of Color Technology*, 1981.

Appendix A

Basic Principles of Chromatic Methodology

A.1 Philosophy and Applications of Chromatic Methodology

The chromatic approaches evolve from the theory of photic field [100] and colour science, where the mammals' perception of light is a typical example. Three different cone cells in human eyes are sensitive to light in different wavelength ranges. In the absence of accurate measurement, our brains can process the outputs of the three cone cells simultaneously and recognize the colour easily. This is the basic idea of chromatic method.

Although the chromatic method originate from the processing of optical signals, its application area is far beyond the scope of optical signals. So far, it has been successfully applied to the monitoring of plasma[76], the monitoring of transformer oil degradation[101], RF signal analysis[102], image recognition[103], location and behaviour monitoring[72, 104] and event monitoring[74]. In short, the chromatic approach is to find the cross-correlation between target variable and processed chromatic parameters by means of comparison. Through chromatic processing, the special conditions of the monitored system can be easily recognized, the state of a system can be quantitatively defined and the effective information of the system can be intuitively perceived rather than simple data.

Moreover, when the original signal is a function of multiple variables, it can be processed using chromatic method with respect to each of these variables successively. Every time chromatic processing will compress the amount of data in the corresponding field and achieve the purpose of reducing dimensions. Unlike those machine learning methods such as supporting vector machine (SVM) and neural networks (NN), chromatic processing reserves the traceability of the data which means the low-order data characteristics and trends can be obtained through the analysis of high-order chromatic parameters.

A.2 Basic Algorithms of Chromatic Methodology

The chromatic processing of a signal can be seen as a truncated form of the Gabor transform[105] and usually involves three non-orthogonal Gaussian processors, as shown in Figure A.1.

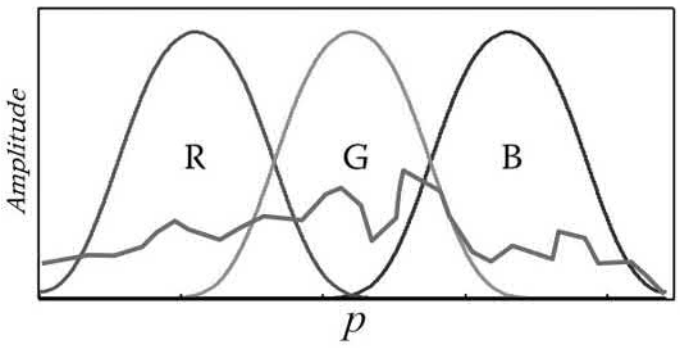

Fig. A.1 Non-orthogoanl Gaussian processors R, G, B[106]

The non-orthogonality of the processor is critical to the chromatic methods. In the process of extracting complex signal features, the non-orthogonal processors have some important properties which can effectively improve the overall signal description accuracy[105]. The sensitivity of the chromatic variables to the signal changes in the overlapping regions can be adjusted through the changing of the width of the overlapping regions between adjacent processors[106].

A.2.1 Chromatic Processing Outputs

The output of each chromatic processor is the product of the response curve and the source signal, usually denoted by R_0, G_0, and B_0, respectively. They can be calculated from the following

$$R_0 = \int S(p)R(p)dp \tag{A.1}$$

$$G_0 = \int S(p)G(p)dp \tag{A.2}$$

$$B_0 = \int S(p)B(p)dp \tag{A.3}$$

where:

p — parameter of interests;

$S(p)$ — source signal;

$R(p)$, $G(p)$, $B(p)$ — response curve of processors R, G and B respectively.

A.2.2 HLS transformation

In order to extract meaningful information from the output of the chromatic processors, the outputs need to undergo different mathematical transformations to highlight some of the characteristics of the original signal. The most basic of which is the HLS transform[106]:

$$H = 240 - 120\frac{g}{g+b} \quad r = 0 \tag{A.4}$$

$$= 360 - 120\frac{b}{b+r} \quad g = 0 \tag{A.5}$$

$$= 120 - 120\frac{r}{r+g} \quad b = 0 \tag{A.6}$$

$$L = \frac{R+G+B}{3} \tag{A.7}$$

$$S = \frac{max(R,G,B) - min(R,G,B)}{max(R,G,B) + min(R,G,B)} \tag{A.8}$$

where:

$$r = R - min(R, G, B) \tag{A.9}$$

$$g = G - min(R, G, B) \tag{A.10}$$

$$b = B - min(R, G, B) \tag{A.11}$$

Max (R, G, B) and min (R, G, B) represent the maximum and minimum values of the parameters (R, G, B), respectively. In general, for the original function S(p) in the parameter p domain, the chromatic parameter H represents the position of dominant value of S(p), L represents the effective signal strength of S(p) i.e. the area under the signal envelope, and (1-S) represents the equivalent signal spread of S(p). If the source signal is a spectrum, the parameter p represents wavelength λ. Therefore, chromatic parameter H represents the dominant wavelength, L represents the effective signal strength, and (1-S) represents the nominal signal spread.

In general, the chromatic parameters H, L, S are demonstrated in two 2D polar plots, as shown in Figure A.2, where the angular coordinates represent H and the radial coordinates represent L and S.

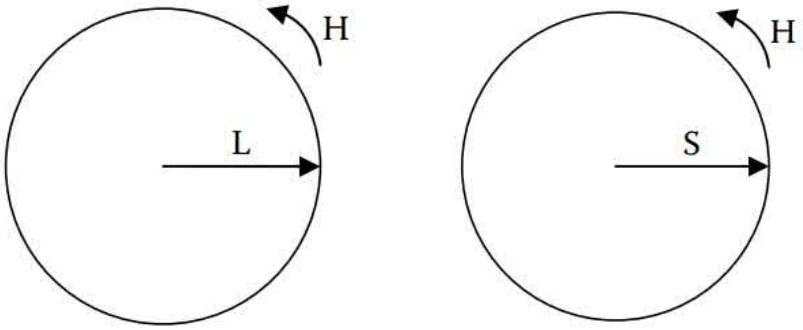

(a) H versus L (b) H versus L

Fig. A.2 Chromatic polar plots

A.2.3 xyz transformation

Another commonly used transformation is called xyz transform, which is derived from the CIE graph in color science[107]. The chromatic parameters x, y and z can be

calculated through the following equations:

$$x = R/(R+G+B) \tag{A.12}$$

$$y = G/(R+G+B) \tag{A.13}$$

$$z = B/(R+G+B) \tag{A.14}$$

It can be derived from the above equations that

$$x + y + z = 1 \tag{A.15}$$

From the point of view of on-line monitoring, the chromatic parameters x and y can be demonstrated in a Cartesian plot (the parameter z is implied by the equation (A.15)), representing the relative signal strength in the coverage area of processor R and G respectively. Unlike the chromatic parameters H, L and S (derived from HLS transformation) represent the overall characteristics of the signal, the x, y and z are used to represent the relative signal strength of the parameter range covered by each processor which contain more detailed information.

Appendix B

Supplementary Plots of Time-resolved Arc Spectra

The experimental results of captured time-resolved arc spectra of selected currents are presented in Chapter 3, Section 3.6. For the results of current amplitudes which are not presented in Chapter 3 but listed in Table 3.2 are listed in Appendix A for reference.

B.1 Time-resolved arc spectra of Cu contact in N_2

The time-resolved spectra of the arc light emission from Cu contact in N_2 at $10kA_p$ and $20kA_p$ are shown in Figure B.1.

B.2 Time-resolved arc spectra of CuW contact in SF_6

The time-resolved spectra of the arc light emission from CuW contact in SF_6 at $10kA_p$ and $20kA_p$ are shown in Figure B.2.

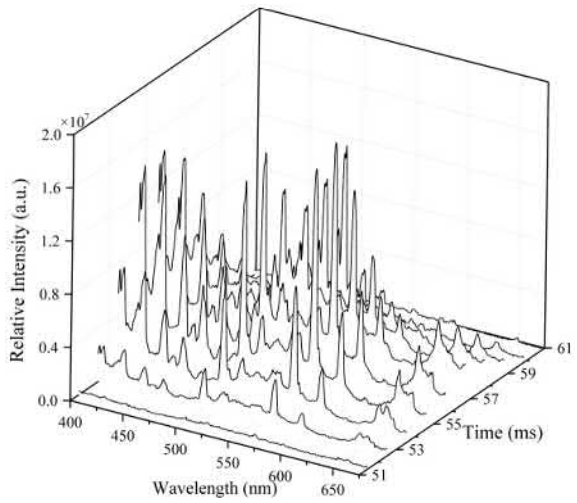

(a) 10kA

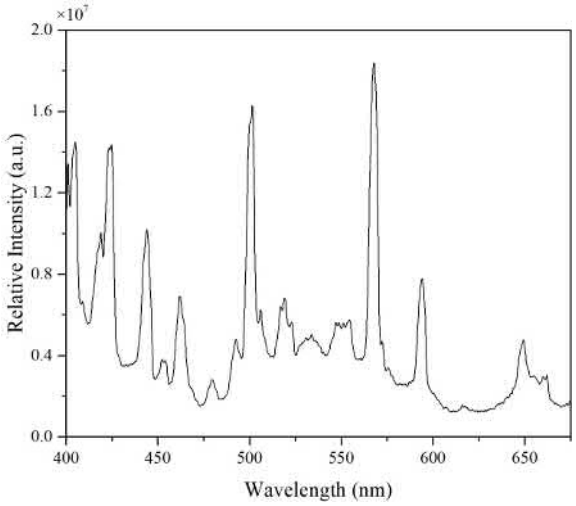

(b) 10kA peak time

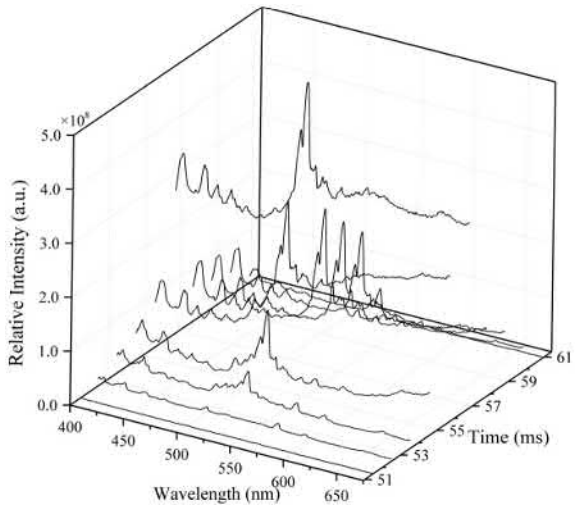

(c) 20kA

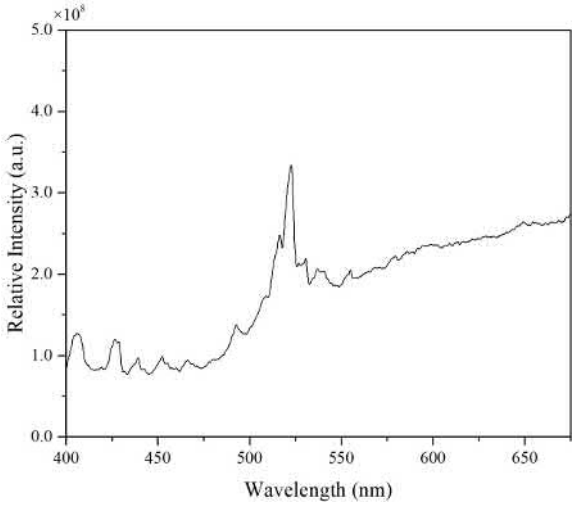

(d) 20kA peak time

Fig. B.1 Arc spectra captured for Cu contact arc in N_2 at various currents.

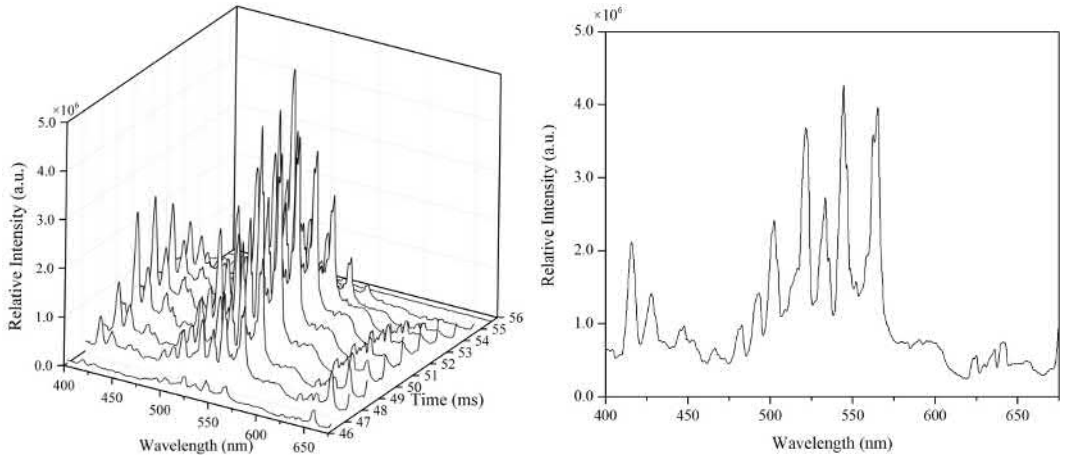

(a) 10kA

(b) 10kA peak time

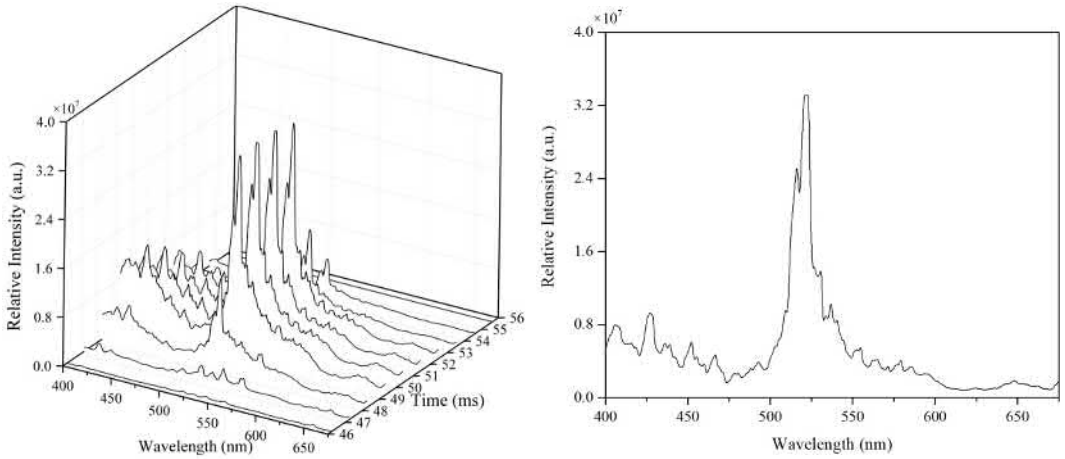

(c) 15kA

(d) 15kA peak time

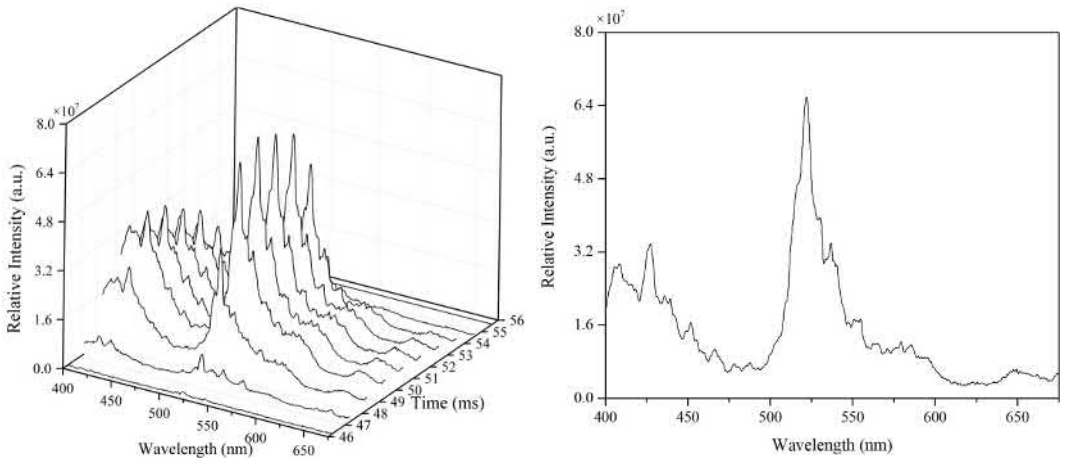

(e) 25kA

(f) 25kA peak time

Fig. B.2 Time-resolved spectra measured for CuW contact arc in SF_6 at various currents.

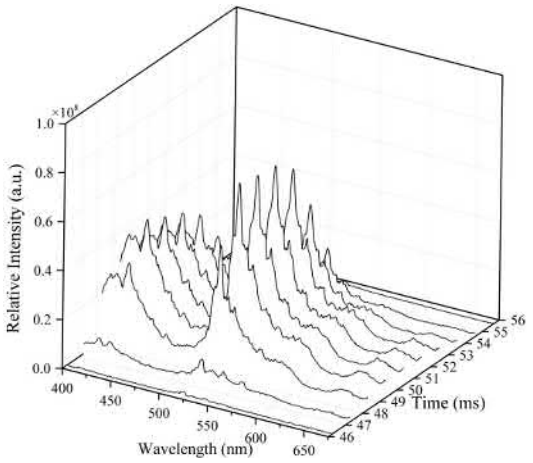

(m) 30kA

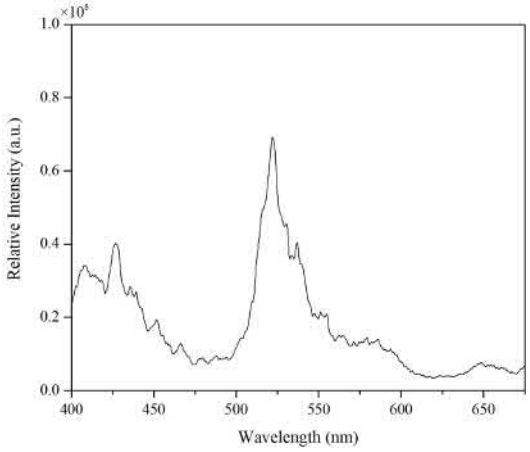

(n) 30kA peak time

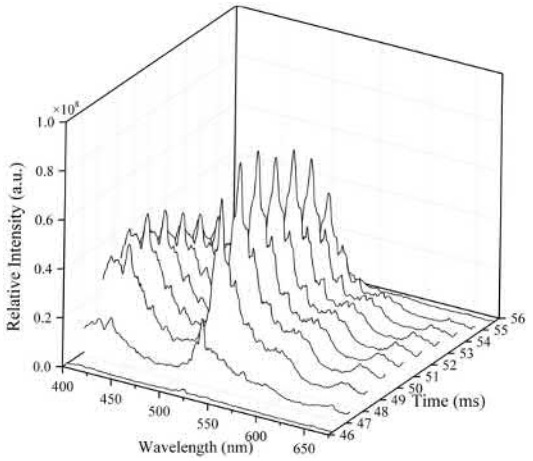

(o) 35kA

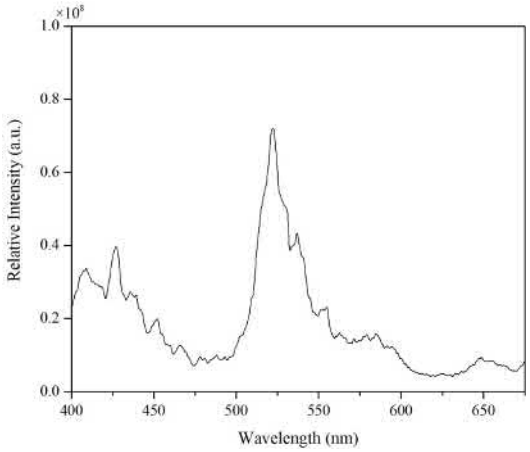

(p) 35kA peak time

Fig. B.2 Time-resolved spectra measured for CuW contact arc in SF_6 at various currents.(con't)